UNIVERSITAT POLITÈCNICA DE VALÈNCIA

A network science approach of the macroscopic organization of the brain: analysis of structural and functional brain networks in health and disease

A dissertation submitted in partial fulfillment of the requirements for the degree of Doctor of Philosophy

DEPARTAMENTO DE INGENIERÍA ELECTRÓNICA

July, 2018

Author: **Antonio Díaz Parra**

Supervisors: **Prof. Dr. David Moratal Pérez**
Center for Biomaterials and Tissue Engineering
Universitat Politècnica de València
Valencia, Spain

Prof. Dr. Santiago Canals Gamoneda
Instituto de Neurociencias
Consejo Superior de Investigaciones Científicas
Universidad Miguel Hernández
San Juan de Alicante, Spain

Acknowledgements

A mis directores de tesis. A Santiago, por su ayuda y colaboración, gracias a la cual he podido aportar mi granito de arena al campo de la neurociencia. A David, porque más allá de su ayuda científico-técnica, ha sabido escucharme y entenderme en todo momento, como un amigo atiende a otro. Porque desde el primer momento en el que empezamos a trabajar juntos, hace ya seis años, ha jugado un papel fundamental en mi desarrollo profesional. Por todo ello, David, te doy las gracias.

A todos los "moratalistas", por aguantarme estos cuatro años, pero sobre todo por su apoyo e innumerables momentos divertidos, que sin ellos no hubiera podido llegar cuerdo al final de esta etapa.

I would like to sincerely express my gratitude to Olaf Sporns and his team for teaching me the fascinating field of network neuroscience. I am also very grateful to Marcus Kaiser, Roman Bauer and their colleagues, for giving me the opportunity to learn from them. To the members of the "Hygge club", for their friendship and making my British experience extremely smooth.

A mi familia, porque no hay palabras que puedan expresar mi gratitud hacia ellos. Porque siempre están ahí sin esperar nada a cambio. Nada de lo que he logrado hasta ahora hubiera sido posible sin su apoyo.

A Raquel, por su generosidad y paciencia. Por su valentía. Por respetar todas y cada una de mis decisiones. A ti, Raquel, porque verdaderamente eres mi presente y mi futuro.

Abstract

The brain is considered to be the most complex system in the known universe. It is composed of massively connected elements arranged into modules that form hierarchical networks. Experimental evidence reveals a well-defined connectivity design, characterized by the presence of strategically connected core nodes that critically contribute to resilience and maintain stability in interacting brain networks. Certain brain pathologies, such as Alzheimer's disease and alcohol use disorder, are thought to be a consequence of cascading maladaptive processes that alter normal connectivity. These findings have greatly contributed to the development of network neuroscience to understand the macroscopic organization of the brain.

This thesis focuses on the application of network science tools to investigate structural and functional brain networks in health and disease. To accomplish this goal, three specific studies are conducted using human and rodent data recorded with magnetic resonance imaging (MRI) and tracing technologies.

Connectomics data from animal models provide an invaluable opportunity to reveal the complex interplay between structure and function in the mammalian brain. In the first study, we examine the relationship between structural and functional connectivity in the rat cortical network. Using a detailed cortical structural matrix obtained from published histological tracing data, we first compare structural connections in the rat cortex with their corresponding spontaneous correlations extracted empirically from functional MRI (fMRI) data. We then show the results of this comparison by relating structural properties of brain connectivity to the functional modularity of

resting-state networks. Specifically, we study link reciprocity in both intra- and inter-modular connections as well as the structural motif frequency spectrum within functionally defined modules. Overall, our results provide further evidence that structural connectivity is coupled to and shapes functional connectivity in cortical networks.

The pathophysiological process of Alzheimer's disease is thought to begin years before clinical decline, with evidence suggesting pahtogenic seeding and subsequent prion-like spreading processes of neurofibrillary tangles and amyloid plaques. In the second study of this thesis, we investigate whether structural brain networks as measured with diffusion-weighted MRI (dMRI) could serve as a complementary diagnostic tool in prodromal dementia. Using imaging data from the Alzheimer's Disease Neuroimaging Initiative (ADNI) database, we first aim to implement machine learning techniques to extract centrality features that are altered in Alzheimer's dementia. We then incorporate data from the Nathan Kline Institute-Rockland Sample (NKI) database and create dynamical models of normal aging and Alzheimer's disease to estimate the earliest detectable stage associated with dementia in the simulated disease progression. Our model results suggest that changes associated with dementia begin to manifest structurally at early stages.

Statistical dependence measures computed between blood oxygen level dependent (BOLD) signals can inform about brain functional states in studies of neurological and psychiatric disorders. Furthermore, its non-invasive nature allows comparable measurements between clinical and animal studies, providing excellent translational capabilities. In the last study, we apply the network-based statistic (NBS) method to investigate alterations in the resting-state functional connectivity of the rat brain in a postdependent (PD) state, an established animal model of clinical relevant features in alcoholism. The analysis reveal statistically significant differences in a connected subnetwork of structures with known relevance for addictive behaviors, hence suggesting potential targets for therapy.

This thesis provides three novel contributions to understand the healthy and pathological brain connectivity under the perspective of network science. The results obtained in this thesis underscore that brain network models offer further insights into the structure-function coupling in the brain. More importantly, this network perspective provides potential applications for the diagnosis and treatment of neurological and psychiatric disorders.

Resumen

El cerebro se considera el sistema más complejo de todo el universo conocido. Está constituido por numerosos elementos que se encuentran interconectados de forma masiva y organizados en módulos que forman redes jerárquicas. Resultados recientes revelan la existencia de un diseño de conectividad cerebral donde regiones estratégicamente conectadas (*core nodes*) contribuyen de forma crítica a la capacidad de adaptación de las redes cerebrales, y a la estabilidad de las mismas. Ciertas patologías cerebrales, como la enfermedad de Alzheimer y el trastorno por consumo de alcohol, se consideran el resultado de efectos en cascada que alteran la conectividad cerebral. Estos descubrimientos han contribuido sustancialmente al desarrollo de la neurociencia basada en redes como un marco de trabajo para explicar y entender la organización macroscópica del cerebro.

La presente tesis tiene como objetivo principal la aplicación de las técnicas de análisis de la ciencia de redes para el estudio de las redes estructurales y funcionales en el cerebro, tanto en un estado control como en un estado patológico. Así, se han llevado a cabo tres estudios específicos que cubren el análisis de datos cerebrales adquiridos en humanos y ratas mediante las técnicas de imagen de resonancia magnética (*magnetic resonance imaging, MRI*) y de trazado neuronal.

La información aportada por el conectoma de animales de experimentación es clave para entender la compleja relación entre la estructura y la función en el cerebro. Así, en el primer estudio de la presente tesis se examina la relación entre la conectividad estructural y funcional en la corteza cerebral

de la rata. En primer lugar, se lleva a cabo un análisis comparativo entre las conexiones estructurales en la corteza cerebral de la rata y los valores de correlación calculados sobre las mismas regiones. La información acerca de la conectividad estructural se ha obtenido a partir de estudios previos, mientras que la conectividad funcional se ha calculado a partir de imágenes de resonancia magnética funcional. A continuación, determinadas propiedades topológicas, y extraídas de la conectividad estructural, se relacionan con la organización modular de las redes funcionales en estado de reposo. En particular, se estudia la reciprocidad de las conexiones estructurales entre regiones del mismo módulo funcional, así como entre regiones localizadas en diferentes módulos funcionales. Por otro lado, también se analizan las diferentes configuraciones (*network motifs*) en las que pueden relacionarse estructuralmente tres regiones cerebrales del mismo módulo funcional. Siguiendo la línea de investigaciones previas, los resultados obtenidos en este primer estudio demuestran que la conectividad estructural y funcional cortical están altamente relacionadas entre sí. Además, la conectividad estructural condiciona las relaciones funcionales que suceden entre las diferentes regiones cerebrales.

El proceso patofisiológico de la enfermedad de Alzheimer tiene lugar antes de que se produzca el deterioro cognitivo. Estudios recientes sugieren que el origen de esta enfermedad reside en un mecanismo en el cual depósitos de ovillos neurofibrilares y placas de beta-amiloide se acumulan en ciertas regiones cerebrales, y tienen la capacidad de diseminarse por el cerebro actuando como priones. En el segundo estudio de la presente tesis se investiga si las redes estructurales que se generan con la técnica de resonancia magnética ponderada en difusión podrían ser de utilidad para el diagnóstico de la pre-demencia causada por la enfermedad de Alzheimer. Mediante el uso de imágenes procedentes de la base de datos *ADNI* (*Alzheimer's Disease Neuroimaging Initiative*), se aplican técnicas de aprendizaje máquina con el fin de identificar medidas de centralidad que se encuentran alteradas en la demencia. En la segunda parte del estudio, se utilizan imágenes procedentes de la base de datos *NKI* (*Nathan Kline Institute-Rockland Sample*) para construir un modelo matemático que simule el proceso de envejecimiento normal, así como otro modelo que simule el proceso de desarrollo de la enfermedad. Con este modelado matemático, se pretende estimar la etapa más temprana que está asociada con la demencia. Los resultados obtenidos de las simulaciones sugieren que en etapas tempranas de la enfermedad de Alzheimer se producen alteraciones estructurales relacionados con la demencia.

La cuantificación de la relación estadística entre las señales *BOLD* (*blood oxygen level dependent*) de diferentes regiones puede informar sobre el estado

funcional cerebral característico de enfermedades neurológicas y psiquiátricas. Además, debido a su naturaleza no invasiva, es posible comparar los resultados obtenidos entre estudios clínicos y estudios con animales de experimentación. En el tercer y último estudio de la presente tesis se estudian las alteraciones en la conectividad funcional que tienen lugar en ratas dependientes del consumo de alcohol cuando se encuentran en estado de reposo. Para ello, se ha aplicado el método *NBS* (*network-based statistic*). El análisis de este modelo de rata revela diferencias estadísticamente significativas en una subred de regiones cerebrales que están implicadas en comportamientos adictivos. Por lo tanto, estas estructuras cerebrales podrían ser el foco de posibles dianas terapéuticas.

En resumen, la presente tesis aporta tres innovadoras contribuciones para entender la conectividad cerebral bajo la perspectiva de la ciencia de redes, tanto en un estado control como en un estado patológico. Los resultados destacan que los modelos basados en las redes cerebrales permiten esclarecer la relación entre la estructura y la función en el cerebro. Y quizás más importante, esta perspectiva de red tiene aplicaciones que se podrían trasladar a la práctica clínica, tanto para el diagnóstico como para el tratamiento de enfermedades neurológicas y psiquiátricas.

Resum

El cervell es considera el sistema més complex de tot l'univers conegut. Està constituït per nombrosos elements que es troben interconnectats de forma massiva i organitzats en mòduls que formen xarxes jeràrquiques. Resultats recents revelen l'existència d'un disseny de connectivitat cerebral on regions estratègicament connectades (*core nodes*) contribueixen de forma crítica a la capacitat d'adaptació de les xarxes cerebrals, i a l'estabilitat de les mateixes. Certes patologies cerebrals, com la malaltia d'Alzheimer i el trastorn per consum d'alcohol, es consideren el resultat d'efectes en cascada que alteren la connectivitat cerebral. Estos descobriments han contribuït substancialment al desenrotllament de la neurociència basada en xarxes com un marc de treball per a explicar i entendre l'organització macroscòpica del cervell.

La present tesi té com a objectiu principal l'aplicació de les tècniques d'anàlisi de la ciència de xarxes per a l'estudi de les xarxes estructurals i funcionals en el cervell, tant en un estat control com en un estat patològic. De manera que, s'han dut a terme tres estudis específics que cobreixin l'anàlisi de dades cerebrals adquirits en humans i rates per mitjà de les tècniques d'imatge de ressonància magnètica (*magnetic resonance imaging, MRI*) i de traçat neuronal.

La informació aportada pel conectoma d'animals d'experimentació és clau per entendre la complexa relació entre l'estructura i la funció en el cervell. Així, en el primer estudi de la present tesi s'examina la relació entre la connectivitat estructural i funcional en l'escorça cerebral de la rata. En primer lloc, es du a terme una anàlisi comparativa entre les connexions estructurals en l'escorça

cerebral de la rata i els valors de correlació calculats sobre les mateixes regions. La informació sobre la connectivitat estructural s'ha obtingut a partir d'estudis previs, mentre que la connectivitat funcional s'ha calculat a partir d'imatges de ressonància magnètica funcional. A continuació, determinades propietats topològiques, i extretes de la connectivitat estructural, es relacionen amb l'organització modular de les xarxes funcionals en estat de repòs. En particular, s'estudia la reciprocitat de les connexions estructurals entre regions del mateix mòdul funcional, així com entre regions localitzades en diferents mòduls funcionals. D'altra banda, també s'analitzen les diferents configuracions (*network motifs*) en les que poden relacionar-se estructuralment tres regions cerebrals del mateix mòdul funcional. Seguint la línia d'investigacions prèvies, els resultats obtinguts en este primer estudi demostren que la connectivitat estructural i funcional cortical estan altament relacionades entre si. A més, la connectivitat estructural condiciona les relacions funcionals que succeeixen entre les diferents regions cerebrals.

El procés patofisiològic de la malaltia d'Alzheimer té lloc abans de que es produeisca el deteriorament cognitiu. Estudis recents suggereixen que l'origen d'esta malaltia resideix en un mecanisme en el qual depòsits d'ovulets neurofibrilars i plaques de beta-amiloide s'acumulen en certes regions cerebrals, i tenen la capacitat de disseminar-se pel cervell actuant com a prions. En el segon estudi de la present tesi s'investiga si les xarxes estructurals que es generen amb la tècnica de la imatge per ressonància magnètica ponderada en difusió podrien ser d'utilitat per al diagnòstic de la predemència causada per la malaltia d'Alzheimer. Per mitjà de l'ús d'imatges procedents de la base de dades *ADNI* (*Alzheimer's Disease Neuroimaging Initiative*), s'apliquen tècniques d'aprenentatge màquina a fi d'identificar mesures de centralitat que es troben alterades en la demència. En la segona part de l'estudi, s'utilitzen imatges procedents de la base de dades *NKI* (*Nathan Kline Institute-Rockland Sample*) per a construir un model matemàtic que simule el procés d'envelliment normal, així com un altre model que simule el procés de desenrotllament de la malaltia. Amb este modelatge matemàtic, es pretén estimar l'etapa més primerenca que està associada amb la demència. Els resultats obtinguts de les simulacions suggereixen que en etapes primerenques de la malaltia d'Alzheimer es produeixen alteracions estructurals relacionats amb la demència.

La quantificació de la relació estadística entre els senyals *BOLD* (*blood oxygen level dependent*) de diferents regions pot informar sobre l'estat funcional cerebral característic de malalties neurològiques i psiquiàtriques. A més, a causa de la seua naturalesa no invasiva, és possible comparar els resultats obtinguts entre estudis clínics i estudis amb animals d'experimentació. En

el tercer i últim estudi de la present tesi s'estudien les alteracions en la connectivitat funcional que tenen lloc en rates dependents del consum d'alcohol quan es troben en estat de repòs. Per a realitzar-ho, s'ha aplicat el mètode *NBS* (*network-based statistic*). L'anàlisi d'aquest model de rata revela diferències estadísticament significatives en una subxarxa de regions cerebrals que estan implicades en comportaments addictius. Per tant, estes estructures cerebrals podrien ser el focus de possibles dianes terapèutiques.

En resum, la present tesi aporta tres innovadores contribucions per a entendre la connectivitat cerebral davall la perspectiva de la ciència de xarxes, tant en un estat control com en un estat patològic. Els resultats destaquen que els models basats en les xarxes cerebrals permeten aclarir la relació entre l'estructura i la funció en el cervell. I potser més important, esta perspectiva de xarxa té aplicacions que es podrien traslladar a la pràctica clínica, tant per al diagnòstic com per al tractament de malalties neurològiques i psiquiàtriques.

Contents

List of Figures

List of Tables

Abbreviations and Acronyms

ADNI Alzheimer's Disease Neuroimaging Initiative

ADRDA Alzheimer's Disease and Related Disorders Association

AIC Akaike information criterion

AUC area under the curve

BOLD blood oxygen level dependent

DCM dynamic causal modeling

DMN default mode network

dMRI diffusion-weighted MRI

DTI diffusion tensor imaging

EEG electroencephalography

EPI echo-planar imaging

FDR false discovery rate

fMRI functional MRI

FN false negatives

fODF fiber orientation density function

FOV field of view

FP false positives

FWER family-wise error rate

GLM general linear model

GRE gradient-echo

ICA independent component analysis

IQR interquartile range

MCI mild cognitive impairment

MEG magnetoencephalography

MMSE mini mental state examination

MRI magnetic resonance imaging

NBS network-based statistic

NINCDS National Institute of Neurological and Communicative Diseases and Stroke

NKI Nathan Kline Institute-Rockland Sample

PD postdependent

PET positron emission tomography

PWS Paxinos&Watson space

RARE rapid acquisition with relaxation enhanced

RCAMs rat cortical association macroconnections

RF random forest

ROC receiver operating characteristic

ROI region of interest

rs-fMRI resting-state fMRI

SI susceptible-infected

sMRI structural MRI

SVM support vector machine

SwS Swanson space

TE echo time

TEeff effective echo time

TN true negatives

TP true positives

TR repetition time

z-Rand z-score of the Rand index

"Mejor hacer algo bueno que nada perfecto"

DVD

Chapter 1

Introduction

1.1 Motivation

The brain is composed of massively connected elements arranged into modules that form hierarchical networks. The different modules do not operate in isolation; on the contrary, interactions at multiple levels occur giving rise to the characteristic fluctuations of brain activity. Theory shows that connecting networks yield an infrastructure in which small and local perturbations can be amplified in cascade, resulting in frequent catastrophic failures and wide-range alterations (Reis et al., 2014). Experimental evidence from humans and rodents reveals a well-defined connectivity design, characterized by the presence of strategically connected core nodes that critically contribute to resilience and maintain stability in interacting brain networks (Gallos et al., 2012; van den Heuvel and Sporns, 2011, 2013). These findings predict that modifying activity in this set of core nodes could drastically alter global patterns of brain activity; which, in turn, raises the possibility that certain brain pathologies might be a consequence of cascading maladaptive processes that alter normal connectivity (Aerts et al., 2016; Fornito et al., 2015; Stam, 2014). Interestingly, this network perspective of the brain is greatly contributing to our understanding of the mechanisms behind different neurological and psychiatric disorders, such as Alzheimer's disease and alcohol use disorder (Deco and Kringelbach, 2014).

Theoretical advancement in the knowledge of the healthy and pathological brain connectivity has been accompanied by the development of non-invasive brain imaging technologies, largely magnetic resonance imaging (MRI) (Jbabdi et al., 2015). MRI provides a variety of contrast or modalities that have the capacity to sense different properties of brain tissues. For instance, diffusion-weighted MRI (dMRI) is a MRI modality based on the mobility of water molecules and is widely employed for the mapping of the structural connectome (*i.e.*, the comprehensive network map of the structural neural connections of a nervous system) (Sporns et al., 2005). On the other hand, functional MRI (fMRI) measures changes in blood oxygenation associated with brain activity. In contrast to dMRI, fMRI enables the mapping of the functional connectome (*i.e.*, the comprehensive network map of the functional neural connections of a nervous system) (Smith et al., 2013)[1].

The use of rodents and other animals provides further advantages for mapping brain-wide networks and investigating brain connectivity (Díaz-Parra et al., 2017b; Gozzi and Schwarz, 2016; Jonckers et al., 2015; Sethi et al., 2017). Specifically, animal models can be examined in-depth to extract a highly detailed structural connectome through histological procedures (van den Heuvel et al., 2016b) and offer the possibility to complete imaging data with a wealth of neurophysiological techniques to measure and manipulate brain function (Grayson et al., 2016).

Over the last decade, analytic methods adopted from network science have gained prominence in neuroscientific applications (Bullmore and Bassett, 2011; Craddock et al., 2013; Fornito et al., 2013; Rubinov and Sporns, 2010). These tools provide an elegant framework to formally investigate the network organization of the brain. Network tools can be applied for the analysis of individual connections between single neurons. Nevertheless, most of the present research is being held at the macroscopic level due to technical limitations in current MRI technology (Jbabdi et al., 2015). More specifically, the macroscopic organization of the brain is modeled as a complex network of areas or regions that interact with each other. Whilst this representation of the brain might seem simplistic at first sight, numerous neural phenomena can be effectively addressed by means of whole-brain network models; to mention a few: *how does the abundant repertoire of functional states emerge from a*

---

[1]Although the term "connectome" refers to the network map comprising a whole nervous system, it is commonly used as synonymous with "brain connectivity" to refer to the interactions between a particular set of brain regions. On the other hand, even though a brain network comprises both regions and connectivity between them, the terms "brain connectivity" and "brain network" are sometimes used interchangeably. This is essentially because connectivity makes the brain a system composed of hierarchical networks (more about this in chapter 2).

relatively fixed structure? What can brain connectivity tell us about the status of a subject? How robust is the brain against lesions? (Aerts et al., 2016; Bassett and Sporns, 2017; Ebadi et al., 2017; Park and Friston, 2013).

The great expectations raised in the field of network neuroscience motivated the development of this thesis. Specifically, this field has been able to explain the existence of interacting networks through highly connected core nodes that critically shape neural response to damage or insult. Additionally, MRI technology possess the ability to gather data as to brain structure and function from both humans and rodents, hence establishing an important tool for translational neuroimaging.

1.2 Objectives

The main objective of this thesis is the application of network science tools to uncover organizational principles governing structural and functional brain networks in health and their disruption in pathological states. Three specific objectives are aimed:

1. To investigate the relationship between the topology of structural and functional brain networks in health.

2. To investigate whether structural brain networks could serve as a complementary diagnostic tool in prodromal dementia caused by Alzheimer's disease.

3. To evaluate the impact of alcohol use disorder on brain dynamics by identifying alterations in functional brain networks.

1.3 Contributions to knowledge

This thesis provides three novel contributions to understand the healthy and pathological brain connectivity under the perspective of network science. The results obtained in this thesis underscore that brain network models offer valuable insights into the principles underlying brain structure and function and that this network perspective have potential clinical applications.

The first contribution is that resting-state fMRI (rs-fMRI) networks based on the fluctuations in blood oxygen level dependent (BOLD) signals extracted from the cerebral cortex of the rat are greatly constrained by the underlying

structural connections (Díaz-Parra et al., 2017b). To the best of our knowledge, this is the first work aimed to compare experimental rat functional connectivity with the rat cortical connectome, which provides information as to the directionality of structural interactions. The knowledge of this information enables characterizing the topology of structural networks using measures that are currently impracticable in human studies.

The second contribution is that structural brain networks as measured with dMRI can yield a complementary tool to detect Alzheimer's disease at early stages (Díaz-Parra et al., 2018). Based on emergent evidence pointing toward prion-like spreading processes and failure of hubs, we model the propagation of a disease factor and the associated degradation in connectivity. This work provides further evidence that network centrality is disrupted in Alzheimer's disease. Importantly, our model simulations suggest that network centrality is also disrupted at early stages, presumably before meeting diagnostic criteria for clinical dementia, hence serving as a potential biomarker before the onset of symptoms.

Finally, the third contribution is that intrinsic interactions occurring in functional brain networks are decreased after alcohol consumption (Díaz-Parra et al., 2017a). Taking advantage of rodent models to faithfully investigate drug dependence-related disorders, this analysis reveals a set of interacting brain areas that could potentially serve as targets in the development of therapeutic strategies in alcohol use disorder.

1.4 Thesis structure

This thesis is structured in 6 chapters. **Chapter 1** has focused on the research motivation behind this thesis and summarized the potential of network science for brain connectivity analysis. Additionally, this introductory chapter has established the specific objectives addressed in this thesis, as well as the resulting contributions to the field of network neuroscience.

Chapter 2 provides an overview as to the main techniques and procedures involved in brain network analysis. This chapter begins presenting biological details regarding the multiscale organization of the brain and the different types of brain connectivity. General concepts about network science are next introduced and a network framework to explain brain connectivity is presented. The chapter continues introducing a typical workflow for brain network analysis and surveying the methods involved in each step. The ideas introduced in this chapter are required for a deeper comprehension of the rest of the manuscript.

Chapter 3 carries out comparisons between the structural and functional brain connectivity in the cerebral cortex of the rat in a healthy state. This analysis is performed at a connection-level, but also using measures of complex networks (in particular, modularity, reciprocity and network motifs). The latter comparison reveals the importance of considering the brain as a networked system. This chapter further covers the most common frameworks for localization of brain structures in rodents (*i.e.*, the Swanson space (SwS) and Paxinos&Watson space (PWS)), the effect of global signal regression on data preprocessing, as well as the impact of anesthesia on functional brain networks extracted from rodents.

Chapter 4 explains the emerging hypothesis as to Alzheimer's disease, which is characterized by the progressive degradation of brain connections. Leveraging machine learning algorithms (for feature selection, classification and model evaluation) and a computational model simulating the spreading dynamics of a disease agent, this chapter extracts predictive brain signatures of dementia caused by Alzheimer's disease and estimates how early network alterations associated with dementia begin to manifest structurally.

Chapter 5 highlights the advantages of considering rodent models when investigating the effects of alcohol use disorder on functional brain connectivity and performs a comparative analysis between a group of control rats and a cohort of rats in a postdependent (PD) state. This analysis is based on a recently proposed method named network-based statistic (NBS), which accounts for the connected nature of the brain. This chapter finally touches upon the current issues regarding the interpretation of negative (anticorrelated) correlations between BOLD signals.

Chapter 6 provides an overall conclusion and future prospects.

Finally, this mansucript ends with a brief CV and a listing of references.

Chapter 2

Approaching the brain as a complex network

2.1 Brain connectivity

The brain is the most complex organ in the human body, allowing and coordinating processes related to perception, cognition and action (Park and Friston, 2013). Underlying these high-order processes, functional segregation and integration occur in the brain as a result of the neural synchronous activity (Friston, 2011). **Functional segregation** suggests that a cortical area is specialized for some aspects of perceptual or motor processing, whereas **functional integration** refers to the capacity of anatomically segregated areas to cooperate. Likewise that cognition is supported by these operational principles, functional integration between neural elements is in turn constrained by structural connections (Sporns et al., 2005). Therefore, it is possible to conceive cognition as the ultimate product emerging from the interplay between the way neurons are structurally connected to each other (*i.e.*, structure) and the dynamical activity (*i.e.*, function) occurring in neural circuits (Honey et al., 2010).

Brain structure and function can be examined at different scales due to the hierarchical organization of the brain (Friston, 2011; Sporns et al., 2005). At the **microscale**, single neurons represent the basic element for information processing and synapses enable communication. At the **mesoscale**, individual neurons are arranged into minicolumns and macrocolumns and message passing between them is mediated by their connection patterns. Finally, the **macroscale** is characterized by the aggregation of neural columns into brain regions that are connected by inter-regional fiber pathways. Advancement in the knowledge of brain structure and function across scales relies critically on the available recording techniques for brain mapping. In particular, the development of MRI has greatly influenced the study of the brain and provided mechanistic insights into its macroscopic organization (Power et al., 2011; Thomas Yeo et al., 2011).

A critical concept is that of **brain connectivity**. Understanding the mechanisms underlying brain function without accounting for its circuitry and connectivity would be imprecise and meaningless at present (Razi and Friston, 2016). The concept of brain connectivity has generated some debates along the history (Horwitz, 2003); however, it is widely recognized that interactions between brain areas can be described using three different, but related, perspectives (Friston, 2011). **Anatomical** or **structural connectivity** refers to patterns of anatomical connections linking brain areas. **Functional connectivity** is defined as the statistical dependence between recorded activity time series. Finally, **effective connectivity** refers to the causal influence that one neural system exerts over another. Whilst the former describes brain structure, functional connectivity and effective connectivity describe brain function, and more specifically, functional integration.

Differentiating between functional and effective connectivity entails important conceptual and methodological issues. The functional connectivity between region A and region B is estimated using some measure of statistical dependence (*e.g.*, the Pearson correlation coefficient) computed from the observed time series. By contrast, the estimation of the effective connectivity between the same regions relies on a biophysical generative model attempting to explain the observed dependencies (*i.e.*, the functional connectivity) (Friston, 2011). This is critical when using fMRI data because what we are actually measuring through this technique are variations in blood oxygenation associated with brain activity and thereby the BOLD signal is an indirect measure of neural dynamics (Buxton, 2010). In other words, the fMRI signal is a measurable (observable) variable whereas the underlying neural activity is a latent (unobserved) variable. Thus, methods to estimate the

effective connectivity between regions, such as dynamic causal modeling (DCM) (Friston et al., 2003), rely on sophisticated mathematical and statistical modeling approaches to infer the latent causal influence (Valdes-Sosa et al., 2011). *How does the structural connectivity come into play in this context?* Structural connections establish a pathway through which neural information can flow. Therefore, the structural connectivity restricts, although does not determine, the causal interactions between neural elements (*i.e.*, the effective connectivity) and, ultimately, the observed dependencies (*i.e.*, the functional connectivity). Functional integration can be further measured in both task-evoked and resting-state experiments (Cole et al., 2014; Fox and Raichle, 2007; Smith et al., 2009). In **task-evoked experiments** subjects are engaged in performing a particular task, whereas in **resting-state experiments** subjects are scanned "at rest" to assess spontaneous or intrinsic BOLD fluctuations.

2.2 Network science

Network science is the scientific field that deals with the formal study of complex networks (*e.g.*, social networks) or any system that can be modeled as such (*e.g.*, air transport networks) (Newman, 2003, 2010; Strogatz, 2001). In essence, a *network* represents a system constituted of *nodes* (also called *vertices*) that are somehow related (or connected) to each other through *links* (also called *edges*). A network is commonly represented by means of a *graph* and a *connectivity matrix*, W, with rows and columns encoding nodes, and matrix entries quantifying the connectivity between nodes. Different types of graphs (or networks) can be defined[1]:

Binary, Weighted: A binary network consists in a network in which $w_{i,j} \in \{0,1\}$, with $w_{i,j} = 1$ indicating the existence of interaction from node i to j. The connectivity matrix in a binary network is commonly named *adjacency matrix*, A, to explicitly indicate that matrix entries merely provide information about which nodes are inter-related. By contrast, edges connecting any pair of nodes in a weighted network can take values that are real numbers, reflecting connection strengths.

Undirected, Directed: An undirected network (Figure 2.1) consists in a network in which the edges do not provide information about the directionality of interaction, that is, $w_{i,j} = w_{j,i}$. In a directed network

---

[1]Multitude of graphs can be defined according to different criteria. However, we here restrict the classification to those types that are more relevant in the context of brain networks.

(Figure 2.2), the edges have directionality. Thus, connectivity matrices of undirected networks are always symmetric.

$$W = \begin{pmatrix} 0 & 7 & 0 & 1 & 0 \\ 7 & 0 & 2 & 0 & 5 \\ 0 & 2 & 0 & 0 & 8.3 \\ 1 & 0 & 0 & 0 & 10.1 \\ 0 & 5 & 8.3 & 10.1 & 0 \end{pmatrix}$$

$$A = \begin{pmatrix} 0 & 1 & 0 & 1 & 0 \\ 1 & 0 & 1 & 0 & 1 \\ 0 & 1 & 0 & 0 & 1 \\ 1 & 0 & 0 & 0 & 1 \\ 0 & 1 & 1 & 1 & 0 \end{pmatrix}$$

(a) (b)
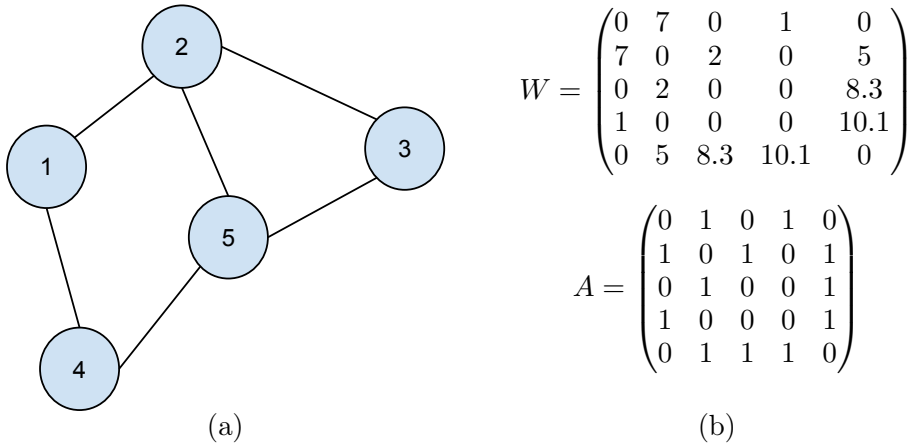
Figure 2.1. Toy example of an undirected network composed of five nodes. (a) Graph representing an undirected network composed of five nodes. (b) In its weighted version, the element $w_{i,j} = w_{j,i}$, with $i, j \in [1, \ldots, 5]$, quantifies the relationship between node i and j. In its binary version, the element $a_{i,j} = a_{j,i}$ is equal to unity when node i and j are connected, and zero otherwise.

Graph theory offers a formal language to describe the **topology** (also called **structure**) of complex networks (Boccaletti et al., 2006). The term "complex" is used to underline that the network is characterized by a series of topological properties (explained in subsection 2.3.4), such as small-worldness, the presence of hubs, modularity and hierarchy, that are not typical of null network models or reference models (*e.g.*, random graphs and regular graphs) (Bullmore and Sporns, 2009).

Whilst graph theoretical analysis of network topology is a fundamental aspect in the study of real-world networks, network science also encompasses **dynamics** (also called **function**) (Boccaletti et al., 2006). Dynamical processes are highly affected by network topology. For example, the spread of ideas in a social network relies on how users are inter-connected (Pei and Makse, 2013). How activity can change on top of network topology is referred to as **dynamics on networks**. On the other hand, edges themselves can also change. For example, when two coupled neurons fire together repeatedly, the

connection between them is strengthened. How network edges can reconfigure is referred to as **dynamics of networks**. Therefore, the topology of the network affects its dynamics but the reverse is also possible (Bassett and Sporns, 2017; Strogatz, 2001). As a result, several useful modeling approaches within network science have recently emerged to attempt to explain physical phenomena as those just described; specifically, multilayer networks (Boccaletti et al., 2014) and temporal networks (Holme and Saramäki, 2012).

$$W = \begin{pmatrix} 0 & 0 & 0 & 5 & 0 \\ 1.4 & 0 & 0 & 0 & 1 \\ 0 & 0.6 & 0 & 0 & -4.8 \\ 0.6 & 0 & 0 & 0 & 10 \\ 0 & 1 & -2 & 0 & 0 \end{pmatrix}$$

$$A = \begin{pmatrix} 0 & 0 & 0 & 1 & 0 \\ 1 & 0 & 0 & 0 & 1 \\ 0 & 1 & 0 & 0 & 1 \\ 1 & 0 & 0 & 0 & 1 \\ 0 & 1 & 1 & 0 & 0 \end{pmatrix}$$

(a)   (b)
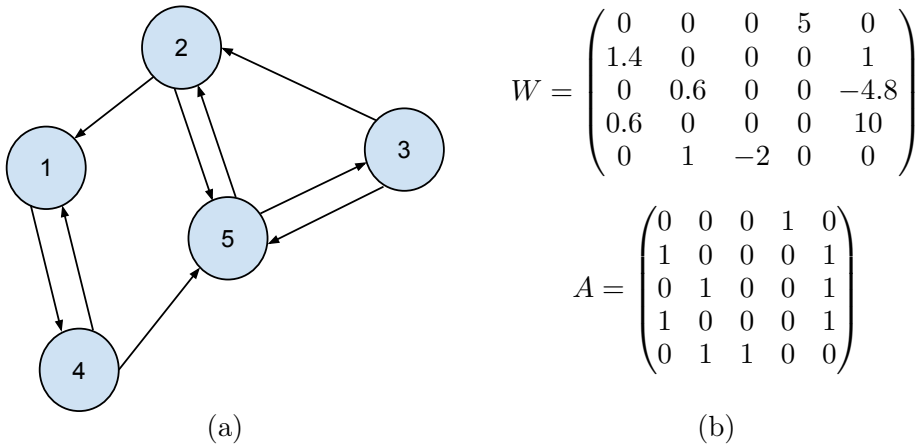
Figure 2.2. Toy example of a directed network composed of five nodes. (a) Graph representing a directed network composed of five nodes. (b) In its weighted version, the element $w_{i,j}$, with $i, j \in [1, \ldots, 5]$, quantifies the relationship from node i to j. In its binary version, the element $a_{i,j}$ is equal to unity when an interaction from node i to j occurs, and zero otherwise.

Given the potential of network science to study complex systems composed of many actors or elements that are related to each other, *how can we adopt these ideas to explain and understand brain connectivity in health and disease?* In network neuroscience, nodes and edges represent brain regions[2] and brain connectivity, respectively (Bassett and Sporns, 2017; Telesford et al., 2011). Brain networks usually fall into one of the following categories (Bullmore and Bassett, 2011; Fornito et al., 2013): binary undirected networks, weighted undirected networks, binary directed networks or weighted directed networks. Note that one can easily obtain a binary network from its weighted version by

---

[2]In this manuscript the terms "area", "region", "node", and "ROI" (introduced in subsection 2.3.2) are used interchangeably.

applying a threshold. In addition, self-connections (the main diagonal in W and A) are not usually considered in brain network analysis.

Consider that we gather data to estimate the brain connectivity among three brain areas (Figure 2.3). Assume that we measure the structural connectivity from a rodent model by using tracing technology and reconstruct the **structural brain network** illustrated in Figure 2.3a. Furthermore, assume for simplicity binary links. In human research, structural brain networks are undirected since dMRI does not allow estimating link directionality (Figure 2.3b). Either way, these structural connections offer potential fibers through which neural populations can cooperate and transmit dynamical code (like a road map providing potential pathways to traffic). For example, region 1 could transmit information to region 3 through the direct, afferent link $a_{1,3}$, but also indirectly via region 2 through $a_{1,2}$ and $a_{2,3}$. Assume the latter scenario, so after estimating the effective connectivity between each pair of areas, the resulting **effective brain network** is represented in Figure 2.3c. Finally, we could potentially obtain a **functional brain network** as that shown in Figure 2.3d, as time series from region 1 and region 3 could be statistically dependent by means of, precisely, region 2.

In the previous illustrative example, we have implicitly assumed that the three areas are isolated and do not interact with others, but the reality is that they can also communicate with other areas (as well as with other parts of the nervous system, or even with the environment). *How can this influence our insights into the brain connectivity among areas?* Now suppose that region 1 is not directly structurally connected to region 2, but are polysinaptically structurally inter-related via a missing region 4 (Figure 2.4a and Figure 2.4b) that has not been considered in the analysis because, for example, data from this region have not been recorded. Assume further that region 1 sends a neural message to region 2 through this structural path (*i.e.*, $1 \rightarrow 4 \rightarrow 2$). In this situation, we could still reconstruct the same effective brain network as before (Figure 2.4c). In this way, one is limited to investigate interactions between pairs of regions that are included in the analysis. Note that this is a different problem from that of latent and measurable variables introduced in section 2.1 when distinguishing between functional and effective connectivity. Additionally, the same reasoning is valid for undirected structural brain networks. Although we were not able to estimate the directionality of structural connections (Figure 2.4d), it would be possible to reconstruct the effective connections of Figure 2.4c. Nevertheless, knowing link directionality and incorporating this information into effective connection estimates would probably enable recovering the effective brain network more accurately.
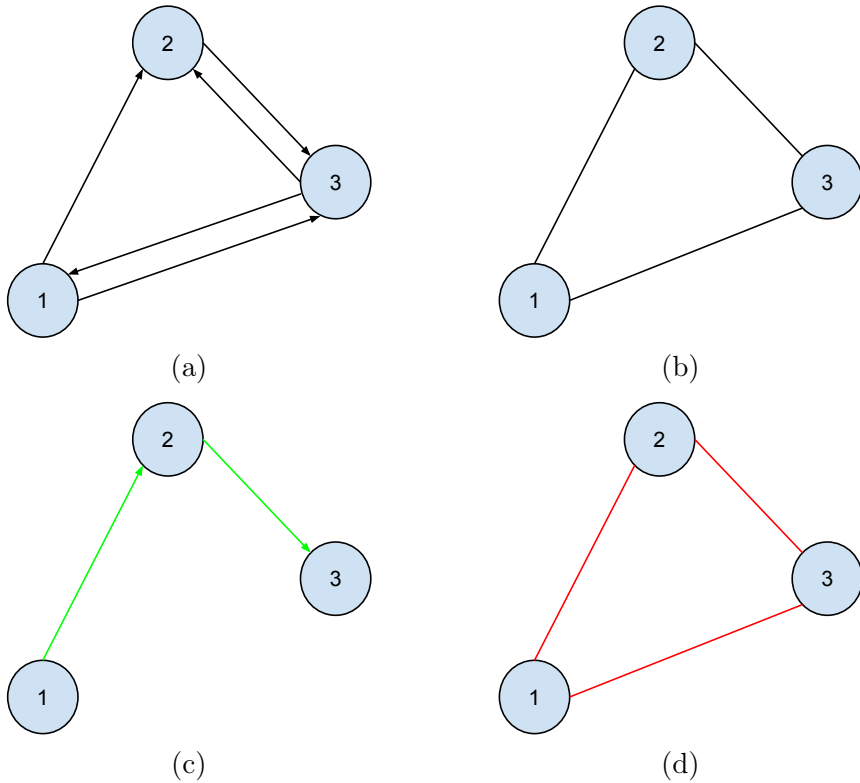
Figure 2.3. The brain from a network perspective. (a) Structural brain network represented by a directed graph. (b) Structural brain network represented by an undirected graph. (c) Effective brain network represented by a directed graph. (d) Functional brain network represented by an undirected graph.

Regardless of the type of connectivity employed to describe interactions between regions, one can interpret the resulting brain graph as a complex network with topology and dynamics. The study of effective brain networks as measured with MRI is restricted to graphs of small size due to the computational complexity associated with inferring latent states (Fornito et al., 2013; Valdes-Sosa et al., 2011). As a result, network science approaches have been widely applied to examine structural and functional, but not effective brain networks. Recent methodological advances have brought effective connectivity into the context of network science, and it is probably that in the future effective brain networks will reach a greater prominence (Razi et al.,

2017). Nevertheless, most of the current research copes with the analysis of whole-brain structural and functional graphs, which is the theme of this thesis.
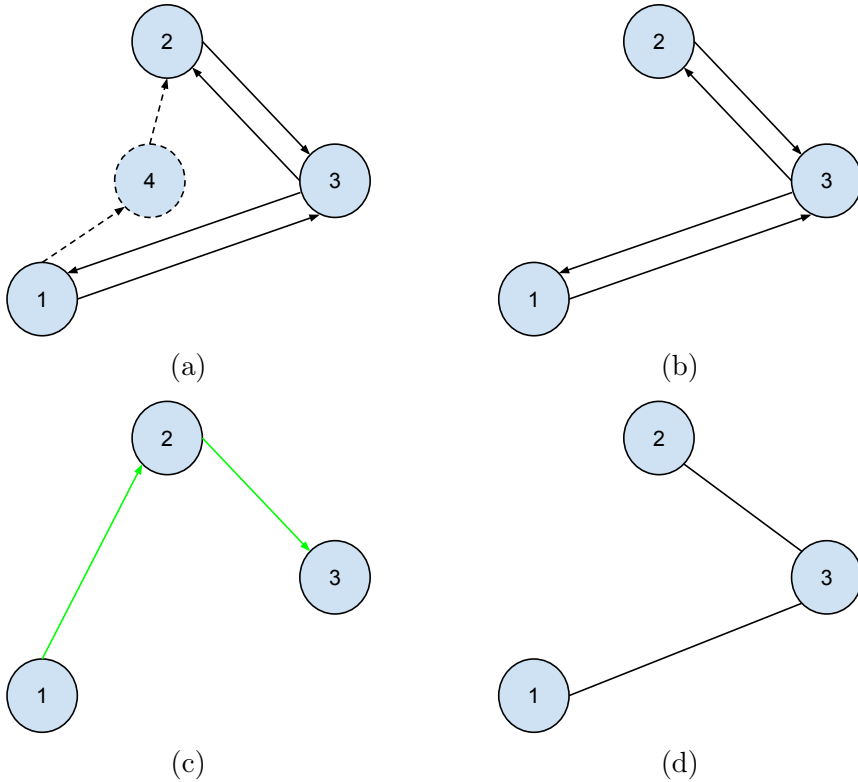
Figure 2.4. Brain networks and missing regions. (a) Data from region 4 are not recorded. (b) The resulting structural brain network does not have a direct structural connection from region 1 to 2. (c) Even so, one could potentially estimate a direct causal influence from the former to the latter. (d) Using dMRI, one would see the structural brain network as an undirected graph.

Although it is possible to characterize the topology of functional brain networks, neurobiological interpretation should be made with caution. For example, paths are sequences of nodes and links that in structural brain networks represent potential routes of information flow, whereas paths in functional networks represent sequences of statistical associations and may not

correspond to information flow on structural connections. Therefore, network measures based on functional paths are less straightforward to interpret (Rubinov and Sporns, 2010; Zalesky et al., 2012). On the other hand, functional brain networks are commonly seen as the dynamical component of structural brain networks. For example, when neural dynamical models are applied on top of structural brain networks to reproduce the organization of resting-state patterns in the brain (Deco et al., 2011; Nakagawa et al., 2013). However, it is also possible to incorporate dynamical process in functional brain networks themselves (Reis et al., 2014; Sinha et al., 2017). Likewise, previous studies have also incorporated dynamics in structural brain networks without calling for neural activity directly (Raj et al., 2012). In summary, both the topology and dynamics of structural and functional brain networks can be analyzed using network science tools, and the choice of the analytic methods relies critically on the research goal.

2.3 The brain network analysis process based on MRI

So far, we have been given a network describing structural or functional interactions between areas. In practice, there are a series of steps that one has to take until brain networks are reconstructed and subsequently analyzed (Figure 2.5). Basically, the process begins by gathering MRI data (subsection 2.3.1), which are then preprocessed (subsection 2.3.2) with the aim of correcting image distortions and preconditioning data for brain network reconstruction. Brain network reconstruction (subsection 2.3.3) mainly involves two processes: brain parcellation and brain connectivity estimation. Brain parcellation consists in dividing the brain into different areas, which will act as network nodes. Brain connectivity between pairs of nodes is then estimated, producing a connectivity matrix. This connectivity matrix encodes the topology of the corresponding structural or functional brain network from which a variety of analytic techniques (subsection 2.3.4) can be applied to extracts insights into the network organization of the brain.

2.3.1 MRI data acquisition

MRI technology enables the estimation of structural and functional whole-brain networks using dMRI and fMRI, respectively (Craddock et al., 2013; Schirner et al., 2015). Additionally, its non-invasive nature allows comparable measurements between clinical and animal studies, providing excellent translational capabilities (Gozzi and Schwarz, 2016). The fundamental physical principle underlying the estimation of structural

connectivity is that water molecules in whiter matter diffuse mainly along the path of axons, phenomenon known as anisotropic diffusion. On the contrary, diffusion of water molecules in gray matter and cerebral spinal fluids occurs approximately equally in all directions, which is known as isotropic diffusion. During acquisition, a series of images (or volumes) are acquired, each sensitive to diffusion along a specific direction (Craddock et al., 2013). Thus, by the controlled application of gradient magnetic fields across different directions, it is possible to map the orientations of fibers passing through each voxel (Figure 2.6a). This information is then used to reconstruct large-scale tracts of white matter, process known as tractography (Figure 2.6b) (Abhinav et al., 2014; Sotiropoulos and Zalesky, 2017).
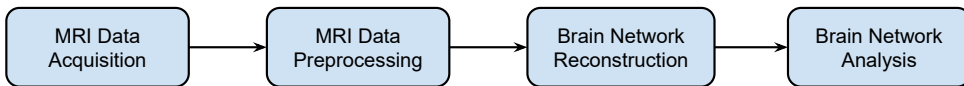
Figure 2.5. Common workflow for brain network analysis. Once the researcher has formulate the hypothesis to be tested and decided the experiment accordingly, the main steps involved in the process of brain network analysis are: acquisition of MRI data, preprocessing of MRI data, reconstruction of brain networks by dividing the brain into discrete nodes and estimating the brain connectivity between pairs of nodes and, finally, application of a variety of techniques to examine the brain from a network perspective.

Although brain function can be measured using different indices related to physiological function, such as cerebral blood flow and glucose metabolism, as well as by means of other neuroimaging modalities, such as positron emission tomography (PET), fMRI based on BOLD contrast is the most widely technique employed for estimating functional interactions[3] (Craddock et al., 2013). This modality is based on the paramagnetic nature of deoxygenated hemoglobin and the overcompensation of blood supply in response to neural activity that produces a net increase in oxygenated hemoglobin. While the physical origin of the BOLD signal is clear, both the triggering mechanisms and its relation to neural activity remain unclear (Buxton, 2010; Logothetis, 2008; Moreno et al., 2013). In this modality, a sequence of images is acquired during the course of an experiment. The BOLD signal contained in each voxel reflects oxygenating changes in the brain as a result of brain activity across time (Figure 2.7).

---

[3]In this manuscript fMRI modality always refers to fMRI based on BOLD contrast.
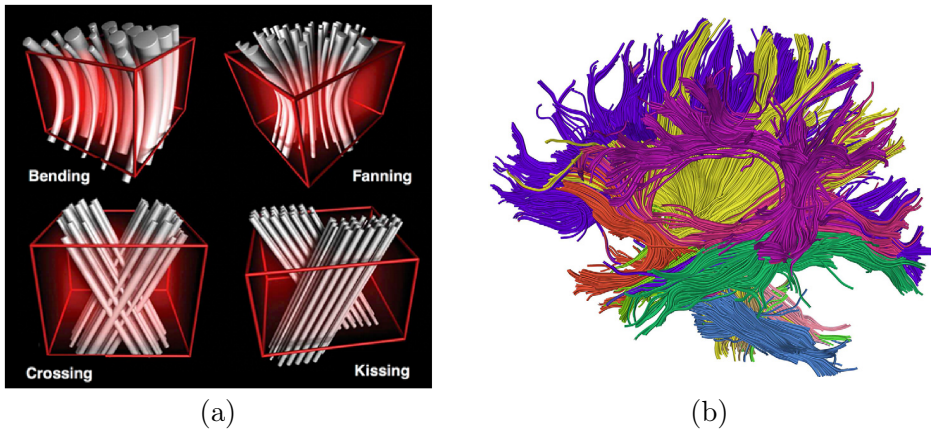
Figure 2.6. Structural brain networks are typically investigated using dMRI.
(a) Examples of fiber orientation patterns that can result within a particular voxel.
Reproduced from Sotiropoulos and Zalesky (2017). (b) Reconstruction of large-scale tracts
of white-matter extracted from fiber orientation patterns within voxels. Reproduced from
O'Donnell and Westin (2011).
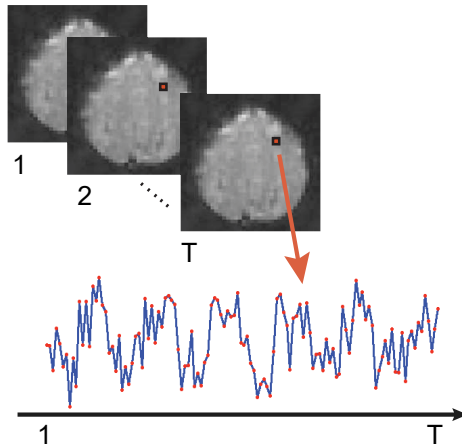
Figure 2.7. Functional brain networks are typically investigated using fMRI.
Functional interactions are estimated from BOLD signals recorded through each voxel.

The aforementioned modalities are commonly acquired along with a structural MRI (sMRI) image. This structural image is employed during data preprocessing for normalization of dMRI and fMRI images (subsection 2.3.2), as well as for node definition during brain network reconstruction (subsection 2.3.3). Therefore, a typical MRI experiment for brain network analysis rests upon dMRI, fMRI and sMRI modalities. Furthermore, each subject can undergo several *runs* (also called *trials*) within the same *session* (Figure 2.8).
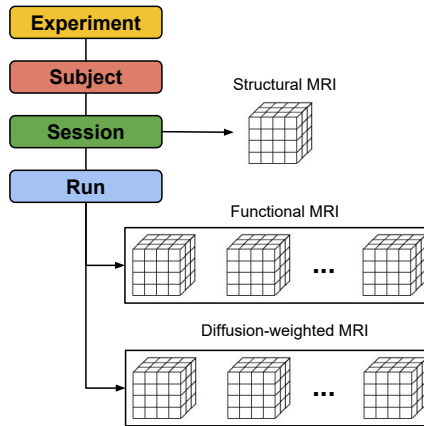
Figure 2.8. Data required for brain network analysis based on MRI technology. An experiment examines many subjects, who can be scanned in multiple sessions. A sMRI image is acquired in each session, which consists of several runs. For each run, dMRI and fMRI images are acquired to examine structural and functional brain networks, respectively. Experimenters could be interested in acquiring only one modality or both, according to their scientific goals. A structural and a functional brain network result from each run, so connectivity matrices of the same type can be averaged across runs.

2.3.2 MRI data preprocessing

To extract meaningful neurological insights from connectivity matrices, raw MRI data must be adapted and preconditioned. This is a crucial step that has generated a lot of debate, especially in rs-fMRI research (Ciric et al., 2017; Power et al., 2015). Nevertheless, a series of standard preprocessing steps are applied across studies.

Diffusion-weighted MRI data preprocessing

Magnetic field inhomogeneities in areas with materials that differ with respect to magnetic susceptibility are a major contribution to spatial distortions of dMRI (Craddock et al., 2013). Image registration, or spatial alignment of brain scans, is used in dMRI data preprocessing pipelines to correct for subject head motion and eddy-current distortions (Andersson and Sotiropoulos, 2016), which are caused by the interaction between the static magnetic field and the currents induced by rapid switching of gradients with the magnetic field. Brain extraction (*a.k.a.*, skull stripping) methods are applied to extract the brain and remove non-interest tissues such as bone and air (Smith, 2002). Recent research has also reported effects of signal drift as a result of temporal scanner instability on dMRI. Therefore, algorithms to correct for this artifact have emerged (Vos et al., 2017).

Before estimating the structural connectivity between pairs of nodes (subsection 2.3.3), large-scale fiber tracts of whiter matter must be reconstructed (Figure 2.6b). This process involves two main steps: fiber orientation estimation within each voxel and whole-brain tractography. There are a large quantity of methods for mapping fiber orientations. The simplest method is the diffusion tensor model (O'Donnell and Westin, 2011). Diffusion tensor imaging (DTI) provides an abstract ellipsoid representation of the water-diffusion profile for a given voxel. The direction of maximal diffusion, referred to as the principal diffusion direction, is used as the best estimate of fiber orientation within a voxel. A more accurate model in the case of complex fiber patterns (Figure 2.6a) is the fiber orientation density function (fODF), which characterizes the fiber distribution in each voxel (Sotiropoulos and Zalesky, 2017). Numerous methods, such as deconvolution methods, parametric, non-parametric, q-ball imaging and diffusion spectrum imaging, are aimed to provide estimates of this fODF.

Regarding tractography methods, it is possible to categorize them into two main groups: local approaches, which in a step-by-step fashion propagate curves (or streamlines) that are tangent to vector fields extracted from the fODF; and global methods, which estimate streamlines that are optimal according to a global criterion. Local methods can be in turn categorized into deterministic and probabilistic, depending on whether they perform a deterministic or stochastic estimation. Note that individual streamlines do not represent actual axons. Instead, they represent estimates of the average trajectories of axon bundles (Craddock et al., 2013; Sotiropoulos and Zalesky, 2017).

Functional MRI data preprocessing in resting-state experiments

Functional MRI data are associated with brain activity, but variations in BOLD signals come from other sources of non-interest including subject head motion, cardiac and respiratory physiological noise, blood pressure and cerebral autoregulation, and vasomotion (Murphy et al., 2013). These confounds, added to the origins of BOLD signals as being a indirect measure of brain activity, have given rise to a plethora of approaches and pipelines for rs-fMRI data preprocessing (Ciric et al., 2017; Pruim et al., 2015). In addition to spatial alignment of brain scans, the variance associated with signals of non-interest is removed through each voxel by applying a general linear model (GLM) that attempts to explain the corresponding BOLD signal. This preprocessing step is known as nuisance regression. A subject of intense interest in the fMRI community is that of global signal. The global signal is the spatial mean of all signals in the brain (Power et al., 2017). Whether or not the variance of this regressor[4] should be removed from BOLD signals is controversial, as artificial negative (or anti-correlated) correlations between time series mathematically arise when it is included in the GLM (Murphy et al., 2009). Band-pass filtering is usually applied to remove frequencies between 0.01 and 0.1 Hz. Slice-timing correction and spatial smoothing are two preprocessing steps commonly applied for fMRI data preprocessing. However, it is not clear that the former provide benefices in resting-state experiments (Wu et al., 2011), whereas the latter can introduce spurious high functional interactions between a node an its neighbors when constructing functional brain networks (Fornito et al., 2010).

MRI data normalization

To perform comparisons within and between groups, one must ensure that the brain is divided into discrete regions (subsection 2.3.3) consistently across subjects. To this end, dMRI and fMRI data must be co-registered or aligned to the sMRI image, which is in turn normalized[5] to a reference image. This reference image or template is another sMRI image that typically is associated with a digital atlas that contains a set of labels, with each label identifying a particular brain area or region of interest (ROI). Figure 2.9 presents a typical scheme for MRI data normalization.

---

[4]In the nuisance regression framework the terms "signal", "variable", "regressor" and "covariate" are used interchangeably.

[5]The term "co-registration" is used in the neuroimaging literature to refer to the alignment or image registration between dMRI or fMRI images and the sMRI. On the other hand, the term "normalization" is reserved to refer to the process of aligning or registering subject-specific images to a reference image or template for group studies. In both cases, algorithms for image registration are applied.
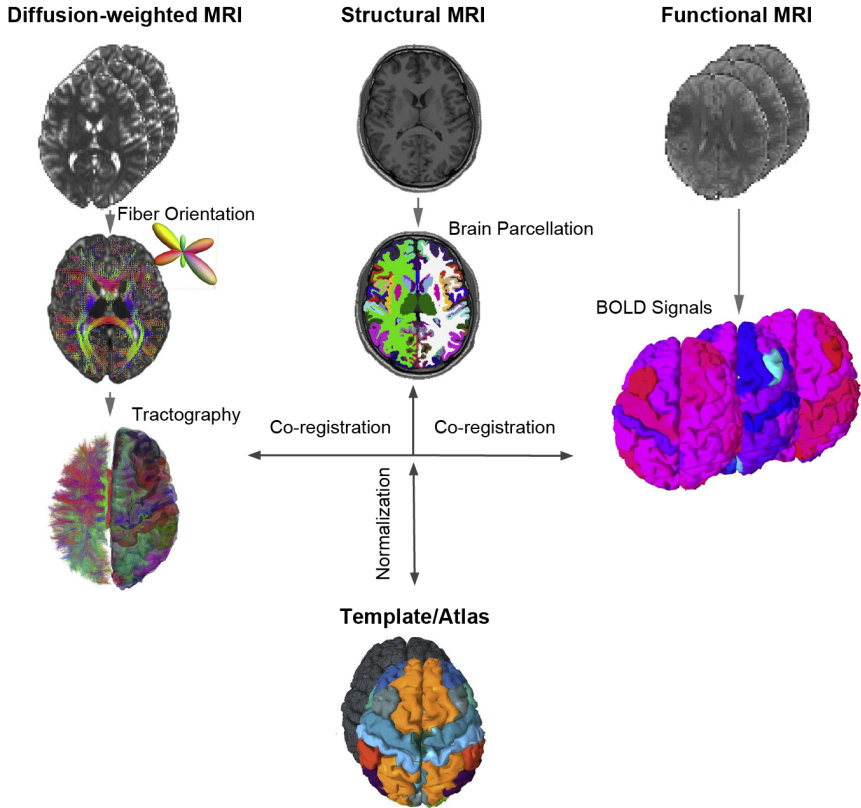
Figure 2.9. Normalization of MRI data for group studies. First, dMRI and fMRI data are spatially aligned to the subject-specific sMRI image. This sMRI image is then aligned to the template. This process generates a set of transformation matrices from which it is possible to move data between different spaces. For example, one could decide to take the template to the native spatial space defined by fMRI images or the other way around. After normalization, the subject-specific sMRI image can be fairly divided into discrete ares, as well as dMRI and fMRI data accordingly, for brain network reconstruction (subsection 2.3.3). Adapted from Schirner et al. (2015).

2.3.3 Brain network reconstruction: defining nodes and edges

The validity of a brain graph model significantly depends on to what extent its nodes and edges represent true subsystems and their interactions, respectively. Whereas in some applications this definition can be straightforward (*e.g.*, in a social network each node represents a person and edges indicate whether two nodes are "friends" or connected), accurate identification of nodes and edges in brain networks can be a tricky task (Fornito et al., 2013).

Defining nodes in brain networks

Depending on the goal of the research, the specific subsystems represented by nodes can range from small patches of the brain cortex to larger brain areas (Craddock et al., 2013). Ideally, a brain parcellation should satisfy three criteria: define functionally homogeneous nodes, represent functional heterogeneity across nodes, and account for spatial relationships (Fornito et al., 2013). As a result, diverse brain parcellation schemes based on both anatomical and functional criteria have been produced to attempt to achieve such requirements (Figure 2.10). Note that brain parcellations are depicted through a digital atlas with ROI labels and an associated template to be used in the normalization process (Figure 2.9).

Defining edges in structural brain networks

Tractography provides an estimate of the trajectories followed by fiber bundles, which are represented by "artificial" streamlines (subsection 2.3.2). Although dMRI modality cannot offer biophysical properties (*e.g.*, axonal densities and myelination) about the structural connectivity between areas, does allow computing measures that indirectly reflect these properties (Sotiropoulos and Zalesky, 2017). Edges in weighted structural brain networks are typically quantified by using the number of streamlines intersecting each pair of regions (*i.e.*, *streamline counts*) or a function of this value. Indeed, streamline counts are sometimes normalized by the size of the nodes to account for volume/area variability since, for example, larger brain regions are more likely to be more strongly connected with the rest of nodes. Other measures that do not make use of streamlines counts are also available. For example, it is possible to compute voxel-specific measures reflecting *microstructural* properties (*e.g.*, fractional anisotropy and mean diffusivity), and define edge weights as the average of these measures over all voxels traversed by those streamlines connecting two regions in question. Whereas it is questionable the ability of
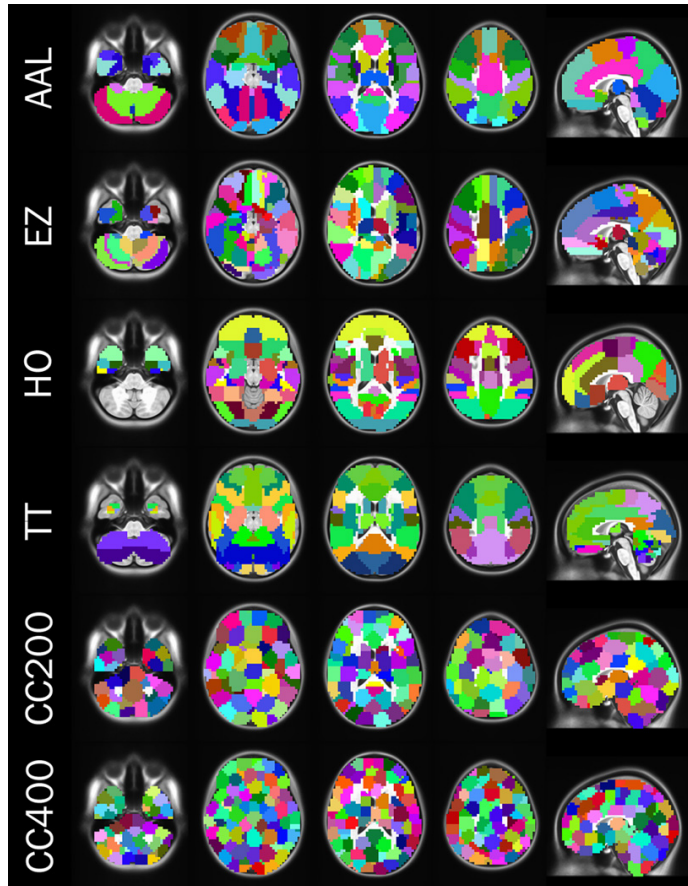
Figure 2.10. Some examples of brain parcellations for brain networks analysis. There are multitude of schemes to divide the brain into discrete areas, which represent network nodes. This figure includes six particular examples, but others are also available. The top four brain parcellations are based on anatomical criteria, whereas the bottom two are based on functional criteria. Reproduced from Craddock et al. (2013).

microstructural properties in reflecting true axonal strengths as measured with tracers, functions of streamlines can be more useful in quantifying structural connectivity (Fornito et al., 2013; Sotiropoulos and Zalesky, 2017).

Defining edges in functional brain networks

Functional connectivity is estimated from activity time series recorded in different brain areas. Several measures can be used to define functional interactions. The simplest measure is the Pearson correlation coefficient. This measure quantifies the linear relationship between signals. However, other more sophisticated measures capturing linear and nonlinear relationships (*e.g.*, mutual information) can be employed. A previous investigation has applied realistic simulations to assess the ability of different functional connectivity measures in reconstructing the true underlying network architecture generating fMRI data (*i.e.*, the effective brain network) (Smith et al., 2011). In particular, the authors computed a variety of metrics including, but not restricted to, correlation, partial correlation, regularized inverse covariance, mutual information, Granger causality, Patel's conditional dependency measures, and methods based on Bayesian networks. They concluded that partial correlation, regularized inverse covariance and Bayesian net methods offered high sensitivity to detect true network connections. Although accurate estimate of connection directionality is more tricky, Patel's conditional dependency measures gave reasonable results. Eventually, one can generate a connectivity matrix encoding the interactions between pairs of nodes (Figure 2.11).

2.3.4 Brain network analysis

Once structural and functional connectivity matrices have been produced from preprocessed dMRI and fMRI data, respectively, complex network analysis methods can be applied in a variety of neuroscientific applications. Whereas many of the analytic techniques have been adopted from network science, others have been exclusively proposed for brain network research, for example, the NBS approach (Zalesky et al., 2010).
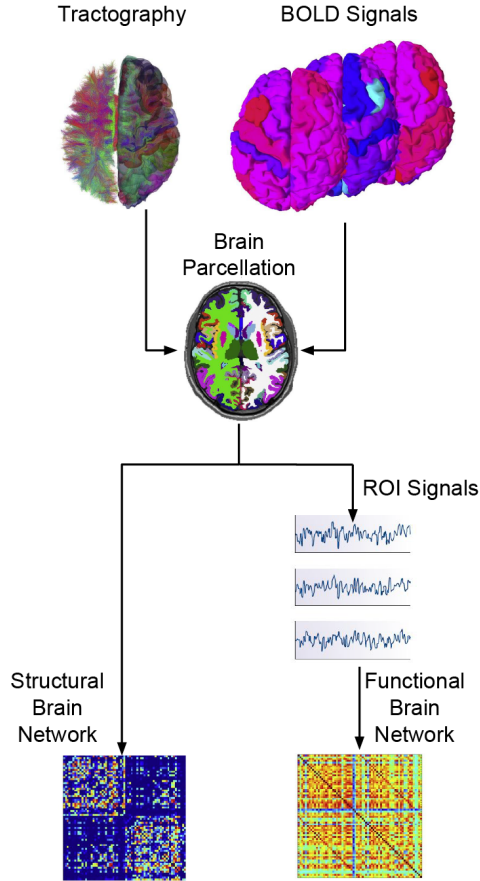
Figure 2.11. Construction of structural and functional brain networks. Structural connectivity is commonly inferred from the number of streamlines intersecting pairs of regions, although voxel-specific measures (*e.g.*, fractional anisotropy) can be used too. On the other hand, functional connectivity is estimated using measures of statistical dependence between time series recorded in brain areas. The time series from a particular ROI is computed as the average BOLD signal of those voxels composing the region. Adapted from Schirner et al. (2015).

Topological description of brain networks

Graph theoretical analyses have revealed that real-world networks, with brain networks being a particular instance, share common organizational principles. For example, earlier studies support that virtually all networks found in natural and technological systems have *small-world* attributes (Figure 2.12) (Bullmore and Sporns, 2009; Newman, 2003; Watts and Strogatz, 1998). Small-worldness indicates that a network combines high levels of local clustering among nodes, which is characteristic of regular networks, and short paths that globally link all nodes of the network, which is characteristic of Erdös-Rényi networks (commonly referred to as random networks). Thus, all nodes are linked through relatively few intermediate steps, despite the fact that most nodes maintain only a few direct connections. It is thought that this organization may constitute an optimal solution to the conflicting constrains of reducing wiring cost and facilitating information flow at the same time. Wiring cost is critical because the brain is a spatial network, that is, it is embedded in the real space wherein nodes occupy a precise location in a Euclidean space, and edges in structural brain networks are real physical connections (Barthélemy, 2011).
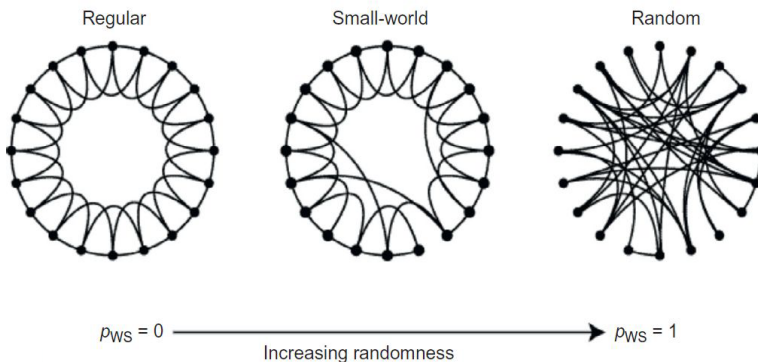
Figure 2.12. Small-world organization. Real-world networks are neither regular nor random, so they are characterized by both high levels of local clustering and short paths. Reproduced from Fornito et al. (2016).

Complex network measures can capture the topological organization at different levels, ranging from measures computed at node-level, to measures describing groups of nodes as well as aggregated measures computed at

network-level (Kaiser, 2011; Rubinov and Sporns, 2010; Stam, 2014). A basic measure is the degree (Figure 2.13a). The degree of a particular node is defined as the number of links connected to that node. In directed networks (Figure 2.13b), one can differentiate between the in-degree and the out-degree, which accounts for those links ending at and originating from an individual node, respectively. The degree does not make use of the weights, so the weighted version of the degree is the strength, which is defined as the sum of all neighboring edge weights. These metrics can be calculated at network-level by aggregating individual node values. More generally, measurement values of all individual elements provide a distribution, for example, the degree distribution of the network. Many real-world networks have degree distributions in the form of a power law, that is, the probability $P(k)$ that a node has k connections is given by $P(k) \sim k^{-\gamma}$. The exponent γ can vary depending on the network under study, although in most power-law systems, $2 < \gamma < 3$. Complex network with a degree distribution in this form are also known as *scale-free* networks. Scale-free networks are characterized by the presence of a subset of nodes with high centrality. Centrality quantifies the importance of a node relative to other nodes in the network. Degree is a centrality measure, but there are others such as closeness centrality and eigenvector centrality. Nodes with high centrality are also named *hubs* (van den Heuvel and Sporns, 2013).

In the brain, high-degree and topologically central hub regions tend to be highly interconnected. In fact, a central core of these hubs form a organization named *rich-club* (van den Heuvel and Sporns, 2011), which facilitates efficient communication between neural systems. The rich-club organization is also related to the *modular* organization of brain networks. The nodes of many real-world networks aggregate into densely connected subgroups called *modules* or *communities* (Figure 2.13c) (Fortunato, 2010; Fortunato and Hric, 2016; Sporns and Betzel, 2016). Nodes within these subgroups are more strongly connected to each other than with other parts of the network. In addition, modules possess a hierarchical organization, with subnetworks within networks. Interestingly, rich-club hubs are densely interconnected, facilitating intermodular organization and global integration (Figure 2.13d) (Park and Friston, 2013).
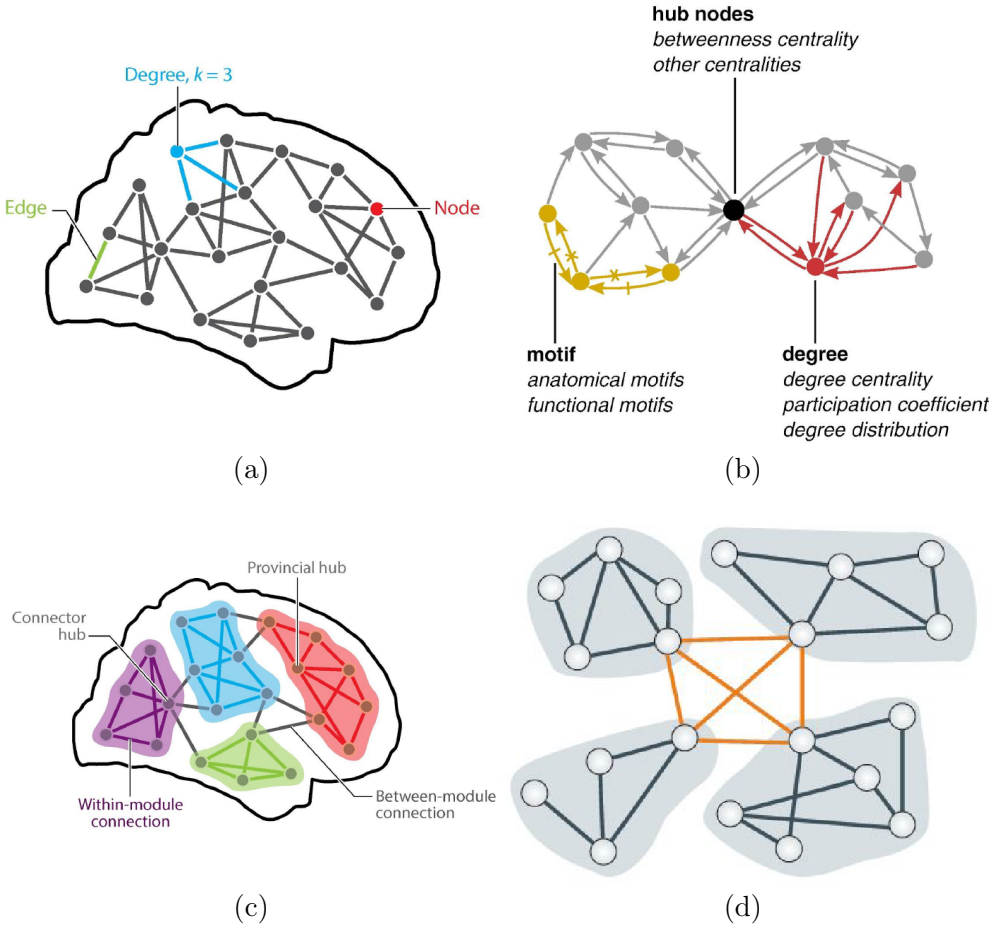
Figure 2.13. Some illustrative measures that quantifies the topology of complex networks. (a) The degree of a node is defined as the number of edges connected to that node. Reproduced from Sporns and Betzel (2016). (b) In directed network, one can compute both the in-degree (number of links going into a node) and out-degree (number of links leaving a node). Degree is a centrality measure and nodes with high centrality are called hub nodes or hubs. Network motifs are subgraphs with a particular topological configuration. Reproduced from Rubinov and Sporns (2010). (c) Brain networks possess a modular structure. Provincial hubs link primarily to other nodes in the same module, whereas connector hubs have links that are distributed across multiple different modules. Reproduced from Sporns and Betzel (2016). (d) Brain networks are also characterized by a rich-club organization, where a subset of hub nodes are highly interconnected, facilitating global communication. Reproduced from Fornito et al. (2015).

Dynamics in brain networks

A emergent trend in the study of brain networks is that of incorporating dynamics. As noted in section 2.2, network dynamics involve at least two dimensions (Bassett and Sporns, 2017): dynamics on networks and dynamics of networks. A clear example of the former is that of spreading process. Spreading describes many activities in real world, ranging from the spread of news and ideas in a social network, or the spread of contagious agents in a population (Pei and Makse, 2013). The position of a node in the network usually determines the spreading capabilities of that node. In neuroscience, spreading processes have been used to investigate how structural brain networks shape and constrain global dynamics of resting-state networks (Mišić et al., 2015), as well as to explain the progression to Alzheimer's disease (Iturria-Medina et al., 2014; Raj et al., 2012, 2015).

On the other hand, dynamics of networks build upon how changes in dynamics or function can produce changes in topology or structure. A particular application in neuroscience involves how connectivity between brain regions changes over the life span (Collin and van den Heuvel, 2013; Lim et al., 2015; Zhao et al., 2015). Indeed, changes in the connectome take place throughout prenatal development, early postnatal development, childhood, adolescence and adulthood. It has been suggested that connectome organization follows an inverted U-shape pattern, with a increasingly integrated topology during development, a plateau lasting for the majority of adulthood, and an increasingly localized topology in late life.

Measuring differences in brain networks

Whilst a quantitative description of healthy brain networks is an intriguing and necessary labor in and of itself in neuroscience, network science tools also provide a mean to investigate network alterations caused by distinct neurological and psychiatric disorders. For example, empirical and computational studies have revealed that lesion effects are critically dependent on the topological position of the lesion (Aerts et al., 2016). More concretely, damage to hubs causes the largest disturbances in network organization. In fact, neurodegenerative diseases, such as Alzheimer's disease, are characterized by the alteration of those nodes occupying a central role in the network (Tijms et al., 2013).

When investigating disruptions in brain networks between different conditions, one can compare complex network measures (*e.g.*, centrality and modularity),

but also edge weights themselves (Varoquaux and Craddock, 2013). The main drawback of the latter approach is the inherent massive number of multiple comparisons to be performed. Put simply, an undirected brain network with $N = 50$ nodes would imply to perform a total of $N(N-1)/2 = 1225$ comparisons (as much as the number of connections). If $N = 90$, the number of different connections to be compared would rise to 4005. With such a large number of multiple comparisons, mass-univariate testing may not offer sufficient power. In response to this limitation, alternative approaches have arisen. In particular, the NBS method attempts to take advantage of the connected nature of the brain under the premise that effects of interest are not confined to a single connection and node (Zalesky et al., 2010). Rather, changes on brain networks caused by pathology are likely to encompass multiple connections and nodes.

Machine learning methods, such as random forest (RF) (Breiman, 2001) and support vector machine (SVM) (Lemm et al., 2011) algorithms, offer an alternative and promising approach to investigate differences in brain networks. They rely on the extraction of distinctive features, which can represent topological properties as well as connection strengths. The power of these multivariate methods to decode brain signatures and predict clinical outcomes enable their application in a subject-specific manner for clinical applications (Woo et al., 2017). A plethora of studies have been published with the aim of predicting different disorders, including mild cognitive impairment (MCI) and Alzheimer's disease (Ebadi et al., 2017; Zhan et al., 2015), and autism spectrum disease (Yahata et al., 2016), among others. Additionally, feature selection algorithms (Guyon and Elisseeff, 2003; Saeys et al., 2007) can be wisely applied to extract potential biomarkers based on network measures. Note that predictive modelling does not suffer from the problem of multiple comparisons, although has to deal with other issues. Specifically, the proper application of resampling techniques (*e.g.*, cross-validation) to evaluate whether the resulting models generalize well across samples (Breiman, 2001; James et al., 2013; Pereira et al., 2009).

2.4   Summary

In this chapter, we have provided an overview about how network models can be applied to understand brain connectivity. In particular, we have discussed the network organization of the brain and surveyed the principal methodological aspects involved in the preprocessing, reconstruction and analysis of brain networks. Although we have focused on graphs

reconstructed from MRI data, network analysis tools themselves also apply to brain networks recorded with other techniques such as tracing technology, electroencephalography (EEG) and magnetoencephalography (MEG).

Brain connectivity can be described across three different dimensions (*i.e.*, structural, functional and effective) and represented by the corresponding connectivity matrix. The topology and dynamics of these matrices can be then investigated in health and disease. Depending on how brain connectivity is estimated, brain networks can encode binary/weighted and undirected/directed interactions. For example, the use of dMRI data enables investigating binary/weighted and undirected structural brain networks. By contrast, tracing data also provide information about the directionality of edges; although its application is limited to animal models due to its invasive nature. Functional and effective brain networks are estimated by using fMRI modality. Effective brain networks can be binary/weighted but are always directed by definition, as they represent causal influences between neural populations. Functional brain networks can be binary/weighted as well as directed/undirected, depending on how connectivity is estimated. For example, measures such correlation and mutual information offer undirected edges (the correlation between x and y is the same as the correlation between y and x), whereas other measures including Granger causality and transfer entropy allow estimating directed interactions. It is important to highlight that some authors consider the directed functional connectivity as being effective connectivity. Some measures based on Granger causality compute interactions directly from observable time series and do not make use of a biophysical generative model that accounts for the latent neural activity underlying BOLD signals (section 2.1). Therefore, strictly speaking, directed functional connectivity is not effective connectivity (Valdes-Sosa et al., 2011).

In the next three chapters we will conduct three different experiments based on the concepts introduced in this chapter. More concretely:

- Chapter 3 examines the community structure of undirected functional brain networks in health and its relationship with network measures of reciprocity and motifs calculated from a directed structural brain network (Díaz-Parra et al., 2017b).

- Chapter 4 makes use of machine learning algorithms based on centrality measures extracted from undirected structural brain networks to predict dementia caused by Alzheimer's disease (Díaz-Parra et al., 2018). Additionally, this chapter incorporates processes related to dynamics on networks as well as dynamics of networks.

■ Chapter 5 investigates alterations in edge weights of undirected functional brain networks in the context of alcohol use disorder by using the NBS approach (Díaz-Parra et al., 2017a).

Chapter 3

Structural and functional brain networks in the cerebral cortex of the rat

Connectomics data from animal models provide an invaluable opportunity to reveal the complex interplay between structure and function in the mammalian brain. In this chapter, we investigate the relationship between structural and functional connectivity in the rat brain cortex using a directed anatomical network generated from a carefully curated meta-analysis of published tracing data, along with rs-fMRI data obtained from a group of anesthetized Wistar rats.

The content presented in this chapter has been adapted from the following publication:

Díaz-Parra, A., Osborn, Z., Canals, S., Moratal, D., and Sporns, O. (2017). "Structural and functional, empirical and modeled connectivity in the cerebral cortex of the rat". *NeuroImage* 159, pp. 170–184.

3.1 Introduction

The study of brain connectivity from a network perspective (Newman, 2003; Strogatz, 2001) has become a promising framework to understand how action, perception, and cognition emerge from a dense ensemble of neural elements (Park and Friston, 2013). Leveraging advances in brain imaging and network science (Sporns, 2013; Sporns et al., 2005), recent approaches have focused on the topology and dynamics of large-scale projections linking anatomically distinct and functionally specialized brain regions (Bullmore and Bassett, 2011). The structure of these large-scale networks is thought to shape and constrain inter-regional interactions and computations.

Interactions between neuronal populations spanning brain-wide networks can be described using the structural, functional and effective connectivity. Whereas the interplay of these three modes of brain connectivity is not completely understood, some progress has been made by combining anatomy with both resting-state and task-based functional connectivity (Hermundstad et al., 2013). The analysis of spontaneous or intrinsic neural activity (Cole et al., 2010; Fox and Raichle, 2007) through using fluctuations in the BOLD signals of rs-fMRI enable examining the extent to which structural patterns shape functional interactions between neural assemblies (Honey et al., 2010). Previous studies have shown that the presence of strong structural connectivity, as measured with dMRI, between two areas increases the probability and strength of the corresponding functional connectivity. Nevertheless, it has also been reported that strong functional connectivity may exist between areas with no (direct) anatomical connections (Bowman et al., 2012; Damoiseaux and Greicius, 2009; Skudlarski et al., 2008), suggesting that indirect signaling and emergent dynamic processes make an additional strong contribution. For example, a study carried out in macaque cortex supports the idea that functional interactions are strongly influenced by network-wide effects (Adachi et al., 2012).

Connectomics data from animal models based on tract-tracing procedures allows in-depth characterization of structural brain networks. In contrast to MRI-based tractography, which provides coarse-grained undirected structural connectivity matrices, histological tracing technology yields highly resolved and directed connectivity information, hence providing important additional information (van den Heuvel et al., 2016a). For instance, recent work relating the structural connectome of the mouse brain and the intrinsic BOLD signal dynamics within individual brain regions has shown the importance of considering both the weight and directionality of structural connections (Sethi

et al., 2017). In addition, the mapping of functional brain networks in rodents provides an invaluable tool to understand the mechanisms behind neurological and psychiatric disorders for translational research (Gozzi and Schwarz, 2016; Pan et al., 2015). These experimental possibilities together with theoretical developments in network science are extending systems neuroscience from unimodal investigations of brain connectivity to a network-level understanding of structure-function interactions (Adachi et al., 2012; Diez et al., 2015; Goñi et al., 2014; Hsu et al., 2016; Mišić et al., 2016; Skudlarski et al., 2016; Stafford et al., 2014; Wang et al., 2015; Wirsich et al., 2016).

In this work, we examine the relationship between structural and functional connectivity in the rat cortical network. Using a detailed cortical structural connectivity matrix obtained from a carefully curated meta-analysis of published histological tracing data in rats (Bota et al., 2015), we first compare structural connections with their corresponding spontaneous correlations extracted empirically from rs-fMRI data collected in a group of 14 Wistar rats. We then show the results of this comparison taking into account network-level effects by relating structural properties of brain connectivity to the functional modularity of rs-fMRI networks. Specifically, we study link reciprocity in both intra- and inter-modular connections as well as the structural motif frequency spectrum within functionally defined modules. Overall, our results provide further evidence that rs-fMRI BOLD signal correlations are constrained and shaped by the underlying structural connectivity patterns.

3.2 Materials and methods

3.2.1 Animals and MRI acquisition protocol

Experiments were carried out in a horizontal 7 Tesla scanner with a 30 cm diameter bore (Biospec 70/30v, Bruker Medical, Ettlingen, Germany). The system had a 675 mT/m actively shielded gradient coil (Bruker, BGA 12-S) of 11.4 cm inner diameter. A 1H rat brain receive-only phase array coil with integrated combiner and preamplifier, no tune/no match, in combination with the actively detuned transmit-only resonator (BrukerBioSpin MRI GmbH, Germany) was employed. Data were acquired and processed with a Hewlett-Packard console running Paravision 5.1 software (Bruker Medical GmbH, Ettlingen, Germany) operating on a Linux platform.

For the rs-fMRI experiments, 14 Wistar rats were anesthetized with urethane (1.2 g/Kg). Anesthetized animals were placed in a custom-made animal holder

with adjustable bite and ear bars, and positioned on the magnet bed. The animals were constantly supplied with $0.8\,\mathrm{L/m}$ O2 with a face mask and temperature was kept between 36.5 and $37.5\,°\mathrm{C}$ through a water heat-pad. The temperature, heart rate, SpO2, and breathing rate were monitored throughout the session (MouseOx, Starr Life Sciences, Oakmont, US).

T2-weighted anatomical images were collected using a rapid acquisition with relaxation enhanced (RARE) sequence, applying the following parameters: field of view (FOV) = 40×40 mm^2; 15 slices; slice thickness = 1 mm; matrix size = 128×128; effective echo time (TEeff) = 56 ms; repetition time (TR) = 2 s; RARE factor = 8. The B0 field distribution in a large voxel ($40 \times 40 \times 40$ mm^3) containing the whole head was acquired. Briefly, the brain was localized with T2-weighted RARE sequence, and first- and second-order shims adjusted with MAPSHIM application in a sufficiently large voxel containing the whole brain. Functional MRI acquisition was performed using a gradient-echo (GRE)-echo-planar imaging (EPI) sequence in 30 coronal slices applying the following parameters: FOV = 25×25 mm^2; slice thickness = 0.5 mm; matrix size = 50×50; segments = 1; FA = $60°$; echo time (TE) = 15 ms; TR = 2000 ms (300 samples per run, 10 min), rendering an isotropic voxel of $0.5 \times 0.5 \times 0.5$ mm^3. Between one and three runs were acquired from each animal. T2-weighted anatomical images with exactly the same geometry were collected using a RARE sequence using the following parameters: FOV = 25×25 mm^2; 30 slices; slice thickness = 0.5 mm; matrix size = 200×200; TEeff = 56 ms; TR = 2 s; RARE factor = 8.

3.2.2 *Preprocessing of MRI data*

Data preprocessing within runs was carried out using *FSL v5.0* (FMRIB Software Library, `https://fsl.fmrib.ox.ac.uk/fsl/fslwiki/`) (Jenkinson et al., 2012) and MATLAB *2014a* (The MathWorks, Inc., Natick, MA, United States, `https://www.mathworks.com/`). Once images were converted to *NIfTI* (Neuroimaging Informatics Technology Initiative, `https://nifti.nimh.nih.gov/`) data format, the original voxel size, (x, y, z), was scaled up by a factor of 10. This step is very common when analyzing rodent data to accurately apply the same algorithms (largely those involving spatial transformations) as in human analyses (Kalthoff et al., 2013; Pan et al., 2015).

The very first volume of fMRI data was used as reference across runs of the same subject for head motion correction, brain extraction and co-registration. As suggested by Kalthoff et al. (2011), head motion correction was applied to each individual slice and restricted to (coronal) in-plane translations (x, y) and

rotation (z) to reduce signal fluctuations related to respiration in anesthetized rats. After applying motion correction and brain extraction (Smith, 2002), global intensity normalization was set to 1000 and spike detection was performed through using *DVARS* measure (Power et al., 2012). Note that *DVARS* is highly dependent on the particular dataset (Power et al., 2014), we therefore did not select an absolute threshold and instead considered as outliers those temporal points exceeding the 75th percentile $+ 1.5 \cdot$ IQR (interquartile range). None of the runs were discarded since the number of spikes was below 30 (out of 300 samples) in all cases (15 ± 4.6 spikes per run, mean $\pm$ SD), hence ensuring a minimum length of 9 min to estimate functional interactions. By using a nuisance regression model, each voxel was corrected for:

- The three rigid body parameters (translation in x and y, and rotation in z) previously computed and their derivatives (backward difference).

- A single regressor per spike with a "*b0, f0*" window (Satterthwaite et al., 2013) (*i.e.*, neither preceding nor following samples were used).

- The global signal and its derivative (backward difference).

- Two regressors modelling the mean and a linear trend.

A band-pass filtering (nonlinear high-pass filter with $\gamma = 50\,$s, and Gaussian linear low-pass filter with $\gamma = 2\,$s) was applied to retain those frequencies ranging from 0.01 and at around 0.1 Hz. Spatial smoothing was not applied to avoid introducing spurious high correlations between a node and its neighbors (Fornito et al., 2010). Finally, filtered rs-fMRI data were co-registered to the brain-extracted T2-weighted image using a rigid body transformation and then normalized to a rat template described elsewhere (Schwarz et al., 2006). Normalization was carried out through using an affine deformation (Jenkinson et al., 2002; Jenkinson and Smith, 2001) and the template was resampled to match the original resolution of functional images (*i.e.*, $0.5 \times 0.5 \times 0.5\,$mm^3).

3.2.3 Rat connectome and definition of brain areas

We made use of a directed anatomical network coming from a systematic curation of the primary neuroanatomical literature for the rat (for specific details as to annotation and collation methodology, see (Bota et al., 2015)). In particular, the dataset was originally composed of 73 cortical gray-matter regions that were defined according to the Swanson-04 hierarchical nomenclature for the rat central nervous system (Swanson, 2004). Connections in the rat cortical association macroconnections (RCAMs) matrix are encoded

by means of eight different ordinally arranged weight categories: *not present, very weak, weak, weak/moderate, moderate, moderate/strong, strong*, and *very strong*.

A critical point in neuroimaging research is the use of a common framework for localization of brain structures, which allows comparisons among results coming from different studies. Nomenclature of the rat connectome project is available in the SwS (Swanson, 2004) and structural connectivity between regions is directly given in matrix form, that is, no *Analyze* or *NIfTI* images are provided. On the other hand, to the best of our knowledge, the most complete atlas available in *Analyze* format (easily converted to *NIfTI* format) is that developed by Schwarz et al. (2006), where brain areas are given in the PWS (Paxinos and Watson, 1998). Therefore, the first task before carrying out network analysis was to establish a correspondence of brain regions between both spaces with the aim of aligning functional correlation matrices with the anatomical network. To this end, we carefully inspected both atlases as follows: (1) a particular reference brain region from SwS was localized in its corresponding coronal plane; (2) we sought the coronal slice/s in PWS containing the previous region, and (3) by taking into account the spatial distribution of surrounding areas as well as the relative anterior and posterior planes, we identified which region or group of regions from PWS matched with the reference region.

As not all of the original structures contained in the RCAMs matrix were available in the *NIfTI* atlas as a single mask, some of them were grouped to cover the whole brain cortex (Figure 3.1 schematizes the process carried out for computing these new connections). Thus, we created a new pattern of cortical connections for the secondary visual area (VISs), which was composed of the original anterior laterolateral area (VISlla), anterolateral area (VISal), rostrolateral area (VISrl), intermediolateral area (VISli), laterolateral area (VISll), mediolateral area (VISlm), posterolateral area (VISpl), and anteromedial area (VISam). The tenia tecta cortical region (TT) was composed of the dorsal and ventral parts (TTd and TTv, respectively). Interactions of the retrosplenial area ventral part (RSPv) with other areas were obtained from the original ventral part (RSPv), ventral part zone a (RSPv-a), and ventral part zone b/c (RSPv). The hippocampal region was partitioned into dorsal and ventral parts as follows. The dorsal part of the hippocampal region (HIPd) was composed of CA1 dorsal part (CA1d), CA3 dorsal part (CA3d), CA2 dorsal part (CA2d), dentate gyrus dorsal part (DGd), and induseum griseum (IG). Whereas the ventral part of the hippocampal region (HIPv) was composed of CA1 ventral part (CA1v), CA3 ventral part (CA3v),

CA2 ventral part (CA2v), and dentate gyrus ventral part (DGv). Note that the current RCAMs matrix does not distinguish between dorsal and ventral parts for CA2, CA3 and DG. To overcome this limitation, and with the aim of including the whole hippocampal region in our analysis, structural patterns contained in the rat connectome for CA2, CA3 and DG were assumed to be equal for both ventral and dorsal parts. Categorical weight for the same region in different parts (*e.g.*, between CA2d and CA2v) were assumed to be very strong. A new pattern of structural connections was also created for the cortical amygdalar nucleus (COA), which was formed from the anterior part (COAa), posterolateral part (COApl), and posteromedial part (COApm). The secondary auditory areas (AUDs) was composed of the ventral and dorsal auditory areas (AUDd and AUDv, respectively). The medio-ventral part of the orbital area (ORBmv) included the ventral and medial parts (ORBv and ORBm, respectively). The presubiculum (PRE) and parasubiculum (PAR) were grouped to form the PreParaSubiculum region (PREPAR). The basolateral amygdalar nucleus (BLA) was composed of the anterior and posterior parts (BLAa and BLAp, respectively). Finally, structural interactions between the basomedial amygdalar nucleus (BMA) and the rest of nodes were obtained from the anterior and posterior parts (BMAa and BMAp, respectively).
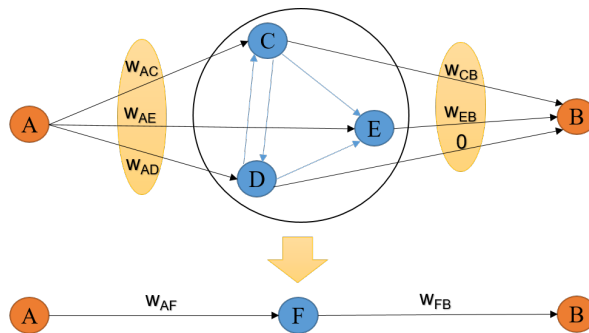
Figure 3.1. Illustration of the process applied for combining brain areas of the RCAMs matrix. Ordinal weights were converted to numerical values and ranked on a linear scale from 0 (*not present*) to 7 (*very strong*). We then calculated the mean of those links entering to and leaving from a new aggregated gray-matter region. Finally, we rounded the mean value to the nearest integer with the aim of keeping the original weight classification. For instance, $w_{AF} \approx (w_{AC} + w_{AE} + w_{AD})/3$ in the figure.

Definition of nodes is a very important step for brain network analysis. Based on the just described procedure and the information available in the *NIfTI* atlas, we generated a brain parcellation of 32 ROIs. Table 3.1 presents the brain regions from SwS and their counterpart regions from PWS.

3.2.4 Construction of functional brain networks

The mean time courses within each of the 32 ROIs were extracted and converted to z-scores (*i.e.*, fMRI BOLD time series were centered and scaled to have zero mean and unit variance). As the current RCAMs matrix (Bota et al., 2015) does not differentiate between hemispheres, voxels within ROIs were also combined across hemispheres (Figure 3.2 presents a seed-based correlational analysis in two different brain regions uncovering bilateral networks in the dataset). That is, the time course from a given region, say the primary somatosensory area, was obtained as the average between signals from right and left primary somatosensory areas. Importantly, to create a homogeneous parcellation by ensuring that all regions had the same size, we adopted the procedure carried out by Alexander-Bloch et al. (2012), where ROIs were eroded until all of them had exactly the same volume, $1\,\mathrm{mm}^3$ here ($0.5\,\mathrm{mm}^3$ in each hemisphere). Before computing functional interactions, time samples marked during preprocessing were "scrubbed". Functional networks were then estimated for each single run by computing the Pearson correlation coefficient. Next, raw correlations were converted to Fisher's z-values and connectivity matrices of each run were averaged within subject. Finally, functional connectivity matrices across the 14 subjects were averaged and a group network was obtained and then used for comparative analysis with the RCAMs matrix.

3.2.5 Modularity

Community structure detection involves the partition of a network into "modules" or "clusters" wherein nodes are highly connected to each other and only sparsely connected with nodes of different modules (Newman and Girvan, 2004). In neuroscience applications, community detection allows the grouping of neural elements (*e.g.*, brain regions) of both anatomical and functional networks into distinct modules (Figure 2.13c) (Sporns and Betzel, 2016). Despite the fact that community detection is conceptually straightforward, its application is methodologically challenging as indicated by the large number of algorithms and approaches dealing with it (Fortunato, 2010; Fortunato and Hric, 2016). Whereas it is also possible to perform graph partition

Table 3.1. Cortical brain regions from SwS and their counterpart regions from PWS used as network nodes.

Swanson structure	Abbreviation	Paxinos&Watson structure	Abbreviation
Primary somatomotor area	MOp	Primary motor cortex	M1
Secondary somatomotor areas	MOs	Secondary motor cortex	M2
		- Primary somatosensory cortex	S1
		- Primary somatosensory cortex, barrel field	S1BF
		- Primary somatosensory cortex, dysgranural region	S1DZ
		- Primary somatosensory cortex, forelimb region	S1FL
Primary somatosensory area	SSp	- Primary somatosensory cortex, hindlimb region	S1HL
		- Primary somatosensory cortex, jaw region	S1J
		- Primary somatosensory cortex, jaw region, oral surface	S1JO
		- Primary somatosensory cortex, trunk region	S1Tr
		- Primary somatosensory cortex, upper lip region	S1ULp
Supplemental somatonsensory area	SSs	Secondary somatosensory cortex	S2
Visceral area	VISC	Granular insular cortex	GI
Infralimbic area	ILA	Infralimbic cortex	IL
Gustatory area	GU	Dysgranular insular cortex	DI
		- Anterior olfactory nucleus, dorsal part	AOD
		- Anterior olfactory nucleus, external part	AOE
Anterior olfactory nucleus	AON	- Anterior olfactory nucleus, lateral part	AOL
		- Anterior olfactory nucleus, medial part	AOM
		- Anterior olfactory nucleus, posterior part	AOP
		+ Tenia tecta, layer 1	TT1
Tenita tecta	TT	+ Tenia tecta, layer 2	TT2
		+ Tenia tecta, layer 3	TT3
		- Piriform layer	Pir
		- Region external to piriform layer	Pir/ext
Piriform area	PIR	- Region internal to piriform layer	Pir/int
		- Piriform cortex	PirCtx
		- Cortex amygdala transition zone	CxA
Primary auditory area	AUDp	Primary auditory cortex	Au1
Secondary auditory areas	AUDs	- Secondary auditory cortex, dorsal area	AuD
		- Secondary auditory cortex, ventral area	AuV
		+ Secondary visual cortex, lateral area	V2L
Secondary visual area	VISs	+ Secondary visual cortex, mediomedial area	V2MM
		+ Secondary visual cortex, mediolateral area	V2ML
Primary visual area	VISp	- Primary visual cortex, binocular area	V1B
		- Primary visual cortex, monocular area	V1M
Anterior cingulate area, dorsal part	ACAd	Cingulate cortex, area 1	Cg1
Anterior cingulate area, ventral part	ACAv	Cingulate cortex, area 2	Cg2
Prelimbic area	PL	Prelimbic cortex	PrL
Orbital area, medio-ventral part	ORBmv	- Medial orbital cortex	MO
		- Ventral orbital cortex	VO
Orbital area, ventrolateral part	ORBvl	Lateral orbital cortex	LO
Agranular insular area, dorsal part	AId	Agranular insular cortex, dorsal part	AID
Agranular insular area, ventral part	AIv	Agranular insular cortex, ventral part	AIV
Agranular insular area, posterior part	AIp	Agranular insular cortex, posterior part	AIP
Retrosplenial area, dorsal part	RSPd	Retrosplenial granular B cortex	RSGb
Retrosplenial area, lateral agranular part	RSPagl	Retrosplenial agranular cortex	RSA
Retrosplenial area, ventral part	RSPv	Retrosplenial granular A cortex	RSGa
Posterior parietal association areas	PTLp	Parietal association cortex	PtA
Postsubiculum	POST	Postsubiculum	Post
Subiculum, dorsal part	SUBd	Subiculum, dorsal part	DS
		- Hippocampus posterior, dorsal part	HCpd
		- Hippocampus fronto dorsal	HCfd
Hippocampal region, dorsal part	HIPd	- Dentate gyrus, dorsal part	DGd
		- Field CA3 of hippocampus, dorsal part	CA3d
		- Indusium griseum	IG
		+ Hippocampus posterior, ventral part	HCpv
Hippocampal region, ventral part	HIPv	+ Field CA3 of hippocampus, ventral part	CA3v
		+ Dentate gyrus, ventral part	DGv
Claustrum	CLA	Claustrum	Cl
Endopiriform nucleus, dorsal part	EPd	Dorsal endopiriform nucleus	Den

with overlapping modules, we only consider in this chapter the detection of non-overlapping modules.

One popular approach for community detection attempts to maximize a quality function, Q, commonly known as the *modularity function*. The problem of community detection can be formalized as:

$$Q = \sum_{i,j} [w_{ij} - p_{ij}] \, \delta \, (\sigma_i, \sigma_j) \, . \tag{3.1}$$
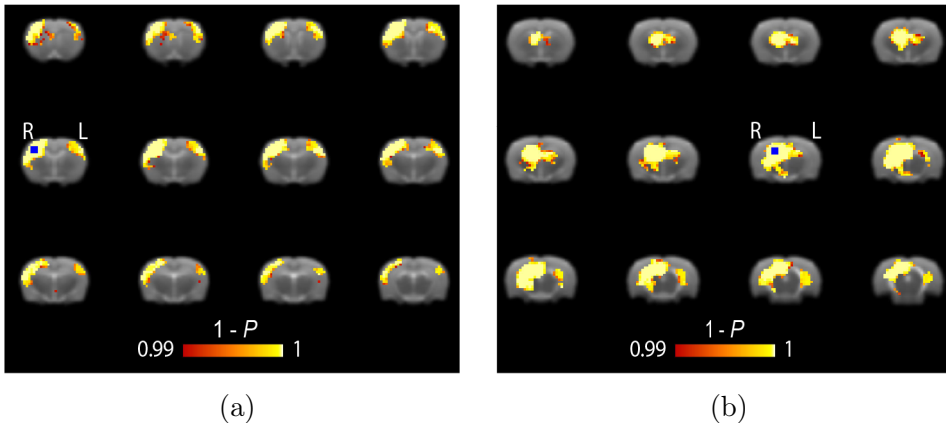
Figure 3.2. **Seed-based correlational analysis**. Intrinsic functional connectivity, as measured with Fisher's z-values of Pearson correlations, using as seeds the primary somatosensory area (a) and the dorsal part of the hippocampal region (b) (3×3 right seed region is shown in blue). The same pipeline as explained in subsection 3.2.2 was applied. Additionally, functional images were smoothed with a 1 mm (two times voxel resolution) full-width at half-maximum Gaussian kernel, as typically performed in voxel-wise analyses. Functional connections were thresholded at uncorrected $P < 0.01$.

In the Equation (3.1), w_{ij} represents the actual weight of the connection between node i and j, whereas p_{ij} refers to a specified null network model so that nodes within communities are internally more connected than expected by chance. The term $\sigma_i \in [1, \ldots, L]$ stands for the assignment of the node i to the l_{th} module, and the Kronecker function, $\delta(\sigma_i, \sigma_j)$, is equal to unity when

node i and j belong to the same community, $\sigma_i = \sigma_j$, and zero otherwise. Thus, only nodes belonging to the same community contribute to maximize Q. The modularity function is typically modified by including a constant factor before summation with the aim of setting the maximum of the quality function to one. This last step has no influence on the final partition, though.

The precise value of the null model, p_{ij}, relies strongly on the nature of the network being analyzed. Traditionally, the most popular null model is the *configuration model*, represented by the following expression:

$$p_{ij} = \frac{k_i \, k_j}{2m}, \tag{3.2}$$

with $k_i = \sum_j w_{ij}$ and $2m = \sum_{i,j} w_{ij}$. However, it has recently been shown that approaches using the Equation (3.2) can lead to biased results when correlation matrices are considered (Bazzi et al., 2016; MacMahon and Garlaschelli, 2015). We therefore made use of a different null model known as the *constant Potts model* (Traag et al., 2011). This approach is named constant because the connection weight in Equation (3.1) is compared to a tunable parameter, γ:

$$p_{ij} = \gamma. \tag{3.3}$$

By varying gamma, one is able to reveal community structure at different scales (given by the number of communities and their size), hence mitigating the problem known as the *resolution limit* (Fortunato and Barthélemy, 2007).

In this work, we used 109 different gamma values ranging linearly from -0.02 to 0.25 in increments of 0.0025 and, for each of them, we ran the Louvain algorithm $10,000$ times (Blondel et al., 2008). After optimizing Q, we computed the mutual similarity, as quantified by using the z-score of the Rand index (z-Rand), over all pairs of partitions within a given setting of γ (Traud et al., 2011). We then obtained a consensus partition for each γ (Bassett et al., 2013; Lancichinetti and Fortunato, 2012).

3.2.6 Reciprocity

Link reciprocity is a network measure that allow assessing the tendency of node pairs to form mutual connections between each other, and whose definition has been extended for weighted networks (Squartini et al., 2013). Formally, it is possible to define the *reciprocated* weight between node i and j (the symmetric part) as:

$$w_{ij}^{\leftrightarrow} \equiv \min[w_{ij}, w_{ji}] = w_{ji}^{\leftrightarrow}, \tag{3.4}$$

and the *non-reciprocated* weight from node i to j (the asymmetric part) as:

$$w_{ij}^{\rightarrow} \equiv w_{ij} - w_{ij}^{\leftrightarrow}. \tag{3.5}$$

Figure 3.3 presents a basic decomposition of any dyadic interaction (*i.e.*, between two nodes). The *weighted reciprocity*, r, is then computed as the ratio between the *total reciprocated weight*, $\sum_{i,j} w_{ij}^{\leftrightarrow}$, and the total weight of the network, $\sum_{i,j} w_{ij}$. Afterwards, this quantity is scaled relative to the average weighted reciprocity derived from a null network model, $\bar{r}_{\text{null}}$, as follows:

$$\lambda \equiv \frac{r - \bar{r}_{\text{null}}}{1 - \bar{r}_{\text{null}}}, \tag{3.6}$$

where λ indicates the tendency of the network to reciprocate ($\lambda > 0$) or to avoid reciprocation ($\lambda < 0$). In this work, λ was computed by generating $5,000$ random networks preserving the in- and out-degree sequences as well as the total strength of the real network. As our main interest was to compare weighted intra-modular (a)symmetries compared to those taking place between modules, the measure λ was computed separately for each type of link. Put simply, by imposing the partition of functional modules on the weighted anatomical matrix, we studied whether modularity obtained from rs-fMRI data showed differences in link reciprocity between intra- and inter-modular projections.
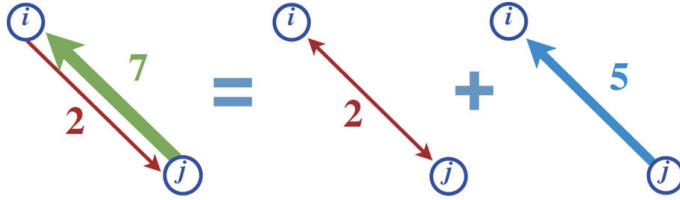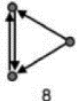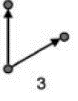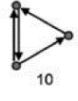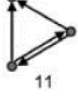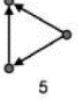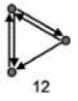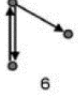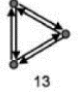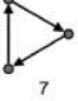
Figure 3.3. Weighted reciprocity. Dyadic interactions ($w_{ij} = 2$ and $w_{ji} = 7$ in the figure) can be decomposed into a fully reciprocated component ($w_{ij}^{\leftrightarrow} = w_{ji}^{\leftrightarrow} = 2$) and a fully non-reciprocated component ($w_{ji}^{\rightarrow} = 5$, which implies $w_{ij}^{\rightarrow} = 0$). Reproduced from Squartini et al. (2013).

3.2.7   Network motifs

The dynamic behavior of a complex system relies critically on the underlying interconnections and how nodes are linked to form specific subgraphs or network motifs (Milo et al., 2002). The existence of these "building blocks" can be recognized in many directed real-world networks such as biological and technological networks, as compared with randomized networks. Motif analysis has been applied in a variety of brain networks to identify motifs that are significantly increased in frequency over various null models (Sporns and Kötter, 2004; van den Heuvel et al., 2012; Varshney et al., 2011). In contrast to link reciprocity, which is a measure quantifying second-order topological properties, networks motifs examine higher-order connectivity patterns.

The total number of different subgraphs or network motifs depends on the number of nodes being considered. For instance, for structural motifs of size $M = 3$ (third-order topological properties) there are 13 different possible alternatives or classes through which three nodes can be linked (Table 3.2). Previous studies have addressed the problem of modularity by clustering subgraphs or higher-order connectivity patterns (Arenas et al., 2008; Benson et al., 2016), rather than considering dyadic interactions. Interestingly, this framework, whereby community structure detection and network motif approaches are related, can reveal new insights into the topological organization of complex networks. In this work, we were interested in the higher-order structural organization within functionally defined modules. Inspired by the *motif modularity* (Arenas et al., 2008), we calculated the ratio of the number of occurrences (summarized in the motif frequency spectrum) for a given motif class i restricted to within communities, fwm_i, to the motif frequency spectrum computed over the whole network for the same class, f_i:

Table 3.2. The 13 different structural motif classes that can be obtained for motifs of size $M = 3$, along with the number of functional instances that can generates.

Structural motif class	Number of functional motifs	Structural motif class	Number of functional motifs
1	1	8	10
2	1	9	9
3	1	10	10
4	3	11	10
5	4	12	24
6	3	13	54
7	4		

$$F_i = \frac{fwm_i}{f_i}. \tag{3.7}$$

We calculated the normalized motif frequency spectrum for structural motifs of size $M = 3$. In this way, we could study whether modules obtained from functional data are associated with a specific pattern of intra-modular anatomical connections. Binary motif analysis was performed for three connectivity levels of structural connectivity: (1) keeping all connections, (2) removing *very weak* links, and (3) removing both *very weak* and *weak/moderate* links.

The observed value F_i was statistically compared against an ensemble of null networks ($5,000$ samples) preserving the number of incoming edges, outgoing edges and mutual edges of each node of the actual network (Milo et al., 2002). Generating null models preserving mutual edges allows us to ascertain that higher-order patterns does not simply emerge as a result of lower-order properties (*e.g.*, link reciprocity), but the abundance of networks motifs inside communities is a feature of real-world networks. Thus, we calculated F_{i_null} for each reference network, and we eventually obtained a null distribution that allowed us to statistically evaluate the fraction of every motif class within communities using the z-score, z_i, as follows:

$$z_i = \frac{F_i - \bar{F}_{i\_\mathrm{null}}}{\sigma_{F_{i\_\mathrm{null}}}}. \tag{3.8}$$

with $\bar{F}_{i\_\mathrm{null}}$ and $\sigma_{F_{i\_\mathrm{null}}}$ representing the average and standard deviation of the null distribution, respectively.

3.3 Results

3.3.1 Characterization of structural connectivity and rs-fMRI-derived functional connectivity

Categorical weights of the RCAMs matrix (Bota et al., 2015) were encoded between 0 (*not present*) and 7 (*very strong*) (Figure 3.4a top panel). Out of the 32 selected regions defined for the cortex, 49.8 % of the possible pair-wise structural connections were *not present*, 7.2 % were *very weak*, 8.6 % *weak*, 6.7 % *weak/moderate*, 10.2 % *moderate*, 5.9 % *moderate/strong*, 8.8 %

strong, and only 2.8 % *very strong* (Figure 3.4a bottom panel). These values confirmed the overall sparsity of the structural network. We next derived the functional connectivity within the same set of brain regions, computed as the correlation between the average BOLD signals (Figure 3.4b top panel). As expected, pair-wise functional interactions between the 32 regions included negative correlations, with functional connectivity values following a slightly right skewed and unimodal distribution with a pronounced peak around zero (Figure 3.4b bottom panel).

Although different studies have revealed that wiring minimization itself cannot account for all topological features of structural and functional networks (Betzel et al., 2016; Vértes et al., 2012), the essential role of physical distances between pairs of nodes is widely recognized. We plotted the pair-wise structural connectivity and functional connectivity values as a function of distance (approximated through the Euclidean distance) and found that both structural connectivity and functional connectivity values tend to be higher between brain regions separated by short distances (Figure 3.5).

With the aim of investigating the relationship between the structural connectivity and the rs-fMRI-measured functional connectivity in the rat cortex, we first calculated the association between anatomical and functional matrices (Figure 3.6). The Spearman correlation, ρ, quantified to what extent the strength of a structural connection predicted the corresponding functional connection between two regions. Using all possible value pairs in the structural connectome (*i.e.*, *present* and *not present*) and the functional matrix, we obtained a Spearman (rank-order) correlation of $\rho = 0.48\,(P < 2 \times 10^{-29})$ between the structural and functional networks. The Spearman correlation did not vary after removing all node pairs for which an anatomical connection was found to be *not present*, $\rho = 0.48\,(P < 2 \times 10^{-19})$. This result reveals a strong positive linear association between structural connectivity and functional connectivity matrices. In addition, we also calculated the association between both networks while controlling the effect of the Euclidean distance. In this case, the Spearman correlation dropped to $\rho = 0.35\,(P < 3 \times 10^{-15})$ and $\rho = 0.33\,(P < 2 \times 10^{-9})$, relative to the total or zero weight-corrected structural matrix, respectively, supporting the role of geometric distances between region pairs in brain network organization. Functional connectivity patterns without global signal regression and the relationship with the structural matrix are shown in Figure 3.7.
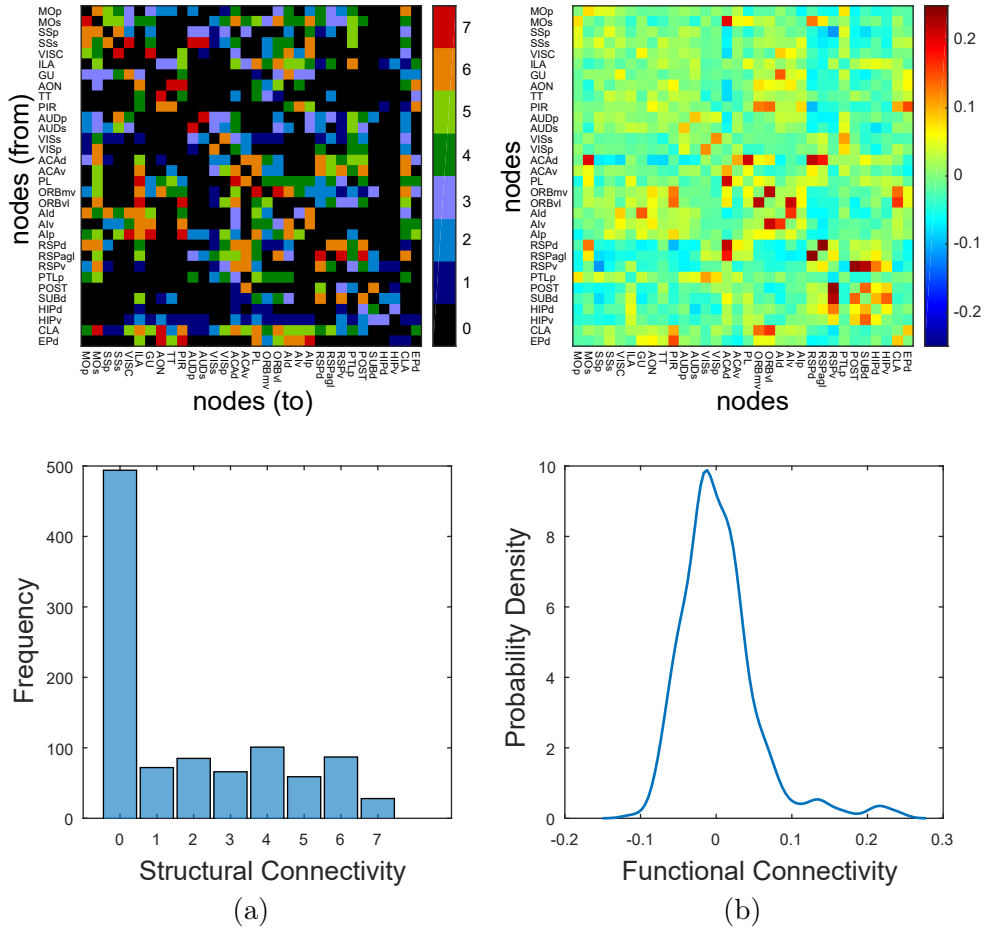
Figure 3.4. Structural and empirical functional brain networks of the rat cortex.
(a) RCAMs matrix built from Bota et al. (2015) (top panel), and histogram of the weight
distribution (bottom panel). Color scale represents the categorical weights of structural links
(0, *not present*; 1, *very weak*; 2, *weak*; 3 *weak/moderate*; 4, *moderate*; 5, *moderate/strong*; 6,
strong; 7, *very strong*). (b) Functional connectivity between pairs of ROI time courses (top
panel), and probability density estimate of the Fisher's z-values (bottom panel). Color scale
represents the strength of functional interactions between pairs of nodes.

(a)

(b)
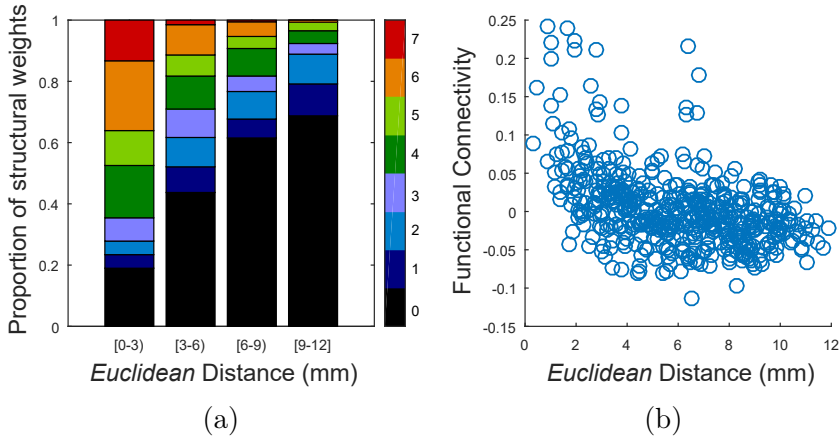
Figure 3.5. Relationship between Euclidean distance and brain connectivity.
Pair-wise structural (a) and functional (b) connections as a function of the Euclidean distance
between pairs of ROIs. Each dot represents a particular functional connection between pairs
of nodes. Euclidean distances were measured between centers of mass.
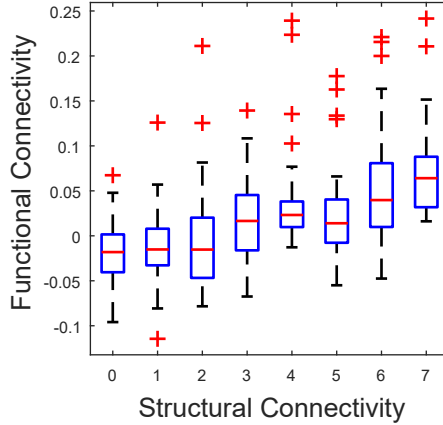
**Figure 3.6. Pair-wise functional interactions as a function of the underlying
structural connections**. Box and whiskers plots representing the median (horizontal red
line), first, Q_1, and third, Q_3, quartiles (blue box), as well as the lower and upper (black)
whiskers of the functional connections. Those values greater than $Q_3 + 1.5 \cdot (Q_3 - Q_1)$ or
lower than $Q_1 - 1.5 \cdot (Q_3 - Q_1)$ were considered as outliers (red crosses).

(a)

(b)

(c)

(d)
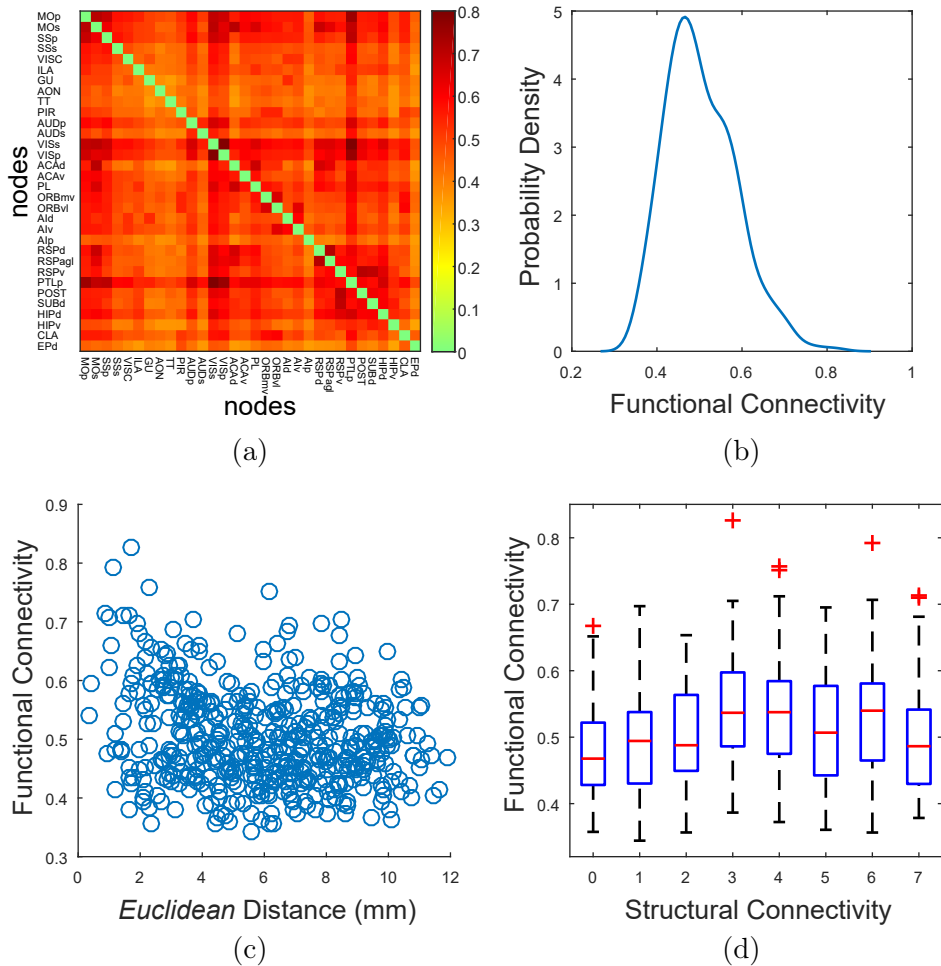
Figure 3.7. **Comparison between structural connectivity and functional connectivity matrices without global signal regression**. (a) Functional connectivity between pairs of BOLD time courses. (b) Probability density estimate of the Fisher's z-values. (c) Pair-wise functional connections as a function of the Euclidean distance between ROIs. (d) Pair-wise functional interactions as a function of the underlying structural connections. We obtained a Spearman (rank-order) correlation of $\rho = 0.26\,(P < 5 \times 10^{-9})$ between the structural and functional brain networks. After removing all node pairs for which an anatomical connection was found to be *not present*, the Spearman correlation dropped to $\rho = 0.16\,(P = 0.005)$.

3.3.2 Relationship between functional modules and structural network-level patterns

Partitioning a network or graph into components offers the ability to uncover modules at different spatial scales. Indeed, each module or component can be interpreted as a subnetwork itself. Figure 3.8a shows the number of communities extracted from the functional data along with the value of the modularity function (which represents the quality of the obtained consensus partition), and the consistency of the partitions by means of the similarity of the modules generated in $10,000$ iterations (see subsection 3.2.5). Given that different community structures might be equally feasible and plausible, we investigated the distribution of motif classes within functionally define modules at different scales of resolution, rather than targeting a unique partition. We examined structural patterns at $\gamma = -0.0125$ (Figure 3.8b), $\gamma = 0.005$ (Figure 3.8c), and $\gamma = 0.02$ (Figure 3.8d). These parameter settings were selected for several reasons. First, these scales were located within intervals of γ values where the number of communities remained relatively constant, hence yielding partitions with two ($\gamma = -0.0125$), three ($\gamma = 0.005$) and five ($\gamma = 0.02$) communities. Second, given a number of communities, the selected scales were the most stable partitions, as indicated by a high mean and a low variance of the z-Rand index. Finally, we did not explore functional partitions beyond $\gamma = 0.02$ because the resulting partitions yielded numerous modules of very small size, which makes motif analysis impractical. For example, at $\gamma = 0.035$, the cortex was partitioned into eight modules, with three modules of three nodes, one module of two nodes, and another singleton module.

At the most coarse scale ($\gamma = -0.0125$), the cortex was partitioned into two modules (Figure 3.8b). The wider module (M1) contained most regions of the sensory-motor cortex including the primary somatomotor (MOp), somatosensory (SSp, SSs), visceral sensory-motor (VISC, ILA), gustatory (GU), olfactory (AON, TT, PIR), auditory (AUDp, AUDs), and visual areas (VISs, VISp). Association areas such as orbital (ORBmv, ORBvl), agranular insular (AId, AIv, AIp) and posterior parietal (PTLp), together with the cortical subplate, namely, claustrum (CLA) and the dorsal part of the endopiriform nucleus (EPd) were grouped in the same module. On the other hand, the second module (M2) brought together all parts of the hippocampal formation included in this analysis (HIPv, HIPd, SUBd, POST) as well as retrosplenial (RSPv, RSPagl, RSPd), prelimbic (PL), and anterior cingulate (ACAv, ACAd) areas. Along with these association structures, only one sensory-motor region was included, namely, the secondary somatomotor region (MOs). As the resolution parameter was increased ($\gamma = 0.005$), the cortex was
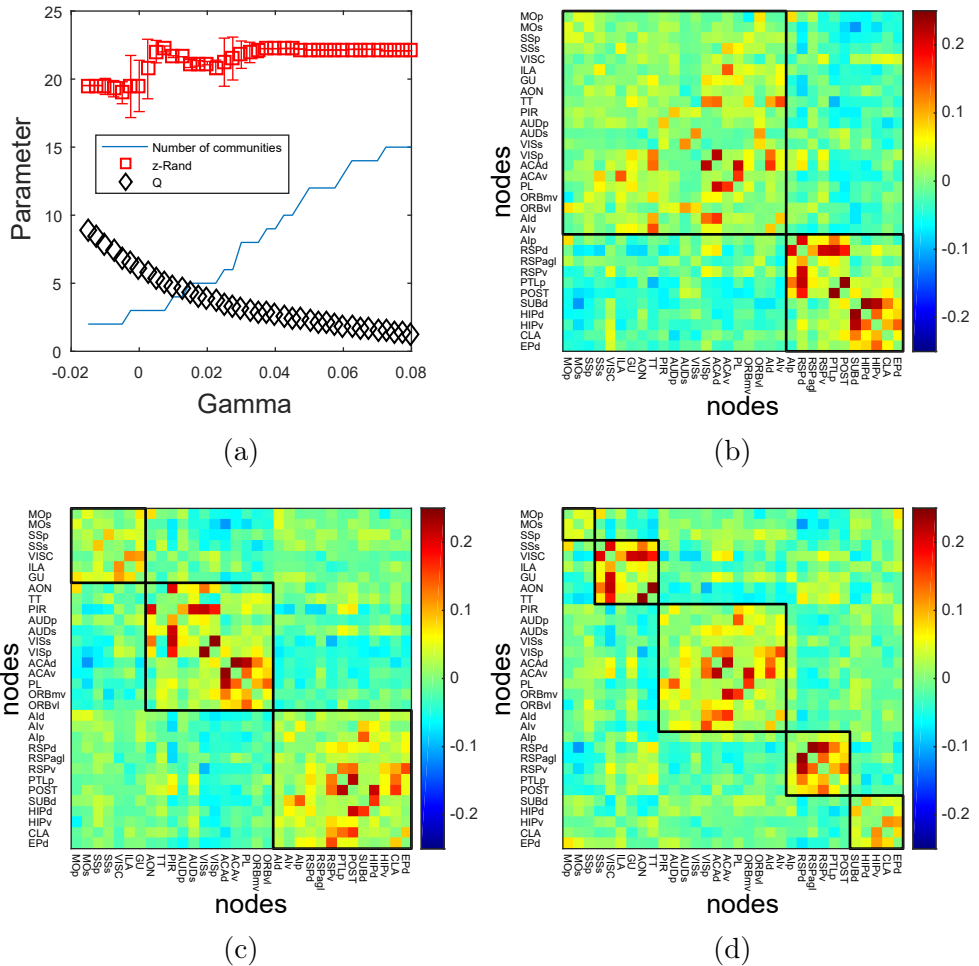
Figure 3.8. **Community structure of the rat cortex**. (a) Different properties were computed at various γ levels (Louvain algorithm was run $10,000$ times): number of communities, modularity function (Q) (measuring the quality of the obtained consensus partition), and mean and variance of the z-score of the rand indices (z-Rand) (measuring the similarity over all pairs of partition within scales). Partitions below -0.015 and above 0.24 were unstable. For clarity, only scales in the range $[-0.015, 0.08]$ are shown, and Q was rescaled between 0 and 10. (b) Functional partition obtained at $\gamma = -0.0125$ (two communities). (c) Functional partition obtained at $\gamma = 0.005$ (three communities). (d) Functional partition obtained at $\gamma = 0.02$ (five communities).

split into three functional modules (Figure 3.8c). The previous module M1 was divided into two different modules, whereas M2 remained largely intact, with only the infralimbic area relocated from M1 into M2. Finally, at the finer scale ($\gamma = 0.02$), a total of five modules were obtained (Figure 3.8d). In this case, the original module M1 was partitioned into three communities and M2 into two. Again, the infralimbic area was relocated within module M2.

The next part of our analysis focused on investigating structural connections and their relationship with functional modularity. Regardless of the resolution scale, both intra- and inter-modular links showed positive reciprocity, indicating that brain regions tend to be mutually connected within and between modules. However, when comparing reciprocity between both types of link, connections of the RCAMs matrix within communities showed a stronger reciprocity compared to projections connecting nodes from different modules: 0.506 *vs.* 0.275, 0.534 *vs.* 0.304, and 0.575 *vs.* 0.326 when the brain cortex was partitioned into two, three, and five modules, respectively. We next investigated the density of each of the 13 potential motif classes associated with structural motifs of size 3 within functionally identified modules and for the selected scales (Figure 3.9, Figure 3.10 and Figure 3.11). We obtained a very high z-score for motif class 13 for all partitions and for all connectivity levels investigated (when keeping all connections, when removing *very weak* links, and when removing both *very weak* and *weak/moderate* links), indicating that this maximally densely connected structural motif is significantly enriched within functional communities. Comparable results were obtained for motif class 12 for scales $\gamma = 0.005$ (Figure 3.10) and $\gamma = 0.02$ (Figure 3.11), and for $\gamma = -0.0125$ (Figure 3.9) after deletion of *very weak* links and of both *very weak* and *weak/moderate* links. A few other motif classes were significant at $z > 3.7$ ($P < 0.0001$), for example motif class 10 and 11 for scales $\gamma = 0.005$ and $\gamma = 0.02$ and only when removing both *very weak* and *weak/moderate* links. Regardless of the considered scale and connectivity level, the significance level of all other motif classes was $z \leq 3.7$.

3.4 Discussion

The study of structure and function at the large-scale in rodent animals offers the possibility to understand the mechanisms underlying psychiatric and neurological disorders for subsequent translation research (Gozzi and Schwarz, 2016; Jonckers et al., 2015). Nevertheless, knowing and describing the healthy rodent brain connectivity is the first step for that endeavor. The organizational principles of the rat and mouse structural networks have been
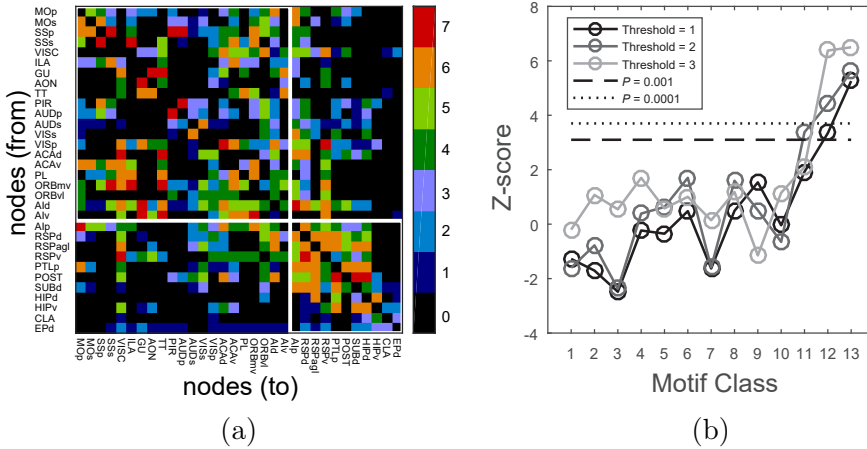
Figure 3.9. **Network motif analysis at** $\gamma = -0.0125$. (a) Functionally obtained partition is imposed over the RCAMs matrix. (b) Statistical evaluation of each of the 13 structural motifs classes is shown for different binarized versions of the structural matrix, namely, when keeping all connections (Threshold = 1), removing *very weak* links (Threshold = 2), and removing both *very weak* and *weak/moderate* links (Threshold = 3).

previously described (Bota et al., 2015; Oh et al., 2014; Swanson et al., 2016; van den Heuvel et al., 2016b). Comparisons between the mouse connectome and rs-fMRI connectivity have revealed that both networks are intimately correlated (Sethi et al., 2017; Stafford et al., 2014). In this work, we have carried out comparisons between the cortical rat connectome (Bota et al., 2015) and the corresponding functional network obtained from rs-fMRI data. The main findings of this study reveal that:

1. In agreement with previous studies in humans and various animal models, the level of functional interaction between two anatomically connected brain areas in resting-state is significantly predicted by the strength of the underlying structural connection.

2. BOLD signal fluctuations in the rat brain cortex can be robustly partitioned into functional modules or clusters.

3. Reciprocity of links connecting nodes from the same functionally defined modules is stronger than those linking regions from different modules.

(a)   (b)
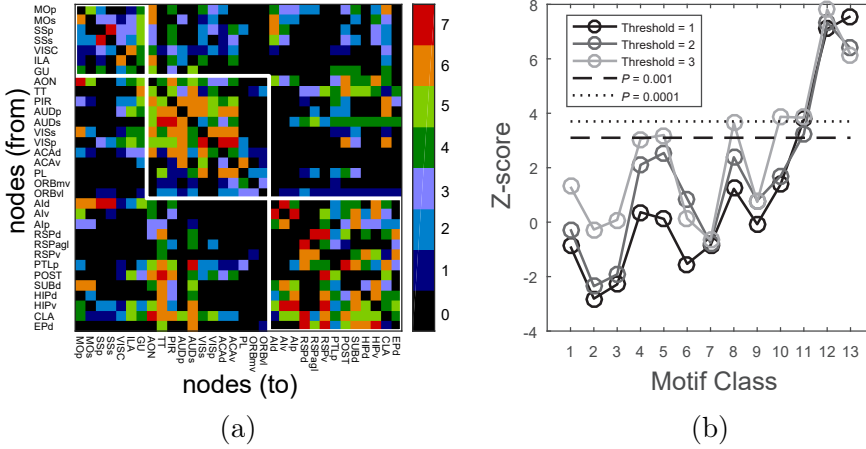
Figure 3.10. Network motif analysis at $\gamma = 0.005$. (a) Functionally obtained partition is imposed over the RCAMs matrix. (b) Statistical evaluation of each of the 13 structural motifs classes is shown for different binarized versions of the structural matrix, namely, when keeping all connections (Threshold = 1), removing *very weak* links (Threshold = 2), and removing both *very weak* and *weak/moderate* links (Threshold = 3).

4. Under a control condition and in resting-state, densely interconnected structural motifs (*i.e.*, class 12 and 13 for motif size of $M = 3$) are significantly enriched within functional communities.

3.4.1 Role of higher-order patterns in shaping cortical functional modular organization

Comparing structural connectivity and functional connectivity without taking into account network-level effects only supplies a partial view of the inherent complexity of the brain. Therefore, network approaches are increasingly gaining prominence to understand the structural-functional connectivity coupling (Wang et al., 2015). We have first shown that the 32 cortical brain regions considered in this work disclose a distinct community structure, partitioned into two, three and five communities, at $\gamma = -0.0125$, $\gamma = 0.005$ and $\gamma = 0.02$, respectively. Previous studies have investigated the modular structure of functional connections over the whole rat brain under different states of consciousness (D'Souza et al., 2014; Liang et al., 2012). Other authors have focused on specific resting-state networks (*e.g.*, the default mode network
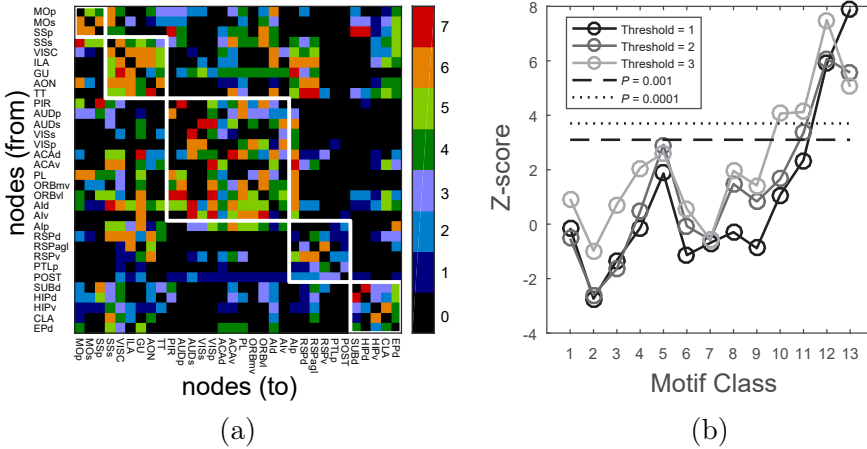
Figure 3.11. Network motif analysis at $\gamma = 0.02$. (a) Functionally obtained partition is imposed over the RCAMs matrix. (b) Statistical evaluation of each of the 13 structural motifs classes is shown for different binarized versions of the structural matrix, namely, when keeping all connections (Threshold = 1), removing *very weak* links (Threshold = 2), and removing both *very weak* and *weak/moderate* links (Threshold = 3).

(DMN)), revealing functional subcomponents and how interactions between and within these submodules can be modulated in age-related neurocognitive disorders (Hsu et al., 2016). Here, we have restricted our analysis to the brain cortex. Future work may address additional brain regions, for example including the association connectome of the rat cerebral nuclei (Swanson et al., 2016).

After evaluating the modular organization of the cortex, we first observed a stronger weighted link reciprocity within functionally defined modules compared to inter-modular links. We then observed a high ratio of structural motif classes 12 and 13 within functional modules. These findings are consistent across resolution scales. In particular, whereas motif class 12 is over-represented at scale $\gamma = -0.0125$ after removing *very weak* links and both *very weak* and *weak/moderate* links, motif class 12 at scales $\gamma = 0.005$ and $\gamma = 0.02$, and motif class 13 at all resolution scales were strongly significant for all thresholds applied. This indicates that the coherence of functional communities may in part reflect an underlying aggregation of densely connected structural motifs. Note that motif analysis was carried out on three binarized versions of rat connectome since we were interested in the count of motif classes

rather than in the strength of the connections. Additionally, the abundance of these anatomical subgraphs can not be trivially explained by lower-order features because the generated network null models also preserved the number of mutual edges of individual nodes (Milo et al., 2002). The important role of motifs in shaping the structural-functional connectivity coupling has been previously observed in the macaque cortex (Adachi et al., 2012). Nevertheless, whereas these authors computed motifs over the whole network, motif analysis in our work was restricted to within modules and to small motifs of size 3. For graphs with a greater size, a richer repertoire of larger structural motifs could be investigated (*e.g.*, network motifs of size 4 and higher (Sporns and Kötter, 2004)). There has been an increasing interest in detecting coherent groups of nodes forming specific network motifs (Arenas et al., 2008; Benson et al., 2016). In this framework, one can specify in advance a particular motif class of interest to guide the clustering process. When domain-specific knowledge is not available, it is also possible to analyze which type of motif organizes and shapes the modular structure of complex networks.

The term "motif" is widely applied for describing and understanding recurring circuits of interactions that take place in real-world networks (Alon, 2007). For instance, in the context of large-scale brain networks, as in the present report, structural motifs consist of a set of nodes and potential pathways supporting communication, whereas functional motifs refer to specific combinations of connections that can be activated within structural motifs (Sporns and Kötter, 2004). That is, both structural and functional motifs are defined for directed structural networks (Table 3.2). In other settings, for example when approaching the functioning of the brain from a computational perspective (Turkheimer et al., 2015) or in the context of activation spreads recorded with different modalities (Frostig et al., 2008; Mohajerani et al., 2013), the concept of motif is related but not completely the same as that employed in this work. The common message behind this general concept is that the brain is a highly hierarchical and complex system wherein organizational principles are repeated across space and time (Turkheimer et al., 2015).

3.4.2   *Construction of brain graphs*

A very critical step for the construction and analysis of brain network is that of dividing the brain into discrete regions. The absence of a well-established and accessible Swanson atlas in *NIfTI* format for parcellation of fMRI data required us to perform a manual matching procedure between cortical regions of SwS (Swanson, 2004) and PWS (Paxinos and Watson, 1998). This entails several caveats. First, although Swanson regions can also be expressed in stereotaxic

coordinates to correspond to Paxinos&Watson regions, coronal planes from both spaces do not always exactly match with respect to bregma reference. Therefore, taking into account the spatial distribution of adjacent planes is fundamental to achieve an accurate alignment of brain regions between different spaces. Second, a common problem when using different spaces or atlases (not only restricted to SwS and PWS) concerns the nomenclature of brain regions, as different spaces may use different nomenclature to label the same brain regions. In this case, we have used the Swanson nomenclature after carefully inspecting both SwS and PWS (see subsection 3.2.3 and Table 3.1). Finally, some cortical regions were not available in the *NIfTI* atlas as a single mask (*e.g.*, CA1 and CA2). To overcome these limitations, several areas from the anatomical matrix were aggregated together by averaging the original categorical weight. In addition, some cortical regions were discarded to ensure a representative time course in each node from functional networks. All 32 ROI signals included in our analysis were averaged across hemispheres, had exactly the same volume ($1\,\mathrm{mm}^3$ in total, $0.5\,\mathrm{mm}^3$ in each hemisphere), and were extracted from exactly the same voxels across rats. The consequences of these methodological steps might inevitable mask relevant features of individual nodes. For instance, parahippocampal regions, such as perirhinal and entorhinal cortices, were not included in our analysis and, however, these areas have shown to be critical for cortico-hippocampal integration in mice (Bergmann et al., 2016). Despite these considerations, the main research goal of the present report was to assess the empirical structural-functional connectivity coupling in the rat brain cortex with a special emphasis in comparisons at regional scale (functional modularity and structural network motifs), rather than the analysis at more local scale (Ferezou et al., 2007; Kaiser, 2011).

3.4.3   *Relevance of data preprocessing: global signal regression*

An important issue in fMRI investigations is that of controlling for head motion and physiological artifacts (mainly those related with respiratory and cardiac cycles) when estimating functional interactions between brain areas, especially in task-free paradigms (Van Dijk et al., 2012; Yan et al., 2013). Even though anesthesia can reduce rough head movements, removing the variance explained by motion parameters can substantially improve the specificity of functional connectivity in anesthetized rodents (Kalthoff et al., 2011). Numerous techniques have arisen with the aim of correcting or minimizing variations in BOLD signals as a consequence of these artifacts, namely:

- Scrubbing (Power et al., 2012).

- Spike regression (Satterthwaite et al., 2013).

- Motion parameter regression (Friston et al., 1996).

- Independent component analysis (ICA) (Pruim et al., 2015).

- The application of the aforementioned techniques along with global signal regression (Ciric et al., 2017).

The inclusion of the global signal as a nuisance regressor is a widely used but controversial preprocessing step. How negative correlations should be interpreted after global signal regression is very challenging given the nature of the BOLD signals (Fox et al., 2009; Murphy et al., 2009). In our dataset, Spearman correlation coefficient demonstrated a strong linear dependence between structural connectivity and empirical functional connectivity after controlling for the global signal. Whether or not other preprocessing steps would further increase the coupling between BOLD signals and the underlying structural connectivity is an open question that would require a separate study comparing the effects of different preprocessing pipelines (Ciric et al., 2017). The removal of global signal variance has been also applied in a previous study relating structure and function in the mouse brain (Stafford et al., 2014). It is important to acknowledge that the application of global signal regression has shown to be effective to reduce the relationship between connectivity and motion, but accentuates distance-dependent effects. On the other hand, temporal censoring techniques (*e.g.*, scrubbing and spike regression) do appear to be suitable to reduce distance-dependent effects, but using additional degrees of freedom in turn (Ciric et al., 2017). In this work, we preprocessed rs-fMRI data by combining these techniques and ensuring a minimum temporal window of 9 min to estimate functional interactions between node pairs.

3.4.4 Effect of anesthesia on functional connectivity

Another very important consideration when examining fMRI data in rodents, and other animal models, has to do with the effect of the anesthetic agent on brain physiology (Pan et al., 2015). Due to the multi-compartmental origin of fMRI signals (Moreno et al., 2013), interference of anesthetics on the neural computations, as well as on the neurovascular coupling itself are expected. Advantages and disadvantages of a number of anesthetic compounds, as well as mixtures of them, have been reported in the literature (Paasonen et al., 2016; Williams et al., 2010). It is well-established that the degree of functional inter-hemispheric coupling is dose-dependent, and previous studies have uncovered bilateral functional networks in the rodent brain using a

variety of anesthetic agents at lower doses (Gozzi and Schwarz, 2016). For instance, whereas the use of urethane anesthesia at higher levels (1.5 g/Kg) has compromised functional inter-hemispheric coupling in mice, cortico-cortical correlations improves when lower doses (1.2 g/Kg) are used (Grandjean et al., 2014). In this work, where subjects were urethane-anesthetized at 1.2 g/Kg, BOLD signals from homotopic ROIs were averaged across hemispheres because bilateral networks were uncovered using different seeds (Figure 3.2). We note, though, that for group studies where subtle inter-hemispheric differences could be of relevance, extraction of ROIs should be performed separately. Finally, it is important to highlight that the significant match found in our study between structural connectivity and functional connectivity could be favored by a decrease in the repertoire of functional configurations that the system can visit under anesthesia, as previously reported in monkeys (Barttfeld et al., 2015). Therefore, the remaining functional interactions under anesthesia would most likely reflect the strongest, hard-wired, connections in the brain, this is, the structural connectivity.

3.5 Conclusions

We have proved in this work the structure-function relationship at large-scale of the rat by directly comparing the structural and functional connections spanning the brain cortex (maximum Spearman rank-order correlation between was type of networks was 0.48), and relating second-order properties (reciprocity) and higher-order structural connectivity pattern (network motifs) with functional communities. We highlight here the importance of densely connected structural motifs in shaping the community structure of functional networks in resting-state. In this way, this investigation further supports the idea that structural connectivity is coupled to and shapes functional connectivity in cortical networks.

Chapter 4

Structural brain network deterioration associated with Alzheimer's disease

The pathophysiological process of Alzheimer's disease is thought to begin years before clinical decline, with evidence suggesting pathogenic seeding and subsequent prion-like spreading processes of neurofibrillary tangles and amyloid plaques. In this chapter, we first investigate network measures that are capable of distinguishing Alzheimer's disease patients with mild dementia from healthy controls. In the second part, we create dynamic models of normal aging and Alzheimer's disease to estimate the earliest detectable stage associated with dementia in the simulated disease progression.

The content presented in this chapter has been adapted from the following article submitted on May 10, 2018:

Díaz-Parra, A., Kennion, O., Moratal, D., Taylor, J.-P., Kaiser, M., Bauer, R., and Alzheimer's Disease Neuroimaging Initiative (2018). "Structural connectivity centrality changes mark the path towards Alzheimer's disease". *Alzheimer's & Dementia: Diagnosis, Assessment & Disease Monitoring* (Submitted).

4.1   Introduction

Alzheimer's disease is the most common cause of neurodegeneration in old age (Alzheimer's Association, 2017). Out of the main risk factors for developing Alzheimer's disease, age is the most influential by far. As a result of the change in age demographic, the number of patients will considerably increase within the coming years (Hebert et al., 2013). Alzheimer's disease is characterized by a continuous degradation involving a preclinical stage, followed by a phase of MCI, and ending with dementia in the strict sense (Alzheimer's Association, 2017; Sperling et al., 2011). Experimental evidence indicates that pathophysiological alterations take place in the brain more than a decade before clinical decline (Jack et al., 2013; Villemagne et al., 2013). Therefore, the search for biomarkers for early diagnosis and the development of disease modifying treatments is an ongoing and challenging endeavor (Jack and Holtzman, 2013).

The presence of neurofibrillary tangles and amyloid plaques are the main pathological hallmarks of Alzheimer's disease (Brettschneider et al., 2015; Jack et al., 2013; Jucker and Walker, 2011; Perl, 2010). The former are intracellular structures largely composed of tau proteins and the latter are extracellular proteolytic fragments of amyloid-β peptides. One emerging hypothesis about the progression of Alzheimer's disease posits that such substances originate in a particular area and propagate throughout neural fibers in a prion-like manner, distorting same-type proteins along the way (Frost and Diamond, 2009; Jucker and Walker, 2013; Saxena and Caroni, 2011; Warren et al., 2013). This mechanism can target neural systems organized in large-scale networks, giving rise to macroscopic changes such as atrophy and synaptic failures (Bruen et al., 2008; Delbeuck et al., 2003; Palop et al., 2006), which can be measured using MRI technology (Mak et al., 2017; Pini et al., 2016).

Network neuroscience has proven useful for understanding the impact of psychiatric and neurological disorders on brain-wide networks (Aerts et al., 2016; de Haan, 2017; Fornito et al., 2015; Zhou et al., 2012). There is a considerable literature describing the topology of Alzheimer's disease networks using different acquisition techniques (John et al., 2017; Lo et al., 2010; Xie and He, 2012). In particular, it has been shown that Alzheimer's disease strongly disturbs connections between nodes (Brier et al., 2014; Delbeuck et al., 2003), as well as those nodes occupying a central role in the network (hub nodes) (Stam, 2014; Tijms et al., 2013). Previous investigations have approached Alzheimer's disease progression by leveraging computer models simulating the spreading dynamics of a disease factor or agent across structural

connections measured with dMRI (Iturria-Medina et al., 2014; Raj et al., 2012, 2015). Furthermore, machine learning algorithms have gained prominence in neuroimaging because of their ability to decode brain signatures and predict clinical outcomes (Jie et al., 2016; Taylor et al., 2018; Woo et al., 2017). In Alzheimer's disease, different types of features can be extracted: atrophy-related measures (Desikan et al., 2009; Klöppel et al., 2008; Magnin et al., 2009); features extracted from amyloid imaging (Mathotaarachchi et al., 2017); predictors based on functional (Chen et al., 2011) and structural brain networks (Ebadi et al., 2017; Shao et al., 2012; Zhan et al., 2015); as well as multimodal descriptors describing both imaging and clinical data (Moradi et al., 2015; Young et al., 2013).

In this work, we investigate whether structural brain networks as measured with dMRI could serve as a complementary diagnostic tool in prodromal dementia. By using the Alzheimer's Disease Neuroimaging Initiative (ADNI) database, we first aim to implement machine learning techniques to extract features that are altered in Alzheimer's dementia. We then incorporate data from the Nathan Kline Institute-Rockland Sample (NKI) database and create dynamical models of normal aging and Alzheimer's disease to estimate the earliest detectable stage associated with dementia in the simulated diseae progression.

4.2   Materials and methods

Figure 4.1 presents a general overview of the proposed approach, which is described in depth in the following sections.

4.2.1   Participants and MRI acquisition protocol

We made use of two publicly available datasets widely used in neuroimaging research: the ADNI (`http://adni.loni.usc.edu/`) (Petersen et al., 2010) and NKI (`http://fcon_1000.projects.nitrc.org/indi/pro/nki.html`) (Nooner et al., 2012) databases. The primary goal of ADNI has been to test whether serial MRI, PET, other biological markers, and clinical and neuropsychological assessment can be combined to measure the progression of MCI and early Alzheimer's disease. The primary goal of the NKI has been to generate a large scale, extensively phenotyped dataset for the purpose of discovery science.
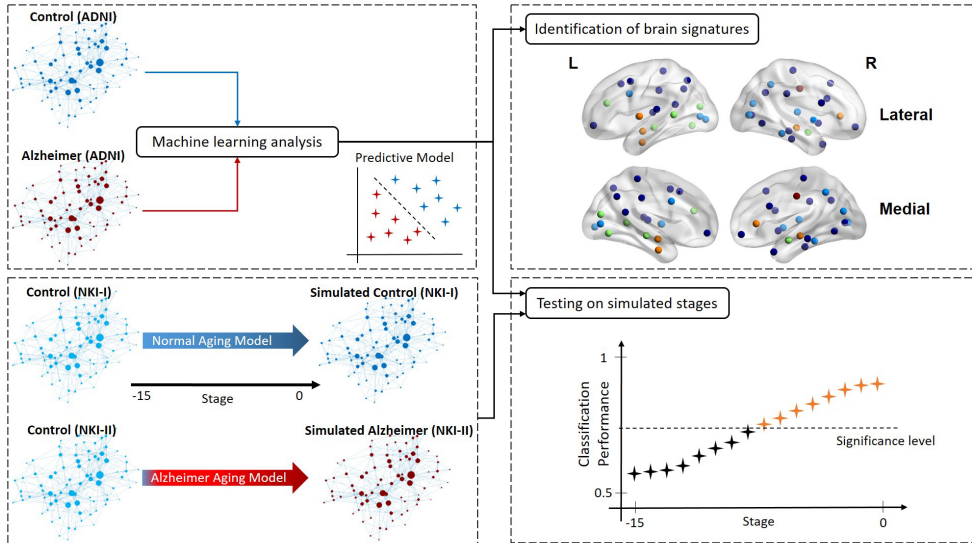
Figure 4.1. Basic schematic of the proposed approach. In the first part of the work, we generated a predictive model based on measures of complex networks to classify between a cohort of patients with Alzheimer's dementia and a cohort of matched healthy controls (top left panel). We then extracted informed brain signatures enabling diagnosis (top right panel). In the second part, we applied dynamical models to emulate changes in structural connectivity caused by normal aging on the one hand, and degradation of structural connections caused by Alzheimer's disease on the other hand (bottom left panel). We finally explored when the relevant features and brain signatures associated with dementia begin to be evident in the simulated progression process (bottom right panel). Significance level represents the minimum value from which classification performance is statistically significant. See section 4.2 for a deeper explanation about the proposed approach.

In our study, we used 39 normal controls and 39 age- and sex-matched Alzheimer's disease patients with mild dementia - meeting National Institute of Neurological and Communicative Diseases and Stroke (NINCDS)/Alzheimer's Disease and Related Disorders Association (ADRDA) criteria for probable Alzheimer's disease - from ADNI2 (`http://adni.loni.usc.edu/wp-content/uploads/2008/07/adni2-procedures-manual.pdf`). These cohorts were used to generate a classifier predicting dementia caused by Alzheimer's disease (Figure 4.1 top left panel) and identify discriminative centrality metrics and brain regions allowing for such diagnosis (Figure 4.1 top right panel). Afterwards, we included 52 adults (26 male/26 female) ranging from 45 to 81 years (60.5 ± 10.41, mean $\pm$ SD) from the NKI dataset. These individuals

are healthy with no presumed covert neuropathology. We divided the NKI dataset into two different groups: NKI-I and NKI-II. We then simulated an experiment over 15 years whereby one group experienced normal aging (NKI-I group), whereas another group of age- and sex-matched individuals developed Alzheimer's disease over the same period (NKI-II group) (Figure 4.1 bottom left panel). This second analysis allowed us to investigate how early structural network alterations associated with dementia take place in the simulated progression process (Figure 4.1 bottom right panel). Table 4.1 summarizes subject characteristics of the four groups considered in this work. For the ADNI dataset, the education variable was marginally different between controls and patients ($P = 0.047$). There was a strong difference between controls and patients in the mini mental state examination (MMSE) score ($P = 4.042 \times 10^{-13}$).

Table 4.1. Subjects information across groups.

	ADNI			NKI		
	Control (n = 39)	**Alzheimer (n = 39)**	***P*-value**	**NKI-I (n = 26)**	**NKI-II (n = 26)**	***P*-value**
Age[a]	74.19 ± 6.29	74.45 ± 8.57	0.88	60.54 ± 11.01	60.46 ± 9.98	0.979
Sex[b]	20M / 19F	20M / 19F	1	13M / 13F	13M / 13F	1
Education[a]	16.38 ± 2.75	15.10 ± 2.86	0.047	-	-	-
MMSE[a]	28.67 ± 1.42	22.10 ± 4.47	4.042×10^{-13}	-	-	-

Education and MMSE variables were not available for the NKI dataset.
[a] Values represent mean $\pm$ SD. Group differences evaluated using a two-sample t-test (two-tailed).
[b] Group difference evaluated using a χ^2-test (two-tailed).

All subjects underwent T1-weighted sMRI and dMRI scanning. For the ADNI dataset, MRI data were acquired on 3 Tesla GE Medical Systems scanners (Boston, Massachusetts, USA) at different acquisition sites across North America. Diffusion-weighted images were recorded applying the following parameters: matrix size = 256 $\times$ 256; voxel size = 2.7 $\times$ 2.7 $\times$ 2.7 mm^3; 59 slices; 5 images with no diffusion sensitization and 41 diffusion directions with b-factor of 1000 s mm^{-2}. More imaging details can be found at `http://adni.loni.usc.edu/wp-content/uploads/2010/05/ADNI2_GE_3T_22.0_T2.pdf`. For the NKI dataset, MRI data were measured with a 3 Tesla Siemens MAGNETOM TrioTim syngo scanner (Erlangen, Germany). In this case, dMRI data were recorded applying the following parameters: matrix size = 128 $\times$ 128; voxel size = 2 $\times$ 2 $\times$ 2 mm^3; 58 slices; 12 images with no diffusion sensitization and 64 diffusion directions

with *b*-factor of $1000\,\text{s}\,\text{mm}^{-2}$. More imaging details can be found at `http://fcon_1000.projects.nitrc.org/indi/pro/nki.html`.

4.2.2   Preprocessing of MRI data and construction of structural brain networks

Data preprocessing was carried out using a combination of software libraries. The preprocessing pipeline to extract brain graphs from the NKI dataset has been described elsewhere (Lim et al., 2015). For the ADNI dataset, a similar pipeline was applied to maintain consistency across datasets. First, structural images were preprocessed using *FreeSurfer v5.3* (`http://surfer.nmr.mgh.harvard.edu/`) as described by Wang et al. (2016). The preprocessing stream of *FreeSurfer* fundamentally performs skull stripping, intensity normalization, subcortical region segmentation, grey and white matter segmentation, and cortical surface extraction for subsequent labeling. The resulting subdivision of the cerebral cortex based on the Desikan/Killinay atlas (Desikan et al., 2006) was combined with subcortical structures to generate a brain parcellation containing 34 cortical and 7 subcortical regions (thalamus, caudate, putamen, pallidum, amygdala, hippocampus[1] and accumbens) for each hemisphere (see Table 4.2 for a detailed listing of the included regions). The same parcellation have been previously used in the context of Alzheimer's disease (Desikan et al., 2009; Prescott et al., 2014).

Raw diffusion data were downloaded from ADNI in *DICOM* data format. Images were then converted to *NIfTI* data format using the *dcm2niix* tool available in *MRIcroGL* (`https://www.nitrc.org/projects/dcm2nii/`) and subsequently preprocessed with *FSL v5.0* (FMRIB Software Library, `https://fsl.fmrib.ox.ac.uk/fsl/fslwiki/`) (Jenkinson et al., 2012). *Dcm2niix* automatically provides a table that stores the diffusion gradient vector for each acquired volume. Using the first *b*0 image as reference, diffusion images were corrected for eddy current and head motion distortions by using the *eddy_correct* tool (Andersson and Sotiropoulos, 2016). Gradient vectors were rotated accordingly by means of the *fdt_rotate_bvecs* function. Next, brain extraction was performed with *BET* (Smith, 2002) before reconstructing diffusion tensors at each voxel through the *Diffusion Toolkit* suite (`http://trackvis.org/dtk/`). Deterministic fiber tracking was carried out by applying the *FACT* method (Mori et al., 1999). Single seed points to reconstruct streamlines were placed in the center of each voxel belonging to the brain and tracking was terminated for curvatures greater than $35°$.

---

[1]Following *FreeSurfer*'s nomenclature, we consider the hippocampus as being a subcortical region.

Table 4.2. Brain regions along with their respective abbreviations.

Brain structure	Abbreviation
Banks of the superior temporal sulcus	BSTS
Caudal anterior division of the cingulate cortex	CAC
Caudal division of the middle frontal gyrus	CMF
Cuneus cortex	CUN
Entorhinal cortex	ENT
Fusiform gyrus	FUS
Inferior parietal cortex	IP
Inferior temporal gyrus	IT
Isthmus division of the cingulate cortex	ISTC
Lateral occipital cortex	LOCC
Lateral division of the orbitofrontal cortex	LOF
Lingual gyrus	LING
Medial division of the orbitofrontal cortex	MOF
Middle temporal gyrus	MT
Parahippocampal gyrus	PARH
Paracentral lobule	PARC
Pars opercularis of the inferior frontal gyrus	POPE
Pars orbitalis of the inferior frontal gyrus	PORB
Pars triangularis of the inferior frontal gyrus	PTRI
Pericalcarine cortex	PCAL
Postcentral gyrus	PSTC
Posterior division of the cingulate cortex	PC
Precentral gyrus	PREC
Precuneus cortex	PCUN
Rostral anterior division of the cingulate cortex	RAC
Rostral division of the middle frontal gyrus	RMF
Superior frontal gyrus	SF
Superior parietal cortex	SP
Superior temporal gyrus	ST
Supramarginal gyrus	SMAR
Frontal pole	FP
Temporal pole	TP
Transverse temporal cortex	TT
Insula	INS
Thalamus	THAL
Caudate	CAUD
Putamen	PU
Pallidum	PAL
Amygdala	AMYG
Hippocampus	HIPP
Accumbens	ACC

For network generation, streamlines were first aligned with the brain parcellation. The first skull-stripped $b0$ image was linearly registered to the preprocessed structural image using *FSL flirt* with six degrees of freedom (Jenkinson et al., 2002). Next, the resulting transformation matrix was applied to every streamline by means of the *track_transform* function included in *Diffusion Toolkit* software. The *UCLA Multimodal Connectivity Package* (`https://github.com/jbrown81/umcp`) was used to obtain an 82×82 weighted connectivity matrix for each subject. Structural interactions were quantified by counting the number of streamlines connecting two regions (self-connections were not considered). Finally, only streamlines with either endpoints terminating at the two regions and greater than $5\,\mathrm{mm}$ were included.

4.2.3 Mathematical models

Alzheimer aging model

Spreading processes have been studied in a multitude of scientific disciplines (Pei and Makse, 2013). We implemented the susceptible-infected (SI) model (Newman, 2010; Pastor-Satorras et al., 2015) to simulate the propagation of a disease factor as Alzheimer's disease progresses. In this model, nodes can be in two possible states: infected or susceptible. Infected nodes are brain regions wherein the probability of the disease factor burden is greater than zero. By contrast, susceptible nodes are free of the disease factor but are susceptible to be infected from other nodes. In a network with N nodes, for any particular node i, the probability of being susceptible, s_i, and the probability of being infected, x_i, satisfy such that $s_i + x_i = 1$. Thus, it is possible to express the rate of change of x_i in the SI model as (Newman, 2010):

$$\frac{\mathrm{d}x_i}{\mathrm{d}t} = \alpha(1 - x_i) \sum_{\substack{j=1 \\ j \neq i}}^{N} a_{ij} x_j, \qquad (4.1)$$

where a_{ij} is an element of the (binary) adjacency matrix, whereas the parameter alpha, $\alpha > 0$, controls the infection rate of node j over node i. As we made use of weighted networks, we replaced the Equation (4.1) by:

$$\frac{\mathrm{d}x_i}{\mathrm{d}t} = \alpha(1 - x_i) \sum_{\substack{j=1 \\ j \neq i}}^{N} \frac{w_{ij}}{k_j} x_j. \qquad (4.2)$$

In the Equation (4.2), k_j stands for the strength of node j and the influence of node j over node i is now proportional to the weight, w_{ij}. We further incorporated another equation simulating Alzheimer's disease-related degradation in connectivity. Particularly, the rate of change of w_{ij} is given by:

$$\frac{\mathrm{d}w_{ij}}{\mathrm{d}t} = -\beta^{AD} w_{ij}(x_i + x_j) + \beta_{ij}^N, \tag{4.3}$$

where the parameter beta, $\beta^{AD} > 0$, controls the influence of the aggregated disease factor present in both node i and node j on the number of streamlines connecting them. The term β_{ij}^N represents the normal aging process (see below) to reflect the fact that patients also age. Therefore, the Alzheimer aging model (Equations (4.2) and (4.3)) relies on three unknown parameters: α, β^{AD}, and an additional parameter indicating the seed region origin of the disease factor. By varying these parameters, one can simulate different diseased trajectories followed by NKI-II participants.

Normal aging model

We developed a mathematical model reflecting the process through which structural connections change due to normal aging. Connectome organization develops across the life span, with age and sex being two critical factors during this process (Collin and van den Heuvel, 2013; Lim et al., 2015). We created link-specific regression models to predict the number of streamlines from age- and gender-related effects. Inspired by Lim et al. (2015), the number of streamlines between region i and region j, w_{ij}, can be expressed as a combination of $p = 4$ variables or predictors (*age*, *gender*, *age gender*, *age*^{2}):

$$w_{ij} = \beta_0^{ij} + \beta_1^{ij}\, age + \beta_2^{ij}\, gender + \beta_3^{ij}\, age\, gender + \beta_4^{ij}\, age^2, \tag{4.4}$$

where *gender* $= 1$ for males and *gender* $= -1$ for females. In the Equation (4.4), we included an intercept term (β_0^{ij}), the linear effect of both age (β_1^{ij}) and gender (β_2^{ij}), the interaction between age and gender (β_3^{ij}), as well as the quadratic effect of age (β_4^{ij}). The coefficients from the Equation (4.4) were only estimated for those connections that all NKI participants had in common (126 connections), generating a minimum grid mask (Fischi-Gómez et al., 2015). Thus, we had 52 data points over the age range of $[45, 81]$ years for each of the 126 common connections.

Upon deriving the Equation (4.4) with respect the age effect, we obtained the following differential equation attempting to mimic the process for aging:

$$\frac{\mathrm{d}w_{ij}}{\mathrm{d}t} = \beta_{ij}^{N} = \beta_1^{ij} + \beta_3^{ij}\, gender + 2\,\beta_4^{ij}\, age. \qquad (4.5)$$

It has been shown that brain connectivity evolves in such a manner that core properties of structural networks (*e.g.*, modular organization) remain stable during brain maturation and adulthood (Collin and van den Heuvel, 2013; Lim et al., 2015; Zhao et al., 2015), suggesting that rules governing neural fiber changes over time are connection-dependent. In mathematical terms, it means that some predictors from the Equation (4.4) can be irrelevant to predict the number of streamlines connecting region i and region j. We therefore applied the model selection algorithm named *subset selection* (James et al., 2013) to exclude variables not related to the response w_{ij}. This approach involves fitting a separate least squares regression for each possible combination of the p predictors and selecting the model that is the "best" in terms of accuracy and complexity. As $p = 4$, a total of 16 different models were fitted containing all possible combinations. Next, among those models containing the same number of variables, the one giving the greater coefficient of determination, R^2, was chosen. This step retained five different models, which contained zero (*i.e.*, a model predicting merely the sample mean through β_0^{ij}), one, two, three and four predictors. Finally, the models were compared by using the Akaike information criterion (AIC), and the model providing the smallest AIC was selected to predict w_{ij}. The outcome of this procedure was a set of link-specific regression models (Equation (4.4)) and their corresponding differential equations (Equation (4.5)), varying in complexity according to the number of included predictors. Note that we did not compute any P-value in this analysis, since our objective was to maximize the ability of the model to predict the response rather than explain the association between variables and the response.

Dynamical simulations

We applied the aforementioned normal aging model to the NKI-I group to create a cohort of simulated healthy controls evolving over 15 years. Similarly, we applied the Alzheimer aging model to the NKI-II group to reproduce the process of propagation of misfolded proteins and disruption of neural pathways throughout the same time window, creating a cohort of simulated Alzheimer's disease patients. To simulate diseased trajectories, we pre-specified different

alpha values ranging from 0 to 1.5 in increments of 0.05 and beta values ranging from 0 to 0.15 in increments of 0.005. These ranges were chosen upon empirically testing possible parameter values to reproduce the differences in structural connectivity between ADNI controls and ADNI patients. For each combination of alpha and beta values, a different brain region in both hemispheres (41 seed regions) was deemed as origin to initiate the progression. By using matrices as input data and for each parameter combination within the set $\{seed, \alpha, \beta^{AD}\}$, we numerically computed model solutions of the Equations (4.2), (4.3) and (4.5) in MATLAB *2016a* (The MathWorks, Inc., Natick, MA, United States, `https://www.mathworks.com/`), with a step size of 0.1. This process produced a set of simulated structural networks based on the changes in connection strength either caused by the process of normal aging or by Alzheimer's disease (Figure 4.1 bottom left panel).

We recorded the resulting simulated matrices in discrete points of a year and defined a set of 16 simulated stages for further analysis (Figure 4.1 bottom right panel). From this point on, we will be using the term "stage" rather than "years" to account for the fact that patients can develop Alzheimer's disease at different rates. Thus, stage -15 represents the initial stage in which both groups of individuals (*i.e.*, NKI-I and NKI-II) are in a healthy condition. By contrast, stage 0 represents the disease stage in which neural degeneration compromises cognitive functions enough to meet criteria for dementia. To assess the extent to which stage 0 reflects this criterion, we compared the differences in node strength obtained at stage 0 between simulated controls and simulated patients, with the counterpart differences measured between ADNI controls and ADNI patients. Specifically, we selected the parameter set $\{seed, \alpha, \beta^{AD}\}$ minimizing the cost function defined by the Euclidean distance between k^0_{NKI} and k_{ADNI}. The term k^0_{NKI} represents the size 82 vector incorporating the differences in node strength measured between simulated controls and simulated patients at stage 0, and the term k_{ADNI} stands for the size 82 vector containing the differences in node strength measured between ADNI controls and ADNI patients.

4.2.4 *Feature extraction and machine learning analysis*

Centrality is a measure that quantifies the relative importance of a node within the overall architecture of a network (van den Heuvel and Sporns, 2013). We made use of the *Brain Connectivity Toolbox v2017-15-01* (`https://sites.google.com/site/bctnet/`) (Rubinov and Sporns, 2010) and computed the following centrality measures (Boccaletti et al., 2006; Pei and Makse, 2013; Rubinov and Sporns, 2010):

Strength: the strength centrality of a node is a basic and intuitive measure that is defined as the sum of all neighboring link weights.

Betweenness and closeness: betweenness and closeness are centrality measures that assume that information tends to traverse the network through the shortest paths. First, a path from node i to node j is a sequence of nodes and edges that begins with i and ends with j, where no node is visited more than once. On the other hand, in weighted networks, higher weights are commonly interpreted as shorter lengths. Thus, the shortest path between node i and node j is the path of minimal length connecting both nodes.

The betweenness centrality of a node is the fraction of all shortest paths in the network that contain that specific node. Nodes with high values of betweenness centrality participate in a large number of shortest paths. The closeness centrality of a node is inversely proportional to the sum of its distances to all other nodes in the network. Thus, the greater closeness a node has, the lower its total distance to all other nodes is.

Eigenvector and pagerank: eigenvector and pagerank are centrality measures that accounts for the importance of neighboring nodes. This is, a node connected to central nodes turns itself to important.

The eigenvector centrality of node i is equivalent to the i_{th} element in the eigenvector corresponding to the largest eigenvalue of the connectivity matrix. Pagerank is a generalization and variation of eigenvector centrality and is defined as the stationary distribution achieved by instantiating a Markov chain on the network.

The foregoing graph metrics were extracted at node-level, producing a feature vector with 410 elements for each subject. Before computing this topological properties, the fraction of streamlines connecting each pair of regions was calculated (Batalle et al., 2017):

$$w'_{ij} = \frac{w_{ij}}{\sum_{k,l} w_{kl}}, \tag{4.6}$$

where w_{kl} represents the streamline counts connecting region k and region l.

Feature scaling is a typical data preprocessing step in machine learning (Pereira et al., 2009). Node metrics were scaled to have zero mean and unit variance.

For example, for the strength of node i, k_i, standardization was performed using the mean, $\bar{k}$, and standard deviation, σ_k, of the strength distribution:

$$k_i^z = \frac{k_i - \bar{k}}{\sigma_k}. \tag{4.7}$$

Another important issue in predictive modeling is that of feature selection (Guyon and Elisseeff, 2003; Saeys et al., 2007). Feature selection methods are widely used in machine learning community to remove irrelevant predictors, especially when dealing with high-dimensional feature vectors (Guyon and Elisseeff, 2003; Saeys et al., 2007). These techniques enable reducing model complexity and improving interpretability. We applied machine learning tools to produce relevant features and brain patterns or signatures classifying between ADNI controls and ADNI patients with dementia (Figure 4.1 upper row). To this end, we combined different methods as implemented in the *Scikit-Learn Package v0.19.0* (`http://scikit-learn.org/stable/index.html`) (Pedregosa et al., 2011).

Supervised learning

Machine learning problems can be mainly categorized as *supervised* or *unsupervised* (James et al., 2013). In supervised learning problems, each sample or instance in the dataset typically consists of input variables (also called *features* or *predictors*), which characterize the sample in question, and an output variable (also called *response*). The purpose of supervised learning is basically to "learn" a function of the features with the aim of predicting the response. By contrast, the response is not available in unsupervised learning problems, and the main task in this setting is to model the underlying structure in the dataset.

Supervised learning problems can be in turn divided into *classification* or *regression*, depending on whether the response is categorical or numeric, respectively. In classification problems, the response is also called *class*. Many of the upcoming techniques can be used in both classification and regression settings. However, we will introduce them for classification purposes, as we aim to predict the subject's condition (*i.e.*, dementia *vs.* control) from centrality features. Note that the normal aging model presented in subsection 4.2.3 was approached as a regression problem.

Feature ranking with random forest

A RF is an ensemble method that combines many *decision trees* (Breiman, 2001). A decision tree is a predictive model that uses a set of binary rules to predict the class. Figure 4.2 illustrates a basic example where the class is predicted from features A and B. Essentially, decision trees partition the feature space into smaller and pure groups by testing feature values (Müller and Guido, 2016). Thus, nodes (not to be confused with network nodes) in the tree either represent groups (represented by rectangles in Figure 4.2 right panel) or feature tests (represented by ellipses in Figure 4.2 right panel). Groups are also called *terminal* nodes or *leaves*. The impurity of a given node can be measured with the Gini index (Kuhn, 2013), which is defined as:

$$I^G = 1 - \sum_{i=1}^{C} p_i^2,\qquad(4.8)$$

where C is the number of classes and p_i the class i probability in the node. Therefore, the lower I^G is, the more pure the node is with respect to one of the classes.

Building, fitting or training a tree consists in recursively searching over combinations of binary decisions to split the feature space into relatively pure groups. During this process, it is possible to compute the reduction in impurity prior and after testing each feature across nodes. This reduction represents the relevance of a feature in predicting the class. The main drawback of decision trees is that they are not able to deal well with overfitting. To overcome this limitation, RFs combine the results of individual trees (Müller and Guido, 2016).

With the aim of ranking centrality features, we made use of the RF technique with 1000 trees. This method returned a set of scores quantifying the importance of each feature, which is obtained by averaging the feature importance of individual trees. Note that the RF algorithm was employed to generate a feature ranking and not to the classification process itself. Feature selection methods that are built-in within some predictive models, such as decision trees and RFs, are called *embedded* methods (Guyon and Elisseeff, 2003).
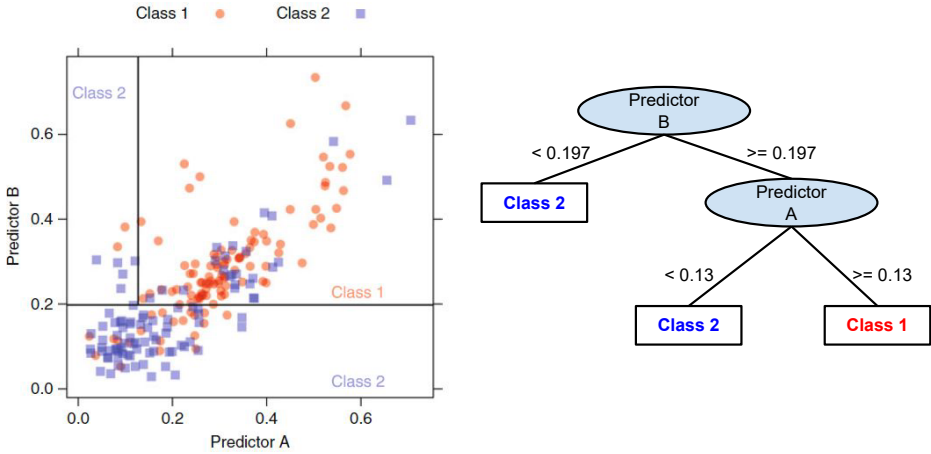
Figure 4.2. Decision tree approach. Classes 1 and 2 are predicted from features A and B (left panel) using a decision tree (right panel). Reproduced from Kuhn (2013).

Classification with support vector machines

In a two-class classification problem, a classifier can be mathematically represented as a decision function $f : \mathbb{R}^N \to \{-1, +1\}$ that assigns a particular observation $x \in \mathbb{R}^N$ (where N represents the number of features) to one of the classes, denoted by -1 and $+1$, respectively (Lemm et al., 2011). Now consider the problem illustrated in Figure 4.3 left panel, where two features are used to classify between two different types of samples (red and blue). Class samples can be linearly separable using multitude of linear decision functions. Each linear decision function corresponds to a separating hyperplane, the classification boundary, that relies on its normal vector, $\mathbf{w}$, and a bias term, b. A given hyperplane represents a line in a two-dimensional space (*i.e.*, when using two features, as in Figure 4.3 left panel), whereas represents a plane in a three-dimensional space (*i.e.*, when using three features). Either way, the class, y, can be predicted as follows (Lemm et al., 2011):

$$y = f(x; \mathbf{w}, b) = sgn(\mathbf{w}^T x + b), \qquad (4.9)$$

and thereby the hyperplane is given by:

$$\mathbf{w}^T x + b = 0. \tag{4.10}$$
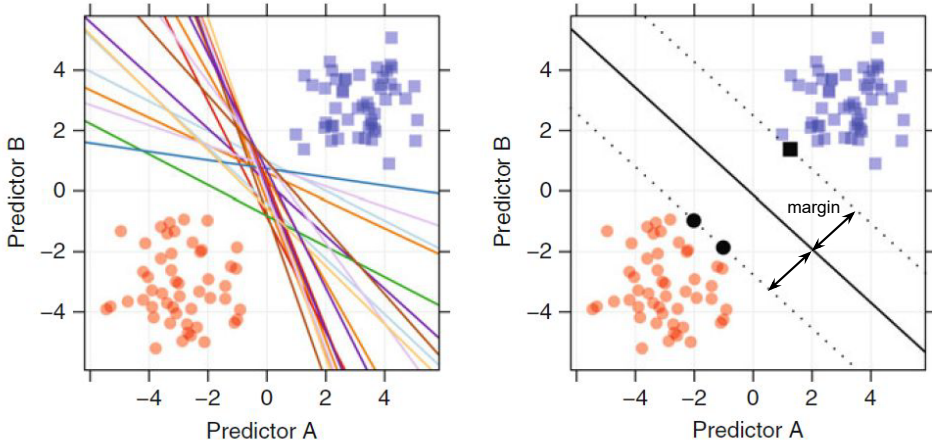
Figure 4.3. Linear support vector machine approach. Many hyperplanes (lines in a two-dimensional space) can be used to predict the class samples from features A and B (left panel). A linear support vector machine proposes a classification boundary such that the margin is maximized. Reproduced from Kuhn (2013).

Thus, the feature space is separated into two groups, given by the samples that satisfy $\mathbf{w}^T x + b > 0$ (*i.e.*, samples of the positive class, $y = +1$) and the samples that satisfy $\mathbf{w}^T x + b < 0$ (*i.e.*, samples of the negative class, $y = -1$), respectively. In this case, learning consists in selecting the optimal parameters $(\mathbf{w}, b)$ such that f will correctly predict the class. How optimal a decision function (and its corresponding classification boundary) is depends critically on the selected metric to evaluate the goodness of the classification. The SVM technique is an approach that has gained popularity in many fields. A linear SVM attempts to find the optimal decision function by maximizing the distance between the separating hyperplane and the closest sample point. This distance is called *margin* (Chang and Lin, 2011; Kuhn, 2013). In Figure 4.3 right panel, three samples are equally closest to the classification boundary. Such points are called *support vectors*. In mathematical terms, a liner SVM solves the following optimization problem (Chang and Lin, 2011; Lemm et al., 2011):

$$\min_{\mathbf{w},b,\xi} \qquad \frac{1}{2}\mathbf{w}^T\mathbf{w} + C\sum_{i=1}^{N}\xi_i$$

$$\text{subject to} \qquad y_i(\mathbf{w}^T x_i + b) \geqslant 1 - \xi_i,$$

$$\xi_i \geqslant 0, i = 1, \ldots, N. \tag{4.11}$$

In the Equation (4.11), N stands for the number of samples used to train the model. The term ξ_i represents slack variables that control whether a sample can be within the margin error ($0 \leqslant \xi_i \leqslant 1$) or be misclassified ($\xi_i \geqslant 1$), whereas $C > 0$ is the regularization parameter that controls for the constraints introduced by ξ_i.

In many real-world problems, class samples cannot be accurately separated using a linear classification boundary. Rather, more sophisticated decision functions are required to account for non-linearities. Support vector machines handle this situation by mapping the original space into a higher dimensional space via a *kernel* function, the *kernel trick*, in such a manner that the transformed input samples can be linearly separated in the new space (Kuhn, 2013; Lemm et al., 2011).

The SVM classifier has been successfully applied in the context of diverse pathologies (Fagerholm et al., 2015; Klöppel et al., 2008). We trained SVMs to distinguish ADNI patients from ADNI controls. We made use of a radial basis function kernel, which introduces an extra parameter to be optimized, $\gamma > 0$. Here, we set $\gamma = 1/N$, where N denotes the number of features. On the other hand, the parameter C of radial SVMs was selected within the set $\{1, 10, 100\}$ to maximize model performance.

Model evaluation with cross-validation

The main interest in supervised learning, and particularly in a classification setting, is to fit a classifier with the ultimate goal of predicting new samples that were not used during the training phase. To evaluate the extent to which a predictive model generalizes across samples, the available dataset can be divided into training and test samples. The training samples are observations aimed to build the model, providing the *training error*, whereas the test samples are observations aimed to test the resulting classifier, providing the *test error*. This difference is important because one can fit a very complex model to perfectly predict the class in the training dataset (resulting in a very small training error), but obtain poor results in the test dataset (resulting in

a very large test error). This problem is known as *overfitting* (James et al., 2013).

In the absence of a very large dataset, splitting the data into training and test samples is not practical, so other strategies such as *resampling* techniques are applied. One popular approach to evaluate the ability of a model in predicting the class is that known as *k-fold cross-validation*. In this technique, the original dataset is randomly partitioned into k groups (also called *folds*) of roughly equal size. The first fold is used to test the model and estimate the classification performance, whereas the remaining $k-1$ folds are used for fitting the model (James et al., 2013; Kuhn, 2013). The same procedure is repeated k times; each time, a different fold is used for testing. The performance measures generated across the k repetitions are summarized with the mean and standard deviation. Typical values for k are 5 and 10. Additionally, the whole procedure can be repeated a certain number of times, resulting in a *repeated k-fold cross-validation*.

Regarding the measures to evaluate the classification performance, consider a two-class classification setting, where a predictive model is fitted using $k-1$ folds and tested on the remaining one. The predictions provided by the classifier from the test fold can be compared with the actual class labels and generate what is called the *confusion matrix* (Figure 4.4). From this matrix, several performance measures can be calculated (Kuhn, 2013):

Sensitivity: the sensitivity is the rate that the positive class is correctly predicted for all positive samples: sensitivity = TP/(TP + FN). The sensitivity is also known as the *true positive rate*.

Specificity: the specificity is the rate that the negative class is correctly predicted for all negative samples: specificity = TN/(FP + TN). The *false positive rate* is defined as one minus the specificity.

Accuracy: the accuracy reflects the overall agreement between the actual and predicted classes by accounting for positive and negative samples: accuracy = (TP + TN)/(TP + FP + FN + TN).

Making predictions can be seen as thresholding the output of the decision function (Equation (4.9)), where a threshold of 0 is used (Müller and Guido, 2016). In some applications, the desired outcome is a continuous valued prediction, which is usually in the form of a probability (*i.e.*, between 0 and 1). In this way, one can provide more informed decisions. For example, given a feature vector x representing centrality measures, what is the probability of this subject having dementia? Note that one can still
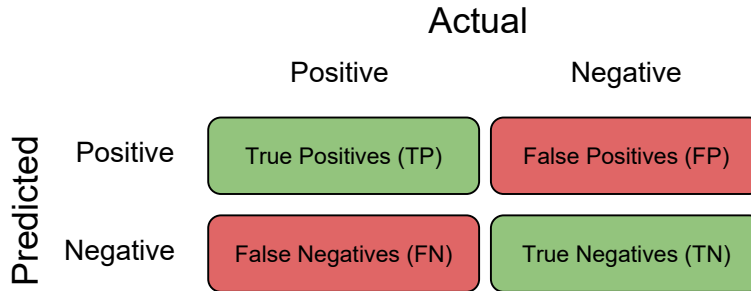
Figure 4.4. Confusion matrix. Predicted class labels are compared with actual class labels, resulting in true positives (TP), false positives (FP), false negatives (FN) and true negatives (TN) results. Positive and negative classes could refer to dementia and control conditions, respectively, depending on the criterion adopted by the researcher. Nevertheless, in a medical context, the positive class is usually used for the diseased condition.

set a specific threshold, say 0.5, to provide discrete predictions, rather than continuous predictions. Returning class probabilities further enable measuring the classification performance using a useful device called the *receiver operating characteristic (ROC) curve*. The ROC curve is constructed by evaluating the class probabilities across different thresholds. For each threshold, the sensitivity and false positive rate $(1 -$ specificity$)$ is computed (Figure 4.5). A model that perfectly separates two classes would have unit sensitivity and specificity (identified by a purple point in Figure 4.5). As noted, there is a tradeoff between the sensitivity and specificity achieved in the classification. As the threshold lowers, the true positive rate improves and the false positive rate declines. Whereas that the opposite effect occurs when the threshold highers. The area under the curve (AUC) yields another measure to evaluate the classification performance. Indeed, a perfect classifier would provide an AUC of 1, whereas that a random classifier would offer an AUC of 0.5 (represented by the dashed red line in Figure 4.5). The AUC allows evaluating the predictive model without fixing a specific threshold and thereby summarizes the overall performance in a single index. Note that a different accuracy value is also obtained for each threshold.

Some classifiers such as the SVM approach do not naturally provide probability estimates. Rather, they potentially provide predictions in the range $[-\infty, +\infty]$. These predictions are then thresholded (Equation (4.9)). In order to transform
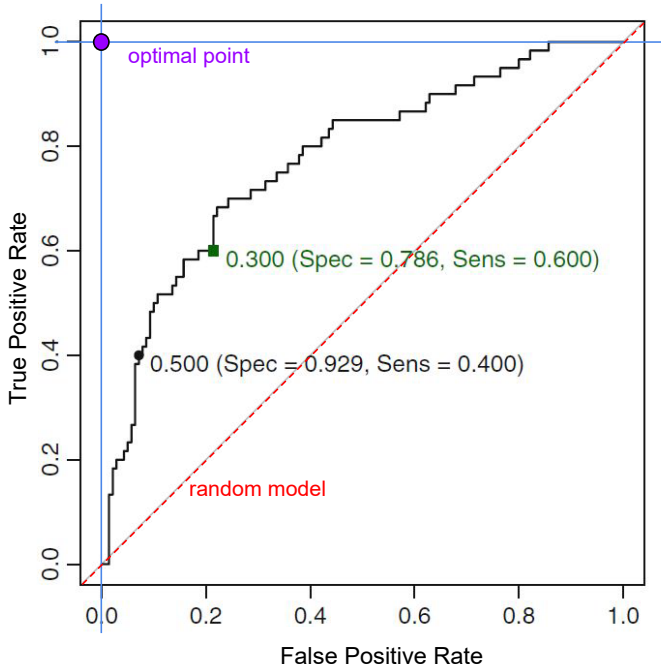
Figure 4.5. Receiver operating characteristic curve. The ROC curve reflects the sensitivity and specificity (and the accuracy accordingly) across different thresholds for classification. In this particular example, at a probability threshold of 0.5, the sensitivity and specificity is 0.4 and 0.929, respectively. At a probability threshold of 0.3, the sensitivity and specificity is 0.6 and 0.786, respectively. A perfect classifier is represented by the purple point, whereas a random classifier is represented by the dashed red line. Adapted from Kuhn (2013).

this range into class probabilities and make use of the ROC curve accordingly, one can apply the Platt scaling (Wu et al., 2004).

To estimate model performance, we incorporated RF and SVM methods in a cross-validation scheme (Figure 4.6). First, the ADNI dataset was split into training and test folds by using the 10-fold cross-validation technique, ensuring that classes were balanced within each fold. In each iteration, a RF was fitted by using the training folds, giving rise to a ranking encoding the relative importance of each feature. To identify the minimum number of features providing good predictions, radial SVMs were then trained by adding features progressively. That is, a first radial SVM was computed using the

most relevant feature (according to the foregoing ranking). Next, a second radial SVM was obtained using the two most important features, sequentially adding features until all features were considered. Each of the 410 radial SVMs was evaluated on the test fold and the AUC of the ROC curve was recorded as a function of the number of features, producing a performance profile. The whole process was further repeated 10 times. Performance profiles and feature importance scores generated across the 100 iterations of the repeated 10-fold cross-validation were averaged. To maximize model performance, we applied this cross-validation scheme for each parameter C, and selected the combination of parameter C and number of features providing the max AUC. Using such number of features, we performed a ROC analysis.

Predictions in the simulated disease progression

As we were also interested in estimating when alterations associated with dementia begin to be significantly apparent in the simulated progression process, a final SVM based on the identified features was fitted using all ADNI samples, and the resulting predictive model was independently tested on each NKI simulated stage (Figure 4.1 bottom right panel). We then computed performance measures of AUC, sensitivity, specificity and accuracy produced throughout the modeled progression span and evaluated the significance of these values. We applied the one-tailed binomial test to evaluate the significance of sensitivity, specificity and accuracy (Pereira et al., 2009) and the non-parametric Wilcoxon rank sum test to evaluate the significance of AUC values (Hanley and McNeil, 1982). We declared results as significant at $P < 0.05$. We further applied the false discovery rate (FDR)-adjustment procedure (Yekutieli and Benjamini, 1999) with $q = 0.05$ to control for multiple comparisons across stages within each performance measure. In all cases, we reported values of sensitivity, specificity and accuracy at the threshold for classification providing the best tradeoff between sensitivity and specificity.

4.3   Results

4.3.1   Diagnosis of dementia caused by Alzheimer's disease

We first analyzed the ADNI dataset with machine learning tools to explore whether structural networks inferred from dMRI predict Alzheimer's disease. Using the cross-validation approach, we achieved the best classification performance when using radial SVMs with $C = 100$ and the first 86 most
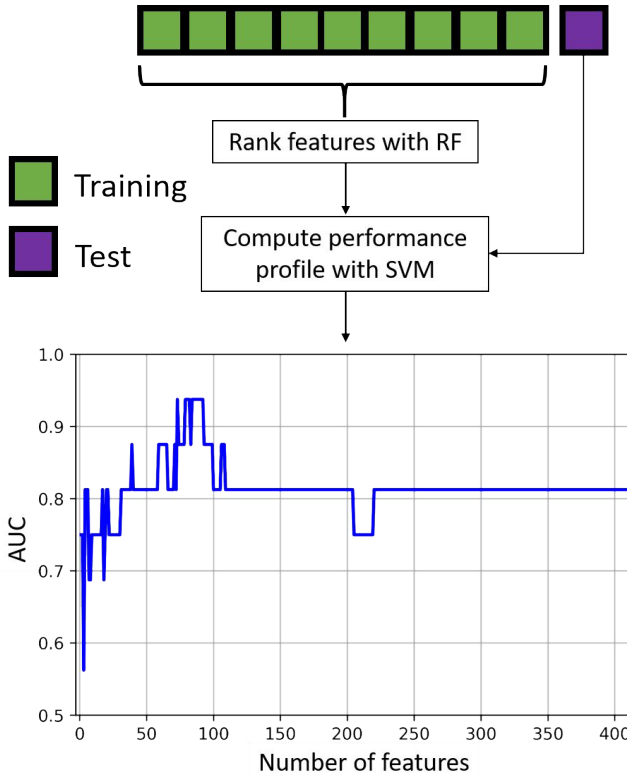
Figure 4.6. Cross-validation. Model evaluation was performed by a repeated 10-fold cross-validation scheme. After partitioning the input dataset into 10 folds, data from nine folds (in green) are used for feature ranking and model fitting. The remaining fold (in purple) is used for model testing, hence generating a performance profile: the classification performance (in term of AUC) as a function of the number of features, which are sorted according to their relative importance. The whole process was repeated 10 times, producing a total of 100 performance profiles and feature rankings, which were finally averaged.

relevant features according to the ranking generated with the RF algorithm (max AUC = 0.78 ± 0.16, mean ± SD) (Figure 4.7a), so the remaining 324 network features did not provide further information for diagnosis. We then analyzed the mean ROC curve generated with the selected features (Figure 4.7b). At the optimal threshold for classification, sensitivity was of 74.17 % ($P = 1.69 \times 10^{-3}$), specificity of 73.47 % ($P = 1.69 \times 10^{-3}$) and accuracy of 73.82 % ($P = 9.76 \times 10^{-6}$), substantially higher than the empirical distribution (50 %).

Next, we identified the most discriminative centrality measures and brain regions providing such performance. Strength and closeness centrality together account for almost half of the network features (23.25 % and 24.42 %, respectively). Measures of eigenvector and pagerank centrality have a lesser influence for classification, but still represent a considerable proportion of the retained features (19.77 % in both cases). Betweenness centrality is the least representative measure in the final set of selected features, accounting for the remaining 12.79 % (Figure 4.8a). More specifically, the top five discriminative features in diagnosing Alzheimer's dementia are pagerank centrality of the left insula, followed by closeness centrality of the left amygdala, betweenness centrality of the right hippocampus, strength centrality of the left insula, and closeness centrality of the left entorhinal cortex (see Table 4.3 for a detailed listing of the selected features).

Table 4.3. Most important features in predicting dementia. Each feature consists of a brain region (represented by its abbreviation, see Table 4.2), the hemisphere which the brain region comes from, and the specific centrality measure associated with the region (*i.e.*, strength, betweenness, closeness, eigenvector or pagerank).

Position in the ranking	Region	Hemisphere	Centrality measure
1	INS	left	pagerank
2	AMYG	left	closeness
3	HIPP	right	betweenness
4	INS	left	strength
5	ENT	left	closeness
6	INS	left	closeness
7	CAC	left	eigenvector
8	PC	left	eigenvector
9	HIPP	right	pagerank
10	HIPP	right	closeness
11	HIPP	right	strength
12	BSTS	left	strength

Table 4.3 continued from previous page

13	AMYG	left	strength
14	PARC	left	eigenvector
15	PCAL	left	eigenvector
16	ISTC	left	eigenvector
17	ENT	left	strength
18	PCUN	right	strength
19	PCUN	left	eigenvector
20	PC	right	eigenvector
21	AMYG	left	pagerank
22	BSTS	left	closeness
23	PCAL	left	closeness
24	CAC	right	eigenvector
25	LING	left	strength
26	PCUN	right	pagerank
27	ENT	left	pagerank
28	AMYG	right	strength
29	LOCC	left	closeness
30	HIPP	left	closeness
31	PARC	right	eigenvector
32	PU	left	pagerank
33	AMYG	right	pagerank
34	RAC	right	closeness
35	HIPP	left	strength
36	LING	right	betweenness
37	INS	left	betweenness
38	CUN	left	eigenvector
39	POPE	right	betweenness
40	HIPP	left	pagerank
41	PU	left	strength
42	LOCC	right	pagerank
43	FP	right	betweenness
44	AMYG	right	closeness
45	PARH	right	closeness
46	THAL	right	closeness
47	INS	right	strength
48	CUN	left	strength
49	THAL	left	closeness
50	FUS	right	strength
51	BSTS	left	pagerank

Table 4.3 continued from previous page

52	CUN	left	closeness
53	SP	left	eigenvector
54	FP	left	betweenness
55	RAC	right	strength
56	INS	right	pagerank
57	CUN	right	eigenvector
58	SF	right	closeness
59	PC	right	betweenness
60	CUN	right	strength
61	RAC	right	betweenness
62	THAL	right	eigenvector
63	LING	left	pagerank
64	RMF	left	pagerank
65	IT	right	closeness
66	ENT	left	betweenness
67	RMF	left	strength
68	SF	left	eigenvector
69	LOCC	left	strength
70	PCAL	right	closeness
71	RMF	left	closeness
72	CAC	left	betweenness
73	LOCC	right	strength
74	PC	right	strength
75	AMYG	left	eigenvector
76	LING	left	closeness
77	RAC	right	eigenvector
78	TT	left	pagerank
79	IP	right	betweenness
80	PC	right	closeness
81	SMAR	right	strength
82	ACC	right	pagerank
83	TP	right	closeness
84	PC	right	pagerank
85	FUS	right	pagerank
86	CMF	left	eigenvector
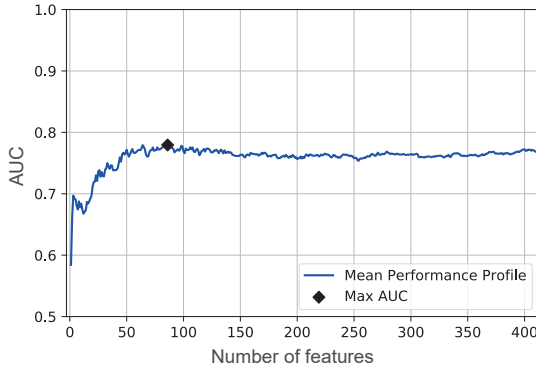
(a)
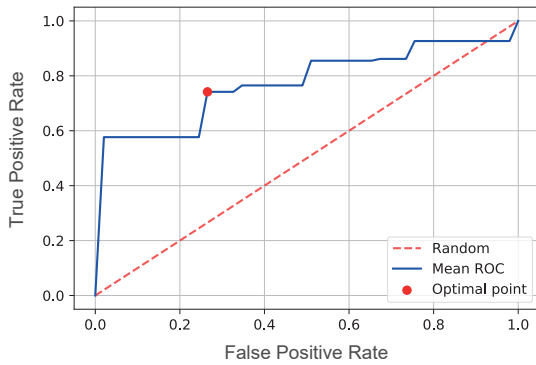
(b)

Figure 4.7. Machine learning analysis to predict dementia based on centrality metrics using the ADNI dataset. (a) Mean performance profile computed as a function of the number of features included in the training process of radial SVMs (with $C = 100$). The most relevant features are identified at smaller values of the x-axis, so features were added progressively according to their relative importance. The max AUC, black diamond, was achieved with the first 86 most important features. (b) Mean ROC curve generated from the features identified in (a). Sensitivity, specificity and accuracy indices were computed at the optimal point (red circle). Such point was identified as the closest point (in terms of Euclidean distance) on the ROC curve to the point defined by a true positive rate of 1 and false positive rate of 0.

(a)

(b)
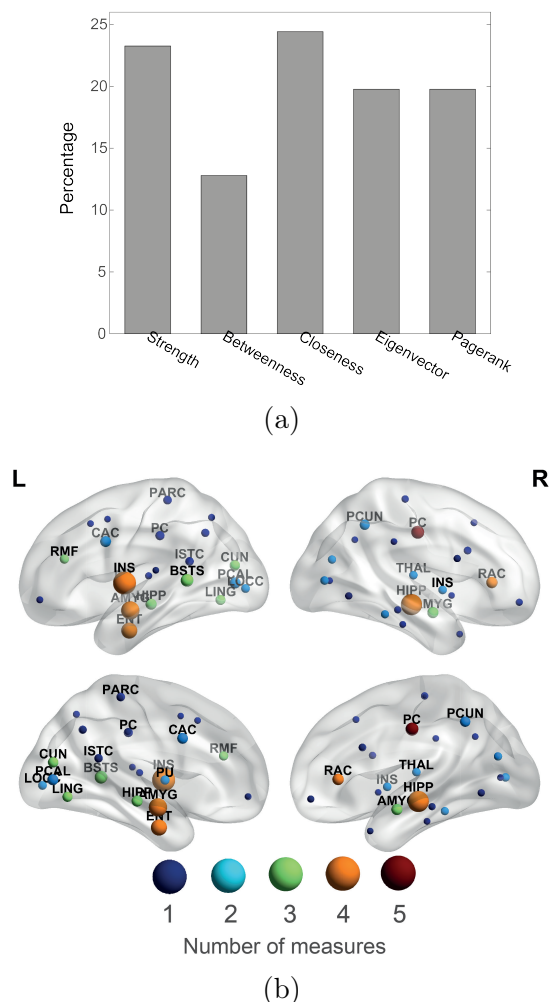
Figure 4.8. Identification of relevant centrality measures and brain regions. (a) Bar chart representing the proportion of each centrality measure that was included in the final set of selected features. (b) Brain map representing the most predictive regions to classify between dementia and healthy control. Lateral and medial views are shown on the top and bottom rows, respectively. Node size is proportional to its relative importance, which was computed from the feature ranking. Node color encodes the number of centrality measures included in the final set of features referring to that specific region. Abbreviations are shown for those regions having a relative importance above the median.

To identify the most characteristic areas of dementia, we summed the feature importance scores of the network features referring to the same area, obtaining the relative importance of individual areas (Figure 4.8b). The entorhinal cortex, insula and subcortical structures, such as the hippocampus, amygdala, putamen and thalamus, are highly discriminative in detecting Alzheimer's dementia, especially in the left hemisphere. Other regions playing an important role to distinguish between controls and patients are the posterior cingulate and precuneus cortices, with the right hemisphere showing a greater relevance. The left occipital lobe and surrounding areas (the isthmus division of the cingulate cortex and the banks of the superior temporal sulcus) are also critical for diagnostic separation. The rostral anterior division of the right cingulate cortex, along with the caudal anterior division of the left cingulate cortex, the left paracentral lobule, and the rostral division of the left middle frontal gyrus capture relevant effects. Other regions from frontal and parietal lobes are further relevant for classification, although to a lesser extent.

The applied cross-validation scheme allows computing the classification performance while controlling for overfitting, but does not provide a single predictive model. We therefore fitted a final SVM based on the 86 selected features using all ADNI samples and this model was tested on the NKI simulated dataset.

4.3.2   Predictions in the simulated disease progression

We incorporated the NKI dataset to simulate 16 disease stages and their corresponding age-matched normal phases, relative to individuals following an AD-related pathological (NKI-II group) and healthy (NKI-I group) pathway, respectively. For the pathological pathway, different trajectories were simulated to identify the model parameters resembling dementia brain patterns at simulated stage 0, as compared with the ADNI dataset. Upon parameter optimization, the hippocampus was identified as the most likely origin of Alzheimer's disease (with $\alpha = 0.3$ and $\beta^{AD} = 0.04$). Other regions, especially the amygdala and entorhinal cortex, are plausible seed candidates wherein Alzheimer's disease first originates (Figure 4.9).

Using the hippocampus as seed region, we produced connectivity matrices either representing individuals normally aging or individuals developing Alzheimer's disease, and the ADNI classifier, which was only based on the relevant features associated with dementia (Figure 4.8a), was evaluated on these structural networks (Figure 4.10a). To estimate the cutoff stage from which network alterations associated with dementia begin to manifest

Figure 4.9. Parameter optimization of the disease progression model. Upon applying dynamical simulations using the NKI dataset, this figure assesses which seed region is most likely to reproduce the differences in node strength measured between ADNI control and ADNI patients. For each region, we explored the parameter space given by α and β^{AD} to find the minimum of the cost function (see subsection 4.2.3). The hippocampus, which is highlighted in red, turned out to be the very first region affected by Alzheimer's disease. Subcortical regions are shown in italic font.

structurally, we calculated the significance of classification performance measures throughout the simulated progression span. Interestingly, we observed that the selected centrality metrics still captures significant dementia alterations at the simulated stage -7 (Figure 4.10b). Classification performance progressively improved as Alzheimer's disease progressed (Figure 4.10a), achieving more accurate predictions as the effect of the disease becomes more prominent. Note that this improvement comes from the rise in the sensitivity index, whereas specificity remains relatively stable across simulated stages. At very early stages, both simulated controls (NKI-I subjects) and simulated patients (NKI-II subjects) are generally classified as controls, when the impact of dementia on brain connectivity is yet subtle.

(a)

(b)

Figure 4.10. Classification across simulated stages using the hippocampus as seed region. (a) A final SVM based on the most discriminative features of dementia (Figure 4.8a) was fitted using all ADNI subjects. This predictive model was then employed to classify between simulated patients and simulated controls across the progression span produced with the NKI dataset. Performance measures of AUC, sensitivity, specificity and accuracy were computed at each stage. (b) Based on the AUC and accuracy indices, network alterations associated with dementia begin to manifest structurally at the simulated stage −7.

We finally explored the evolution of predictions when the remaining 40 brain areas served as seed region to initiate the propagation of the disease factor (Figure 4.11). Interestingly, those regions most likely to be the origin of the disease (Figure 4.9) offer a gradual increase in classification performance throughout simulated stages. This effect is largely visible for the amygdala and the entorhinal cortex. When Alzheimer's disease simulation originated from these areas, performance measures were comparable with the optimal seed (*i.e.*, the hippocampus).
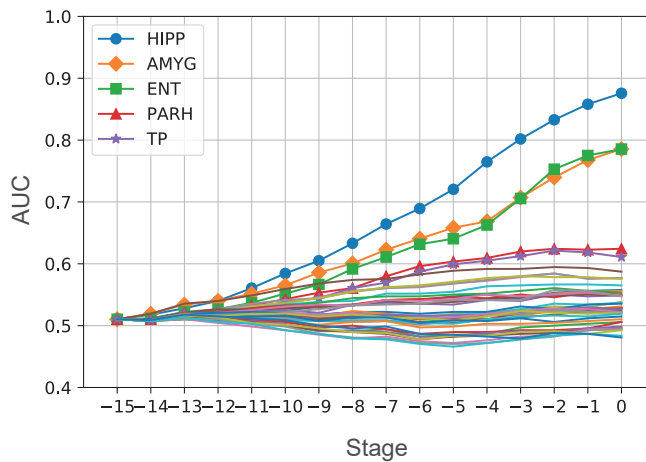
Figure 4.11. Classification performance along the disease progression when using different seeds. The AUC index was calculated at each simulated stage when individual regions were set as origin to initiate the propagation of the disease factor. Hippocampus, amygdala and entorhinal cortex structures offered a similar roughly linear trend.

4.4 Discussion

The field of network neuroscience provides a compelling framework to generate mechanistic models about brain disease and identify useful biomarkers (Bassett and Sporns, 2017; Kaiser, 2013). In this work, we have proposed an approach grounded on network neuroscience to assess the potential of structural brain networks as measured with dMRI in prodromal dementia. The main findings uncovered in this work suggest that:

1. Centrality measures of dMRI networks are informative for Alzheimer's dementia diagnosis.

2. The most discriminative network features are largely associated with medial temporal and subcortical brain regions, as well as posterior structures of the DMN and occipital areas.

3. The hippocampus is the likely origin of Alzheimer's disease.

4. Pathophysiological alterations associated with dementia become significantly apparent at the simulated stage -7, presumably before meeting diagnostic criteria for clinical dementia.

4.4.1 Prediction of Alzheimer's disease using real-world data

It has been suggested that the pathophysiological processes in Alzheimer's disease largely disturb hub regions (Stam, 2014; Tijms et al., 2013). Here, we have applied sophisticated multivariate techniques to predict dementia based on 86 features quantifying the centrality of individual nodes, obtaining significant classification performance: sensitivity of 74.17% ($P = 1.69 \times 10^{-3}$), specificity of 73.47% ($P = 1.69 \times 10^{-3}$), and accuracy of 73.82% ($P = 9.76 \times 10^{-6}$).

Earlier investigations have developed classifiers to distinguish Alzheimer's disease patients in different phases or stages from healthy controls. Klöppel et al. (2008) developed a classifier based on atrophy-realted measures and they reported 89% accuracy in separating patients with mild dementia from matched controls. Based on characteristics extracted from the gray matter, Magnin et al. (2009) achieved values of 94.5%, 91.5% and 96.6% for accuracy, sensitivity and specificity, respectively, in detecting dementia. However, their dataset comprises a rather small number of patients (5 male / 11 female), and so it is problematic to generalize these high accuracies. Using connection weights as features extracted from diffusion MRI, Zhan et al. (2015) systematically compared different tractography algorithms for classification. They concluded that the ability of classifying between dementia and control conditions was higher than comparisons between dementia and MCI conditions. By contrast, Ebadi et al. (2017) developed an ensemble classification module based on graph metrics to perform classification across diagnostic groups. These authors obtained better classification performance when classifying between dementia and MCI conditions (accuracy of 83.3%) than when distinguishing patients with dementia from healthy controls (accuracy of 80%). Based on connection weights, Shao et al. (2012) achieved classification

accuracies greater than 95 % using data from 17 patients. Other studies have developed predictive models to estimate which MCI individuals will develop dementia within a certain time window. For example, a recent study using amyloid imaging (Mathotaarachchi et al., 2017) has reported values of 84 % and 0.91 for accuracy and AUC, respectively, when assessing the progression to dementia within two years. Although the classification performance demonstrated in our work appears relatively modest, a comparison across studies is not straightforward due to variations in predictors, datasets or patient's disease stage.

4.4.2 Discriminative brain signatures of dementia

There is literature supporting a stereotypical pattern of neurodegeneration in Alzheimer's disease that is associated with tau pathology of Braak staging (Braak et al., 2006; Whitwell et al., 2008). At early stages, atrophy largely occurs in the entorhinal cortex, hippocampus and posterior structures of the DMN (Buckner et al., 2009; Frisoni et al., 2010; Seeley et al., 2009; Whitwell et al., 2008). From these regions, atrophy then extends to the lateral temporal cortex, dorsal parietal and frontal cortex. Finally, sensorimotor and visual cortices are affected at late stages (Frisoni et al., 2009; Pini et al., 2016). In this work, the relevant features extracted using the ADNI dataset uncovered a set of brain regions that are highly predictive of dementia: the entorhinal cortex, insula, hippocampus and other subcortical structures, as well as posterior structures of the DMN and the occipital lobe. Our results are in line with previous literature, with medial temporal and subcortical structures having a greater weight for classification.

4.4.3 Spreading process and Alzheimer's disease

Our computational model is in accordance with previous work. In particular, we model the degradation of structural connectivity (dynamics of networks) based on the disconnection hypothesis (Brier et al., 2014; Delbeuck et al., 2003) as the disease factor spreads (dynamics on networks). The most plausible scenario was when the disease is initiated in the hippocampus, as well as in the entorhinal cortex and amygdala. Numerous studies have shown levels of atrophy and functional disruption in the hippocampus and the entorhinal cortex at very early stages of the disease (Brier et al., 2014; Buckner et al., 2009; Frisoni et al., 2010). The initial Braak stages are also characterized by the presence of tau proteins in these areas, which in turn extend to the amygdala (Braak et al., 2006).

There is a correspondence between the Alzheimer's disease-associated features identified in this work and relevant patterns identified by other researchers. When using raw streamline counts, one cannot dissociate changes due to connectivity itself from changes emerged from spatial properties (e.g., changes in volume) (Sotiropoulos and Zalesky, 2017; Taylor et al., 2015). Our computational model is capturing both effects together since our objective was not to assess their contributions separately to structural connectivity. This might also partially explain the correspondence between the relevant features identified in this work and the atrophy patterns identified by other researchers using sMRI. Along these lines, eigenmodes derived from a network diffusion model recapitulate atrophy patterns measured in Alzheimer's disease and behavioral frontotemporal dementia (Raj et al., 2012). This model relies on a diffusive mechanism where a disease agent accumulates in brain areas giving rise to atrophy. The same authors extended their approach by predicting both atrophy and metabolism in Alzheimer's disease (Raj et al., 2015). Iturria-Medina et al. (2014) describe a spreading model to reproduce regional amyloid-β patterns measured with PET imaging. Their model also incorporates a term capturing mechanisms of amyloid-β clearance. Overall, these brain models illustrate that both atrophy and amyloid-β patterns can be explained by disease agents that propagate in a prion-like manner (Frost and Diamond, 2009). These findings are further supported by recent work showing that intrinsic functional connectivity cannot explain the tendency for strongly connected nodes to have more tau pathology (Cope et al., 2018).

4.4.4 Network alterations in the simulated disease progression

We found that a classifier based on centrality features using the ADNI dataset provides significant predictions in the simulated progression process. In particular, AUC and accuracy indices becomes significant at simulated stage -7 onwards. At this stage, clinical symptoms may not yet be detectable: assuming that Alzheimer's disease progresses continuously at a constant rate, our model suggests that alterations associated with dementia could be detected up to seven years before the diagnosis established in the ADNI database. Hence, our model simulations suggest a valuable opportunity for risk assessment and early diagnosis. Moreover, our simulations highlight the possibility that neural structure may be significantly compromised before physiological deficits become evident, possibly due to compensatory plasticity (Savioz et al., 2009). Nevertheless, Alzheimer's disease progresses at different rates in actual subjects. Consequently, a direct link between simulated stages and years of progression might be subject to large inter-subject variation.

4.4.5 Limitations

When applying the SI model, we have assumed that once the disease agent reaches a region, connections are always degraded. As a result, the task of classifying simulated groups turned out to be less tricky since the disease factor affects many structural links. Note that the classification performance obtained at the simulated stage 0, which attempts to emulate a dementia stage, was greater (AUC of 0.88) as compared with ADNI (actual) data (mean AUC of 0.78). Nevertheless, the fact that significant predictions are achieved when using a classifier fitted with real-world controls and matched patients with dementia suggests that our model could capture differences encountered in early Alzheimer's disease progression.

The final set of discriminative brain signatures included medial temporal and subcortical structures, which are thought to be disrupted at early stages (Mak et al., 2017). However, it is important to acknowledge that the relevant features were extracted from ADNI patients with dementia, which is not a prodromal phase. Thus, future research could incorporate data from patients at earlier stages (*e.g.*, before or during the MCI phase and prodromal dementia) for a definitive validation. For instance, our model could be tested retrospectively for patients that were scanned within the UK Biobank project (Miller et al., 2016) before disease onset. Importantly, one should include individuals with an age range in agreement with the simulated period, as Alzheimer's disease is an age-dependent disorder and brain patterns differentiating between conditions could vary across age ranges. Moreover, subject-specific dynamics could be included in more detailed progression models. As patients might be affected by cerebrovascular diseases (Santos et al., 2017) and other copathologies such as alpha synuclein (Wirths and Bayer, 2003), the diagnosis could be enhanced by accounting for these comorbidities. On the other hand, as new information about the selective neural vulnerability in Alzheimer's disease is gathered (Saxena and Caroni, 2011), more complex models could be implemented to mimic mechanisms of degeneracy and reserve (Fornito et al., 2015; Iturria-Medina et al., 2014). This would also enable a more mechanistic modeling of aging, as the aggregation of misfolded proteins in the brain is part of the normal aging process (Fjell et al., 2014). Finally, studying Alzheimer's disease using multimodal imaging technology will likely contribute to a more precise identification (Teipel et al., 2015).

4.5 Conclusions

Computational models of disease progression, based on knowledge about structural connectome pathways for spreading, are an approach to discover risk factors and biomarkers of brain network diseases (Kaiser, 2013). We have used such a model to study the progression from networks of healthy controls to networks showing features of Alzheimer's disease patients. This highlights centrality as an early risk factor of developing dementia. Overall, our work identifies potential anatomical origins of Alzheimer's disease, and suggests a diffusion MRI-based biomarker for early diagnosis.

Chapter 5

Functional brain network alterations in alcohol use disorder

Statistical dependence measures computed between BOLD signals can inform about brain functional states in studies of neurological and psychiatric disorders. Furthermore, its non-invasive nature allows comparable measurements between clinical and animal studies, providing excellent translational capabilities. In the present chapter, we apply the NBS approach to investigate alterations in the intrinsic functional connectivity of the rat brain in a PD state, an established animal model of clinical relevant features in alcoholism.

5.1   Introduction

Functional MRI has greatly influenced the study of brain function (Friston, 2002). In particular, fluctuations in fMRI signals measured with BOLD contrast have proved to be a potential tool to assess the impact of a variety of neurological and psychiatric disorders on brain dynamics (Stam, 2014). Analytic approaches developed within graph theory and network science have been successfully applied to examine brain connectivity (Bullmore and Sporns, 2009). As a result, the field of connectomics (*i.e.*, the mapping of structural and functional connections in the brain) has increasingly gained prominence (Smith et al., 2013; Sporns et al., 2005).

Functional connectivity estimates the statistical dependence between activity time courses recorded from areas spanning the brain (Friston, 2011). Although functional connectivity patterns can be measured in both task-evoked and resting-state experiments (Smith et al., 2009), its use in rs-fMRI studies has notably increased since subjects are not engaged in a particular task. In turn, patients suffering from disorders with cognitive limitations (*e.g.*, alcoholism and Alzheimer's disease) can be reliably examined and compared against a matched control group to identify differences in functional connectivity and imaging biomarkers (Craddock et al., 2009; Fornito et al., 2012).

Alcoholism is a drug dependence-related disorder that involves a complex interdependence between neurological and environmental variables. The latter includes factors such as age, gender and family as well as economic and cultural contexts (World Health Organization, 2014). From a neuroscientific point of view, alcohol intake has shown to disturb diverse human brain networks, such as the DMN, the integrative executive control, the salience and the subcortical reward networks (Chanraud et al., 2011; Müller-Oehring et al., 2014). Nevertheless, the main limitation of assessing alcohol addiction in humans lies in that alcohol intake is often accompanied by the consumption of other drugs and comorbidity with other psychiatric conditions including depression and anxiety disorders, and the difficulty to follow brain changes along the trajectory towards the pathological state (Feldstein Ewing et al., 2014). Thus, differences measured between groups can be due to the main effect of other drugs or the interaction among them, rather than alcohol itself. In this context, the use of animal models allows having a greater experimental control and faithfully investigate the effect of interest under study (Meinhardt and Sommer, 2015).

In this work, we examine the effect of chronic and intermittent alcohol exposure, as usually occurs in humans, on spontaneous fluctuations in BOLD

signals by comparing large-scale functional brain networks between control and postdependent Wistar rats.

5.2 Materials and methods

5.2.1 Animals and MRI acquisition protocol

The PD rat model was specifically developed to test the role of negative affect as a key driving force in a perpetuating addiction cycle (details in Sommer et al. (2008)). In this model, rats are made dependent by chronic intermittent exposure to alcohol, and it has been previously demonstrated that these animals show long-lasting excessive consumption of and increased motivation for alcohol, and evidence for loss of control over alcohol intake (Meinhardt et al., 2013), making it a well-established and widely used animal model of alcohol use disorder.

Experiments were carried out in a horizontal 7 Tesla scanner with a 30 cm diameter bore (Biospec 70/30v, Bruker Medical, Ettlingen, Germany). The system had a 675 mT/m actively shielded gradient coil (Bruker, BGA 12-S) of 11.4 cm inner diameter. A 1H rat brain receive-only phase array coil with integrated combiner and preamplifier, no tune/no match, in combination with the actively detuned transmit-only resonator (BrukerBioSpin MRI GmbH, Germany) was employed. Data were acquired and processed with a Hewlett-Packard console running Paravision 5.1 software (Bruker Medical GmbH, Ettlingen, Germany) operating on a Linux platform.

For the rs-fMRI experiments, 14 control and 13 PD Wistar rats were anesthetized with urethane (1.2 g/Kg). Anesthetized animals were placed in a custom-made animal holder with adjustable bite and ear bars, and positioned on the magnet bed. The animals were constantly supplied with 0.8 L/m O2 with a face mask and temperature was kept between 36.5 and 37.5 °C through a water heat-pad. The temperature, heart rate, SpO2, and breathing rate were monitored throughout the session (MouseOx, Starr Life Sciences, Oakmont, US).

T2-weighted anatomical images were collected using a RARE sequence, applying the following parameters: FOV = 40×40 mm^2; 15 slices; slice thickness = 1 mm; matrix size = 128×128; TEeff = 56 ms; TR = 2 s; RARE factor = 8. The B0 field distribution in a large voxel ($40 \times 40 \times 40$ mm^3) containing the whole head was acquired. Briefly, the brain was localized with

T2-weighted RARE sequence, and first- and second-order shims adjusted with MAPSHIM application in a sufficiently large voxel containing the whole brain. Functional MRI acquisition was performed using a GRE-EPI sequence in 30 coronal slices applying the following parameters: FOV = 25 × 25 mm²; slice thickness = 0.5 mm; matrix size = 50 × 50; segments = 1; FA = 60°; TE = 15 ms; TR = 2000 ms (300 samples per run, 10 min), rendering an isotropic voxel of 0.5 × 0.5 × 0.5 mm³. Between one and three runs were acquired from each animal. T2-weighted anatomical images with exactly the same geometry were collected using a RARE sequence using the following parameters: FOV = 25 × 25 mm²; 30 slices; slice thickness = 0.5 mm; matrix size = 200 × 200; TEeff = 56 ms; TR = 2 s; RARE factor = 8.

5.2.2 Preprocessing of MRI data

Every functional run was preprocessed using *FSL v5.0* (FMRIB Software Library, `https://fsl.fmrib.ox.ac.uk/fsl/fslwiki/`) (Jenkinson et al., 2012) and Matlab *2014a* (The MathWorks, Inc., Natick, MA, United States, `https://www.mathworks.com/`) as follows. First, voxel size was resized by a factor of 10 (as typically performed in rodent data (Kalthoff et al., 2011)). Afterwards, functional volumes were realigned using a rigid body transformation and taking the very first volume of each subject as reference. In addition, this realignment was carried out slice by slice (translation in x and y, and rotation in z) to reduce breathing-related variance (Kalthoff et al., 2011). Next, we extracted the brain and set the global mean intensity to 1000. Spike detection was then performed using *DVARS* measure (Power et al., 2012). No run was discarded since none of them had more than 30 spikes (out of 300 samples). Leveraging a multilinear regression model, each individual voxel was corrected for:

- The three rigid body parameters (translation in x and y, and rotation in z) previously computed and their derivatives (backward difference).

- A single regressor per spike with a "*b0, f0*" window (Satterthwaite et al., 2013) (*i.e.*, neither preceding nor following samples were used).

- The global signal and its derivative (backward difference).

- Two regressors modelling the mean and a linear trend.

No spatial smoothing was applied to avoid a mixture of signals within ROIs, whereas band-pass filtering was performed after ROI signal extraction (see subsection 5.2.3). Spatial transformations were estimated to be applied during

construction of functional networks (subsection 5.2.3). In particular, functional data were co-registered to the brain-extracted T2-weighted image using a rigid body transformation and then normalized to a widely used rat template described elsewhere (Schwarz et al., 2006) using an affine transformation.

5.2.3 Construction of functional brain networks

To investigate connectivity changes over the whole brain, a total of 47 bilateral ROIs covering most part of the rat brain were selected. Twenty-six cortical ROIs were analyzed, including structures of the hippocampal formation, prefrontal, insular, association, sensory and motor cortices, as well as 21 subcortical ROIs including, among others, striatal regions, amygdala, thalamus, ventral tegmental area, and hypothalamus. These ROIs were automatically delineated through using a 3D digital atlas referring to PWS (Paxinos and Watson, 1998; Schwarz et al., 2006). Functional images were kept in their native space and the mean time courses within each ROI were extracted and converted to z-scores, that is, ROI signals were normalize to have zero mean and unit variance. A Fast Fourier transform-based filter was applied to retain those frequencies between 0.01 and 0.1 Hz. Afterwards, those time samples deemed as spikes were removed and the functional interaction between pairs of regions was estimated by using the Pearson correlation coefficient. Correlations were converted to Fisher's z-values. Finally, matrices across runs were averaged within each animal to obtain a 47×47 subject-specific functional network.

5.2.4 Network-based statistic

When testing differences in edge weights between conditions, one must deal with the problem of multiple comparisons to control for the family-wise error rate (FWER). The more regions are included in the analysis, the more stringent the statistical threshold used to declare a significant change should be. This is especially critical when changes in functional connectivity are widely and weakly distributed across several links and they are not limited to certain connections (Zalesky et al., 2010). In that scenario, one would likely miss a difference between conditions. To overcome this limitation, we made use of the *NBS Toolbox v1.2* (Zalesky et al., 2010), which assesses functional connectivity differences by accounting for the connected structure of brain regions (Figure 5.1), to identify differences in functional connectivity between control and PD rats. First, a univariate test statistic is independently applied at every network connection to compare the two groups (Figure 5.1a). For

example, a t-test can be computed to evaluate whether functional connectivity is greater in control condition compared to PD condition (*i.e.*, control > PD). This first step provides a statistic matrix (Figure 5.1b, left), which is then thresholded by a primary threshold, t_{th}, to identify suprathreshold links (Figure 5.1b, middle) and subsequently the connected components[1] (Figure 5.1b, right). These connected components can be treated as subgraphs or subnetworks. The size of each identified subnetwork is then quantified by counting the number of links forming it. A component size is compared to a null distribution of maximal component size using permutation testing. Finally, a subnetwork is considered to be statistically significant whether the P-value based on its size is lower than a specific threshold, P_{th}.

In this work, a threshold of $t_{th} = 3.1$ was selected. Differences in functional connectivity were tested in both directions (*i.e.*, control > PD and control < PD) by using 10,000 permutations. A component size was declared as significant whether its P-value was lower than $P_{th} = 0.05/2\,(0.025)$. For comparison, mass-univariate tests were also performed to identify differences in individual connections. Individual P-values were calculated by permutation testing (10,000 permutations). In this case, multiple comparisons were controlled by using the Benjamini-Hochberg FDR (Benjamini and Hochberg, 1995) procedure with $q = 0.05$.

5.3 Results and discussion

Figure 5.2 presents the average functional matrices in both conditions. First, differences in functional connectivity patterns were investigated by individually looking at each link. We did not find significant differences in any contrast when using mass-univariate tests. The NBS method was then applied with the aim of increasing statistical power to obtain potentially connected structures showing differences between conditions.

When looking for subnetworks wherein the activity was greater after alcohol exposure, we did not find significant changes. Conversely, NBS revealed a significant subnetwork ($P = 0.01$) composed of 5 brain structures within which functional connectivity values were greater in the control condition. This subnetwork was composed of three cortical regions (the anterior and the posterior part of the dorsal hippocampus, and the temporal cortex) and three subcortical areas (lateral hypothalamus, central amygdala and raphe nucleus) (Figure 5.3). This result highlights a central role of the

---

[1]In a connected component, there is a path between any pair of nodes.
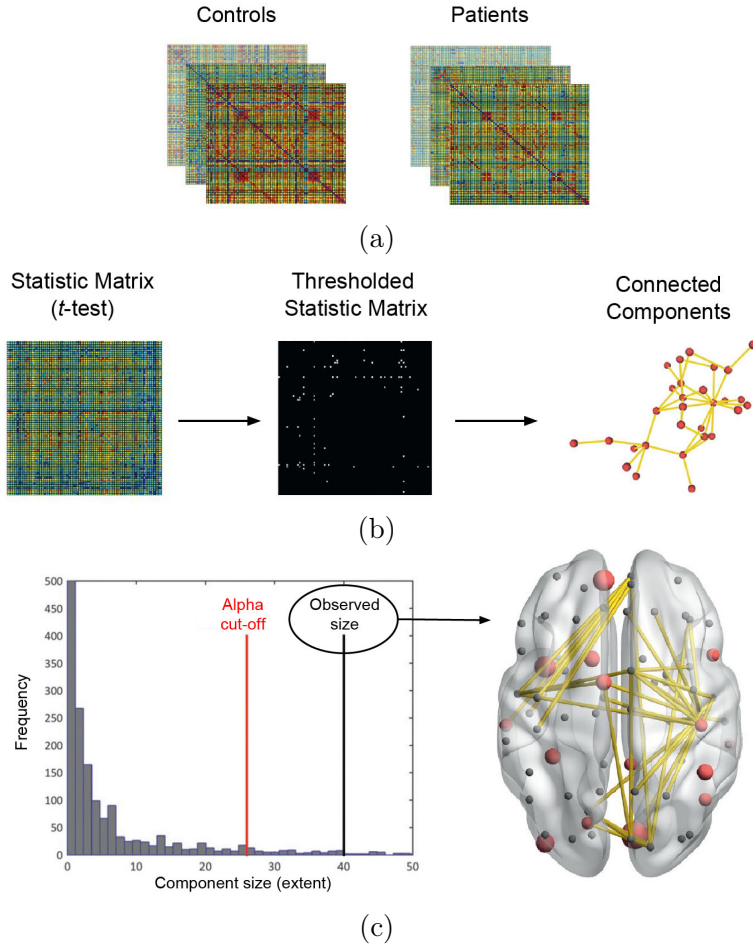
Figure 5.1. Steps comprising the NBS approach. (a) Functional brain networks from controls (left) and patients (right) are used as input. (b) A test statistic (a *t*-test in this case) is calculated for each connection (*e.g.*, between the hippocampus and amygdala), given rise to a statistic matrix (left). Each matrix entry is then compared to a primary threshold, t_{th}, to generate a thresholded and binarized statistic matrix (middle). The connected components are identified and the size of each component (as measured with the number of links) is calculated. A particular connected component is shown (right). (c) The significance of a component size is evaluated (left). A component size with a *P*-value lower than a specific threshold, P_{th}, is declared as significant, indicating that functional connectivity within that component is greater in a condition compared to the other (depending on the hypothesis being tested) (right). Adapted from Fornito et al. (2016).

Figure 5.2. **Group functional brain networks obtained in control and postdependent conditions**. Color scale represents the strength of functional interactions between pairs of nodes.

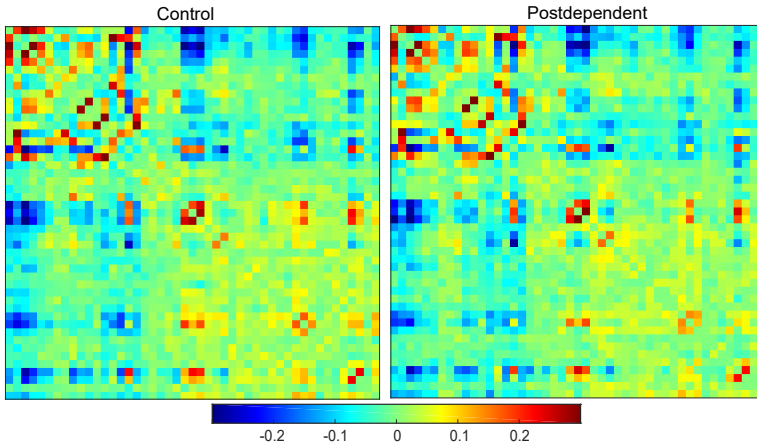hippocampus in the postdependent state, showing a disconnection of this structure from all identified subcortical regions. In Figure 5.4, we present the functional connectivity values in each of the links conforming the obtained subnetwork. As shown, positive correlations decrease or become negative (anticorrelated) after intermittent alcohol exposure, hence suggesting a functional disconnection.

The NBS method was proposed to provide a gain in statistical power (Zalesky et al., 2010). However, it is important to highlight that we are not able to declare an individual link as being different between conditions, as we are evaluating the subnetwork as a whole. Indeed, this method suffers from two main drawbacks. First, the obtained results are very sensible to the threshold t_{th}, as the size of the connected structures relies critically on it. A high enough t_{th} was chosen to avoid large subnetworks arising from permuted data just by chance (Zalesky et al., 2010). On the other hand, as NBS works at subnetwork-level, it loses capacity to pinpoint which specific functional interactions are actually disrupted. By contrast, one can argue that, due to the connected nature of the brain, many neurological disorders tend to spread over many regions, rather than being confined within a discrete brain structure (Raj et al., 2012). In turn, differences in functional connectivity patterns might be reflected across several links, and this fact is exploited by NBS.

The interpretation of negative correlations is very challenging in the study of brain connectivity through using fMRI, as the mechanisms governing fluctuations of BOLD signals and their relationship with concomitant neural activity is not completely understood (Moreno et al., 2013). This is especially relevant when the global signal is included as a nuisance covariate during the preprocessing stage (as performed in this work, see subsection 5.2.2) (Murphy et al., 2009). An important choice must be made if one wants to compare
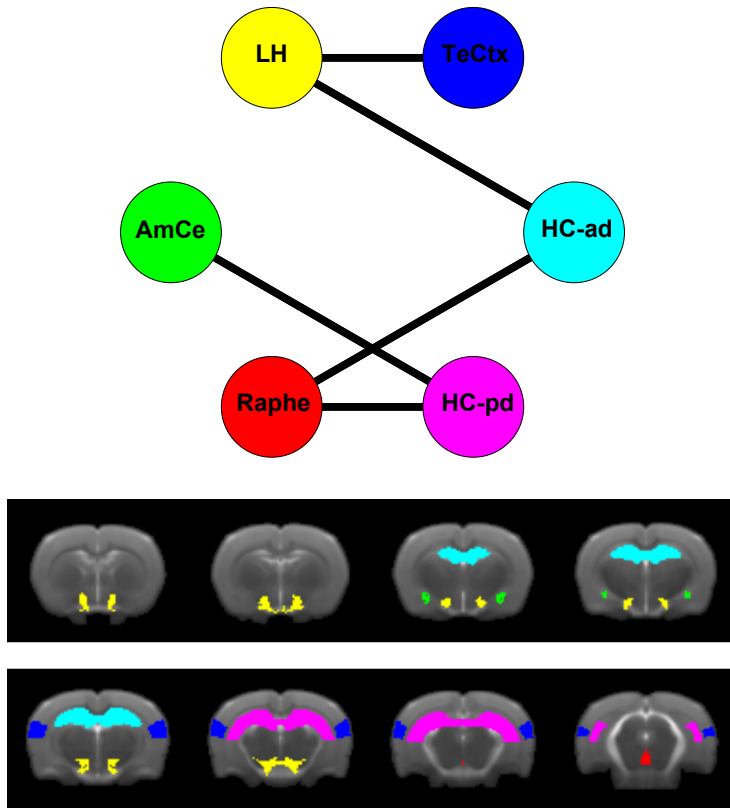

Figure 5.3. Significant changes obtained with the NBS approach. Functional connectivity within this subnetwork is decreased after alcohol intake. TeCtx: temporal cortex; HC-ad: hippocampus antero-dorsal; HC-pd: hippocampus postero-dorsal; AmCe: amygdala central; LH: hypothalamus lateral.
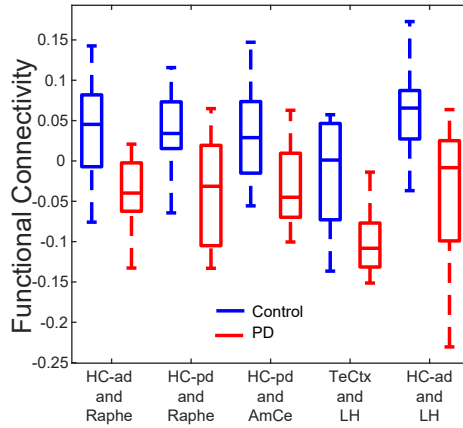
Figure 5.4. Boxplots representing the group functional connectivity values from control and PD condition and for each link. TeCtx: temporal cortex; HC-ad: hippocampus antero-dorsal; HC-pd: hippocampus postero-dorsal; AmCe: amygdala central; LH: hypothalamus lateral.

correlations (or the corresponding Fisher's z-values) between different groups. In particular, *should we take the absolute value of correlations?* By doing this, one is implicitly acknowledging that the functional interaction between two areas quantified by a value of -0.4 is the same as a value of 0.4. On the other hand, if one takes the raw values to carry out comparisons, a functional connectivity value of 0 (no correlation) is deemed as being greater than -0.4 (strong negative correlation). Until these issues are sorted out, most likely in combined electrophysiological–fMRI experiments, the obtained results should be interpreted with caution (Murphy et al., 2009). In this study, the interpretation have been one of classical neurophysiology, this is, that anticorrelated neuronal populations exchange less information.

5.4 Conclusions

In this work, we have shown that the PD state associated with alcohol use disorder modifies functional connectivity measured in resting-state networks. We have also shown the advantage of using the NBS method to identify alterations in interconnected structures. The results suggest the existence of a subnetwork of hippocampal and subcortical structures relevant to addiction

that is disconnected in the PD state. Further research is required to evaluate the clinical potential of the identified regions. Importantly, the effect of fMRI data preprocessing on functional connectivity estimates should be explored in depth to evaluate the robustness of the resulting subnetwork, as the relationship between the BOLD signal and the concomitant neural activity is not well understood (Buxton, 2010; Friston, 2011; Moreno et al., 2013). Nevertheless, our results are generally supported by available molecular and neurobiological data from this animal model (Sommer et al., 2008; Uhrig et al., 2016), hence suggesting the relevance of the identified subnetwork as potential target for therapeutic approaches.

Chapter 6

Conclusion

Network science provides a lucrative framework to formally investigate numerous neural phenomena by considering the brain as a complex system constituted of regions or areas that are connected to each other. The main objective of this thesis was to investigate the macroscopic organization of the brain in health and disease under the perspective of network science. More concretely, we have examined both structural and functional brain networks. In order to contribute to the field of network neuroscience and further demonstrate the potential of network science tools to understand brain structure and function, we have conducted three specific investigations (chapters 3 to 5).

We have demonstrated that the topology of structural connections in the healthy cerebral cortex plays a critical role in shaping functional patterns in resting-state. The *Spearman* correlation between the structural weights of the rat connectome and their counterpart functional interactions was of 0.48. This analysis reveals that structural and functional brain networks are coupled, but does not account for network-level effects. A distinctive characteristic of the brain, as well as of any complex network, is its connectivity. That is, brain regions are not isolated but are constituted part of a connected system. As a result, it is important to consider properties emergent from the inter-relation between regions. Brain regions that belong to the same module in functional brain networks tend to mutually structurally interact between each other compared to regions located in different functional modules. Additionally,

densely connected structural motifs (*i.e.*, classes 12 and 13 for motif size $M = 3$) are enriched within functional modules. Therefore, communication among neural elements are strongly influence by the way they are connected.

Making use of rodent models and MRI data allowed us to investigate how brain function is influenced by the directionality of structural connections. Interestingly, rodents can be functionally experimentally manipulated to investigate how local perturbations impact on the global neural dynamics. In this way, an intriguing question that might be addressed in future research would be that of investigating the community structure of functional brain networks derived upon manipulating specific nodes (*e.g.*, hubs) and how the motif frequency spectrum changes within the resulting modules.

Hub nodes facilitate efficient communication between neural systems and the failure of central regions is thought to be a possible final common pathway in many neurological and psychiatric disorders. Along these lines, distinguishing Alzheimer's disease patients with dementia from healthy controls is possible by using dMRI networks and measures quantifying the centrality of individual regions (AUC = 0.78 ± 0.16, mean $\pm$ SD). In particular, strength and closeness are the most relevant measures for Alzheimer's dementia diagnosis (representing the 23.25% and 24.42% of the selected features, respectively), followed by eigenvector and pagerank (19.77% in both cases) and, lately, betweenness (12.79%). These relevant features are largely associated with medial temporal and subcortical structures, the posterior cingulate and precuneus cortices, and occipital regions.

Dynamical processes occur in many real-world networks. To evaluate the potential of dMRI technology in the search for biomarkers for early diagnosis of Alzheimer's disease, we incorporated dynamics along with the topology of structural brain networks. Our simulations suggest that the hippocampus is the most likely seed region to initiate the progression of Alzheimer's disease, and that changes associated with dementia begin to manifest structurally at simulated stage -7, presumably before meeting diagnostic criteria for clinical dementia. Nevertheless, it is important to acknowledge that a definitive validation is required at this point to translate these findings into the clinical practice. In particular, the inclusion of actual patients before or during the MCI phase and prodromal dementia is essential.

Precisely because the brain is a connected system, disruptions caused by neurological and psychiatric disorders can be reflected over many regions and connections. We have explored how alcohol use disorder impacts on spontaneous functional brain networks by comparing connection weights

between control and PD rats. The hippocampal formation together with the temporal cortex and subcortical regions (the lateral hypothalamus, central amygdala and raphe nucleus) are disrupted in alcohol use disorder. In particular, they form a subnetwork wherein activity is decreased after alcohol consumption, making it a potential target for therapy. A future research line should assess in depth the effect of data preprocessing on the differences observed between groups. And more importantly, electrophysiological-fMRI experiments in animals models have the potential of elucidating the relationship between the BOLD signal and the concomitant neural activity, as they allow a greater experimental control.

These results provide further evidence that approaching the brain as a complex network offers valuable insights into the principles underlying brain structure and function. Brain regions are intimately connected forming networks, the brain networks. These brain networks are characterized by the presence of communities o modules and strategic core nodes or hubs that facilitate intermodular organization and global integration, so brain diseases that harm hubs can be disastrous.

Curriculum Vitae

Research internships

- Dynamic Connectome Laboratory, Interdisciplinary Computing and Complex Biosystems Research Group, School of Computing, Newcastle University (April 4, 2017 – October 3, 2017). Supervisor: Marcus Kaiser.

- Computational Cognitive Neuroscience Laboratory, Department of Psychological and Brain Science, Indiana University (February 16, 2016 – May 16, 2016). Supervisor: Olaf Sporns.

Journal papers

Díaz-Parra, A., Kennion, O., Moratal, D., Taylor, J.-P., Kaiser, M., Bauer, R., and Alzheimer's Disease Neuroimaging Initiative (2018). "Structural connectivity centrality changes mark the path towards Alzheimer's disease". *Alzheimer's & Dementia: Diagnosis, Assessment & Disease Monitoring* (Submitted). *The content of this publication has been adapted for chapter 4.

Díaz-Parra, A., Osborn, Z., Canals, S., Moratal, D., and Sporns, O. (2017). "Structural and functional, empirical and modeled connectivity in the cerebral cortex of the rat". *NeuroImage* 159, pp. 170–184. *The content of this publication has been adapted for chapter 3.

Ruiz-España, S., Domingo, J., **Díaz-Parra, A.**, Dura, E., D'Ocón-Alcañiz, V., Arana, E., and Moratal, D. (2017). "Automatic segmentation of the spine by means of a probabilistic atlas with a special focus on ribs suppression". *Medical Physics* 44, pp. 4695–4707.

International conferences

Díaz-Parra, A., Pérez-Ramírez, Ú., Pacheco-Torres, J., Pfarr, S., Sommer, W. H., Moratal, D., and Canals, S. (2017). "Evaluating network brain connectivity in alcohol postdependent state using network-based statistic". *39th Annual International Conference of the IEEE Engineering in Medicine and Biology Society (EMBC 2017)*, pp. 533–536. *The content of this publication has been adapted for chapter 5.

Díaz-Parra, A., Canals, S., and Moratal, D. (2017). "A fully automated method for segmentation and classification of local field potential recordings. Preliminary results". *39th Annual International Conference of the IEEE Engineering in Medicine and Biology Society (EMBC 2017)*, pp. 426–429.

Pérez-Ramírez, Ú., **Díaz-Parra, A.**, Ciccocioppo, R., Canals, S., and Moratal, D. (2017). "Brain functional connectivity alterations in a rat model of excessive alcohol drinking: a resting-state network analysis". *39th Annual International Conference of the IEEE Engineering in Medicine and Biology Society (EMBC 2017)*, pp. 3016–3019.

Ortiz-Ramón, R., Ruiz-España, S., Pérez-Ramírez, Ú., **Díaz-Parra, A.**, Ciccocioppo, R., Canals, S., and Moratal, D. (2017). "Evaluation of texture features on resting-state networks of a rat model of alcohol use disorders". *34th Annual Scientific Meeting of the European Society for Magnetic Resonance in Medicine and Biology (ESMRMB 2017)*, pp. 623–624.

Ruiz-España, S., Ortiz-Ramón, R., Pérez-Ramírez, Ú., **Díaz-Parra, A.**, Ciccocioppo, R., Canals, S., and Moratal, D. (2017). "Evaluation of 2D texture analysis on fMRI data to identify changes in the striatal network induced by alcohol drinking". *34th Annual Scientific Meeting of the European Society for Magnetic Resonance in Medicine and Biology (ESMRMB 2017)*, pp. 653–654.

Ortiz-Ramón, R., Llorca, A., Pérez-Ramírez, Ú., **Díaz-Parra, A.**, Marín, O., and Moratal, D. (2017). "Registration of mouse brain microscopy images to a MR mouse brain atlas for locating interneuron cells: a preliminary study". *34th Annual Scientific Meeting of the European Society for Magnetic Resonance in Medicine and Biology (ESMRMB 2017)*, pp. 625–625.

Pérez-Ramírez, Ú., **Díaz-Parra, A.**, Moratal, D., and Canals, S. (2015). "Resting-state brain networks during high levels of alcohol drinking followed by abstinence in rats". *15th Congress of the European Society for Biomedical Research on Alcoholism (ESBRA 2015)*, pp. 58–59.

Ruiz-España, S., **Díaz-Parra, A.**, Arana, E., and Moratal, D. (2015). "A fully automated level-set based segmentation method of thoracic and lumbar vertebral bodies in computed tomography images". *37th Annual International Conference of the IEEE Engineering in Medicine and Biology Society (EMBC 2015)*, pp. 3049–3052.

Ruiz-España, S., Domingo, J., **Díaz-Parra, A.**, Dura, E., D'Ocón-Alcañiz, V., Arana, E., and Moratal, D. (2015). "Automatic segmentation of the spine by means of a probabilistic atlas with a special focus on ribs suppression. Preliminary results". *37th Annual International Conference of the IEEE Engineering in Medicine and Biology Society (EMBC 2015)*, pp. 2014–2017.

Díaz-Parra, A., Arana, E., and Moratal, D. (2014). "A fully automated method for spinal canal detection in computed tomography images". *36th Annual International Conference of the IEEE Engineering in Medicine and Biology Society (EMBC 2014)*, pp. 5514–5517.

Díaz-Parra, A., Arana, E., and Moratal, D. (2014). "Fully automatic spinal canal segmentation for radiation therapy using a gradient vector flow-based method on computed tomography images: a preliminary study". *36th Annual International Conference of the IEEE Engineering in Medicine and Biology Society (EMBC 2014)*, pp. 5518–5521.

References

Abhinav, K., Yeh, F.-C., Pathak, S., Suski, V., Lacomis, D., Friedlander, R. M., and Fernandez-Miranda, J. C. (2014). "Advanced diffusion MRI fiber tracking in neurosurgical and neurodegenerative disorders and neuroanatomical studies: a review". *Biochimica et Biophysica Acta (BBA) - Molecular Basis of Disease* 1842, pp. 2286–2297.

Adachi, Y., Osada, T., Sporns, O., Watanabe, T., Matsui, T., Miyamoto, K., and Miyashita, Y. (2012). "Functional connectivity between anatomically unconnected areas is shaped by collective network-level effects in the macaque cortex". *Cerebral Cortex* 22, pp. 1586–1592.

Aerts, H., Fias, W., Caeyenberghs, K., and Marinazzo, D. (2016). "Brain networks under attack: robustness properties and the impact of lesions". *Brain* 139, pp. 3063–3083.

Alexander-Bloch, A., Lambiotte, R., Roberts, B., Giedd, J., Gogtay, N., and Bullmore, E. (2012). "The discovery of population differences in network community structure: New methods and applications to brain functional networks in schizophrenia". *NeuroImage* 59, pp. 3889–3900.

Alon, U. (2007). "Network motifs: theory and experimental approaches". *Nature Reviews Genetics* 8, pp. 450–461.

Alzheimer's Association (2017). "2017 Alzheimer's disease facts and figures". *Alzheimer's & Dementia* 13, pp. 325–373.

Andersson, J. L. R. and Sotiropoulos, S. N. (2016). "An integrated approach to correction for off-resonance effects and subject movement in diffusion MR imaging". *NeuroImage* 125, pp. 1063–1078.

Arenas, A., Fernández, A., Fortunato, S., and Gómez, S. (2008). "Motif-based communities in complex networks". *Journal of Physics A: Mathematical and Theoretical* 41, p. 224001.

Barthélemy, M. (2011). "Spatial networks". *Physics Reports* 499, pp. 1–101.

Barttfeld, P., Uhrig, L., Sitt, J. D., Sigman, M., Jarraya, B., and Dehaene, S. (2015). "Signature of consciousness in the dynamics of resting-state brain activity". *Proceedings of the National Academy of Sciences* 112, pp. 887–892.

Bassett, D. S., Porter, M. A., Wymbs, N. F., Grafton, S. T., Carlson, J. M., and Mucha, P. J. (2013). "Robust detection of dynamic community structure in networks". *Chaos* 23, p. 013142.

Bassett, D. S. and Sporns, O. (2017). "Network neuroscience". *Nature Neuroscience* 20, pp. 353–364.

Batalle, D. et al. (2017). "Early development of structural networks and the impact of prematurity on brain connectivity". *NeuroImage* 149, pp. 379–392.

Bazzi, M., Porter, M. A., Williams, S., McDonald, M., Fenn, D. J., and Howison, S. D. (2016). "Community detection in temporal multilayer networks, with an application to correlation networks". *Multiscale Modeling & Simulation* 14, pp. 1–41.

Benjamini, Y. and Hochberg, Y. (1995). "Controlling the false discovery rate: a practical and powerful approach to multiple testing". *Journal of the Royal Statistical Society. Series B (Methodological)* 57, pp. 289–300.

Benson, A. R., Gleich, D. F., and Leskovec, J. (2016). "Higher-order organization of complex networks". *Science* 353, pp. 163–166.

Bergmann, E., Zur, G., Bershadsky, G., and Kahn, I. (2016). "The organization of mouse and human cortico-hippocampal networks estimated by intrinsic functional connectivity". *Cerebral Cortex* 26, pp. 4497–4512.

Betzel, R. F. et al. (2016). "Generative models of the human connectome". *NeuroImage* 124, Part, pp. 1054–1064.

Blondel, V. D., Guillaume, J.-L., Lambiotte, R., and Lefebvre, E. (2008). "Fast unfolding of communities in large networks". *Journal of Statistical Mechanics: Theory and Experiment* 2008, P10008.

Boccaletti, S., Bianconi, G., Criado, R., Genio, C. I. del, Gómez-Gardeñes, J., Romance, M., Sendiña-Nadal, I., Wang, Z., and Zanin, M. (2014). "The structure and dynamics of multilayer networks". *Physics Reports* 544, pp. 1–122.

Boccaletti, S., Latora, V., Moreno, Y., Chavez, M., and Hwang, D.-U. (2006). "Complex networks: structure and dynamics". *Physics Reports* 424, pp. 175–308.

Bota, M., Sporns, O., and Swanson, L. W. (2015). "Architecture of the cerebral cortical association connectome underlying cognition". *Proceedings of the National Academy of Sciences* 112, E2093–E2101.

Bowman, F. D., Zhang, L., Derado, G., and Chen, S. (2012). "Determining functional connectivity using fMRI data with diffusion-based anatomical weighting". *NeuroImage* 62, pp. 1769–1779.

Braak, H., Alafuzoff, I., Arzberger, T., Kretzschmar, H., and Del Tredici, K. (2006). "Staging of Alzheimer disease-associated neurofibrillary pathology using paraffin sections and immunocytochemistry". *Acta Neuropathologica* 112, pp. 389–404.

Breiman, L. (2001). "Random Forests". *Machine Learning* 45, pp. 5–32.

Brettschneider, J., Tredici, K. D., Lee, V. M.-Y., and Trojanowski, J. Q. (2015). "Spreading of pathology in neurodegenerative diseases: a focus on human studies". *Nature Reviews Neuroscience* 16, pp. 109–120.

Brier, M. R., Thomas, J. B., and Ances, B. M. (2014). "Network dysfunction in Alzheimer's disease: refining the disconnection hypothesis". *Brain Connectivity* 4, pp. 299–311.

Bruen, P. D., McGeown, W. J., Shanks, M. F., and Venneri, A. (2008). "Neuroanatomical correlates of neuropsychiatric symptoms in Alzheimer's disease". *Brain* 131, pp. 2455–2463.

Buckner, R. L., Sepulcre, J., Talukdar, T., Krienen, F. M., Liu, H., Hedden, T., Andrews-Hanna, J. R., Sperling, R. A., and Johnson, K. A. (2009). "Cortical hubs revealed by intrinsic functional connectivity: mapping, assessment of stability, and relation to Alzheimer's disease". *The Journal of Neuroscience* 29, pp. 1860–1873.

Bullmore, E. and Sporns, O. (2009). "Complex brain networks: graph theoretical analysis of structural and functional systems". *Nature Reviews Neuroscience* 10, pp. 186–198.

Bullmore, E. T. and Bassett, D. S. (2011). "Brain graphs: graphical models of the human brain connectome". *Annual Review of Clinical Psychology* 7, pp. 113–140.

Buxton, R. (2010). "Interpreting oxygenation-based neuroimaging signals: the importance and the challenge of understanding brain oxygen metabolism". *Frontiers in Neuroenergetics* 2, p. 8.

Chang, C.-C. and Lin, C.-J. (2011). "LIBSVM: a library for support vector machines". *ACM Transactions on Intelligent Systems and Technology* 2, p. 27.

Chanraud, S., Pitel, A.-L., Pfefferbaum, A., and Sullivan, E. V. (2011). "Disruption of functional connectivity of the default-mode network in alcoholism". *Cerebral Cortex* 21, pp. 2272–2281.

Chen, G., Ward, B. D., Xie, C., Li, W., Wu, Z., Jones, J. L., Franczak, M., Antuono, P., and Li, S.-J. (2011). "Classification of Alzheimer disease, mild cognitive impairment, and normal cognitive status with large-scale network analysis based on resting-state functional MR imaging". *Radiology* 259, pp. 213–221.

Ciric, R. et al. (2017). "Benchmarking of participant-level confound regression strategies for the control of motion artifact in studies of functional connectivity". *NeuroImage* 154, pp. 174–187.

Cole, D. M., Smith, S. M., and Beckmann, C. F. (2010). "Advances and pitfalls in the analysis and interpretation of resting-state FMRI data". *Frontiers in Systems Neuroscience* 4, p. 8.

Cole, M. W., Bassett, D. S., Power, J. D., Braver, T. S., and Petersen, S. E. (2014). "Intrinsic and task-evoked network architectures of the human brain". *Neuron* 83, pp. 238–251.

Collin, G. and van den Heuvel, M. P. (2013). "The ontogeny of the human connectome: development and dynamic changes of brain connectivity across the life span". *The Neuroscientist* 19, pp. 616–628.

Cope, T. E. et al. (2018). "Tau burden and the functional connectome in Alzheimer's disease and progressive supranuclear palsy". *Brain* 141, pp. 550–567.

Craddock, R. C., Holtzheimer, P. E., Hu, X. P., and Mayberg, H. S. (2009). "Disease state prediction from resting state functional connectivity". *Magnetic Resonance in Medicine* 62, pp. 1619–1628.

Craddock, R. C. et al. (2013). "Imaging human connectomes at the macroscale". *Nature Methods* 10, pp. 524–539.

Damoiseaux, J. S. and Greicius, M. D. (2009). "Greater than the sum of its parts: a review of studies combining structural connectivity and resting-state functional connectivity". *Brain Structure and Function* 213, pp. 525–533.

de Haan, W. (2017). "The virtual trial". *Frontiers in Neuroscience* 11, p. 110.

Deco, G., Jirsa, V. K., and McIntosh, A. R. (2011). "Emerging concepts for the dynamical organization of resting-state activity in the brain". *Nature Reviews Neuroscience* 12, pp. 43–56.

Deco, G. and Kringelbach, M. L. (2014). "Great expectations: using whole-brain computational connectomics for understanding neuropsychiatric disorders". *Neuron* 84, pp. 892–905.

Delbeuck, X., Van der Linden, M., and Collette, F. (2003). "Alzheimer' disease as a disconnection syndrome?" *Neuropsychology Review* 13, pp. 79–92.

Desikan, R. S. et al. (2006). "An automated labeling system for subdividing the human cerebral cortex on MRI scans into gyral based regions of interest". *NeuroImage* 31, pp. 968–980.

Desikan, R. S. et al. (2009). "Automated MRI measures identify individuals with mild cognitive impairment and Alzheimer's disease". *Brain* 132, pp. 2048–2057.

Díaz-Parra, A., Pérez-Ramírez, Ú., Pacheco-Torres, J., Pfarr, S., Sommer, W. H., Moratal, D., and Canals, S. (2017a). "Evaluating network brain connectivity in alcohol postdependent state using network-based statistic". *39th Annual International Conference of the IEEE Engineering in Medicine and Biology Society (EMBC 2017)*, pp. 533–536.

Díaz-Parra, A., Kennion, O., Moratal, D., Taylor, J.-P., Kaiser, M., Bauer, R., and Alzheimer's Disease Neuroimaging Initiative (2018). "Structural connectivity centrality changes mark the path towards Alzheimer's disease". *Alzheimer's & Dementia: Diagnosis, Assessment & Disease Monitoring* (Submitted).

Díaz-Parra, A., Osborn, Z., Canals, S., Moratal, D., and Sporns, O. (2017b). "Structural and functional, empirical and modeled connectivity in the cerebral cortex of the rat". *NeuroImage* 159, pp. 170–184.

Diez, I., Bonifazi, P., Escudero, I., Mateos, B., Muñoz, M. A., Stramaglia, S., and Cortes, J. M. (2015). "A novel brain partition highlights the modular skeleton shared by structure and function". *Scientific Reports* 5.

D'Souza, D. V., Jonckers, E., Bruns, A., Künnecke, B., von Kienlin, M., der Linden, A., Mueggler, T., and Verhoye, M. (2014). "Preserved modular network organization in the sedated rat brain". *PLoS ONE* 9, e106156.

Ebadi, A., Dalboni da Rocha, J. L., Nagaraju, D. B., Tovar-Moll, F., Bramati, I., Coutinho, G., Sitaram, R., and Rashidi, P. (2017). "Ensemble classification of Alzheimer's disease and mild cognitive impairment based on complex graph measures from diffusion tensor images". *Frontiers in Neuroscience* 11, p. 56.

Fagerholm, E. D., Hellyer, P. J., Scott, G., Leech, R., and Sharp, D. J. (2015). "Disconnection of network hubs and cognitive impairment after traumatic brain injury". *Brain* 138, pp. 1696–1709.

Feldstein Ewing, S. W., Sakhardande, A., and Blakemore, S.-J. (2014). "The effect of alcohol consumption on the adolescent brain: a systematic review of MRI and fMRI studies of alcohol-using youth". *NeuroImage: Clinical* 5, pp. 420–437.

Ferezou, I., Haiss, F., Gentet, L. J., Aronoff, R., Weber, B., and Petersen, C. C. H. (2007). "Spatiotemporal dynamics of cortical sensorimotor integration in behaving mice". *Neuron* 56, pp. 907–923.

Fischi-Gómez, E., Vasung, L., Meskaldji, D.-E., Lazeyras, F., Borradori-Tolsa, C., Hagmann, P., Barisnikov, K., Thiran, J.-P., and Hüppi, P. S. (2015). "Structural brain connectivity in school-age preterm infants provides evidence for impaired networks relevant for higher order cognitive skills and social cognition". *Cerebral Cortex* 25, pp. 2793–2805.

Fjell, A. M., McEvoy, L., Holland, D., Dale, A. M., and Walhovd, K. B. (2014). "What is normal in normal aging? Effects of aging, amyloid and Alzheimer's disease on the cerebral cortex and the hippocampus". *Progress in Neurobiology* 117, pp. 20–40.

Fornito, A., Zalesky, A., and Breakspear, M. (2013). "Graph analysis of the human connectome: promise, progress, and pitfalls". *NeuroImage* 80, pp. 426–444.

Fornito, A., Zalesky, A., and Breakspear, M. (2015). "The connectomics of brain disorders". *Nature Reviews Neuroscience* 16, pp. 159–172.

Fornito, A., Zalesky, A., and Bullmore, E. (2010). "Network scaling effects in graph analytic studies of human resting-state fMRI data". *Frontiers in Systems Neuroscience* 4, p. 22.

Fornito, A., Zalesky, A., and Bullmore, E. (2016). *Fundamentals of brain network analysis.* 1st ed. San Diego: Academic Press.

Fornito, A., Zalesky, A., Pantelis, C., and Bullmore, E. T. (2012). "Schizophrenia, neuroimaging and connectomics". *NeuroImage* 62, pp. 2296–2314.

Fortunato, S. (2010). "Community detection in graphs". *Physics Reports* 486, pp. 75–174.

Fortunato, S. and Barthélemy, M. (2007). "Resolution limit in community detection". *Proceedings of the National Academy of Sciences* 104, pp. 36–41.

Fortunato, S. and Hric, D. (2016). "Community detection in networks: a user guide". *Physics Reports* 659, pp. 1–44.

Fox, M. D. and Raichle, M. E. (2007). "Spontaneous fluctuations in brain activity observed with functional magnetic resonance imaging". *Nature Reviews Neuroscience* 8, pp. 700–711.

Fox, M. D., Zhang, D., Snyder, A. Z., and Raichle, M. E. (2009). "The global signal and observed anticorrelated resting state brain networks". *Journal of Neurophysiology* 101, pp. 3270–3283.

Frisoni, G. B., Fox, N. C., Jack Jr, C. R., Scheltens, P., and Thompson, P. M. (2010). "The clinical use of structural MRI in Alzheimer disease". *Nature Reviews Neurology* 6, pp. 67–77.

Frisoni, G. B., Prestia, A., Rasser, P. E., Bonetti, M., and Thompson, P. M. (2009). "In vivo mapping of incremental cortical atrophy from incipient to overt Alzheimer's disease". *Journal of Neurology* 256, pp. 916–924.

Friston, K. J., Harrison, L., and Penny, W. (2003). "Dynamic causal modelling". *NeuroImage* 19, pp. 1273–1302.

Friston, K. (2002). "Functional integration and inference in the brain". *Progress in Neurobiology* 68, pp. 113–143.

Friston, K. J. (2011). "Functional and effective connectivity: a review". *Brain Connectivity* 1, pp. 13–36.

Friston, K. J., Williams, S., Howard, R., Frackowiak, R. S. J., and Turner, R. (1996). "Movement-Related effects in fMRI time-series". *Magnetic Resonance in Medicine* 35, pp. 346–355.

Frost, B. and Diamond, M. I. (2009). "Prion-like mechanisms in neurodegenerative diseases". *Nature Reviews Neuroscience* 11, pp. 155–159.

Frostig, R. D., Xiong, Y., Chen-Bee, C. H., Kvašňák, E., and Stehberg, J. (2008). "Large-scale organization of rat sensorimotor cortex based on a motif of large activation spreads". *The Journal of Neuroscience* 28, 13274 LP –13284.

Gallos, L. K., Makse, H. A., and Sigman, M. (2012). "A small world of weak ties provides optimal global integration of self-similar modules in functional brain networks". *Proceedings of the National Academy of Sciences* 109, pp. 2825–2830.

Goñi, J. et al. (2014). "Resting-brain functional connectivity predicted by analytic measures of network communication". *Proceedings of the National Academy of Sciences* 111, pp. 833–838.

Gozzi, A. and Schwarz, A. J. (2016). "Large-scale functional connectivity networks in the rodent brain". *NeuroImage* 127, pp. 496–509.

Grandjean, J., Schroeter, A., Batata, I., and Rudin, M. (2014). "Optimization of anesthesia protocol for resting-state fMRI in mice based on differential effects of anesthetics on functional connectivity patterns". *NeuroImage* 102, Part, pp. 838–847.

Grayson, D. S., Bliss-Moreau, E., Machado, C. J., Bennett, J., Shen, K., Grant, K. A., Fair, D. A., and Amaral, D. G. (2016). "The rhesus

monkey connectome predicts disrupted functional networks resulting from pharmacogenetic inactivation of the amygdala". *Neuron* 91, pp. 453–466.

Guyon, I. and Elisseeff, A. (2003). "An introduction to variable and feature selection". *Journal of Machine Learning Research* 3, pp. 1157–1182.

Hanley, J. A. and McNeil, B. J. (1982). "The meaning and use of the area under a receiver operating characteristic (ROC) curve." *Radiology* 143, pp. 29–36.

Hebert, L. E., Weuve, J., Scherr, P. A., and Evans, D. A. (2013). "Alzheimer disease in the United States (2010–2050) estimated using the 2010 census". *Neurology* 80, pp. 1778–1783.

Hermundstad, A. M. et al. (2013). "Structural foundations of resting-state and task-based functional connectivity in the human brain". *Proceedings of the National Academy of Sciences* 110, pp. 6169–6174.

Holme, P. and Saramäki, J. (2012). "Temporal networks". *Physics Reports* 519, pp. 97–125.

Honey, C. J., Thivierge, J.-P., and Sporns, O. (2010). "Can structure predict function in the human brain?" *NeuroImage* 52, pp. 766–776.

Horwitz, B. (2003). "The elusive concept of brain connectivity". *NeuroImage* 19, pp. 466–470.

Hsu, L.-M. et al. (2016). "Constituents and functional implications of the rat default mode network". *Proceedings of the National Academy of Sciences* 113, E4541–E4547.

Iturria-Medina, Y., Sotero, R. C., Toussaint, P. J., Evans, A. C., and Alzheimer's Disease Neuroimaging Initiative (2014). "Epidemic spreading model to characterize misfolded proteins propagation in aging and associated neurodegenerative disorders". *PLOS Computational Biology* 10, e1003956.

Jack, C. R. and Holtzman, D. M. (2013). "Biomarker modeling of Alzheimer's disease". *Neuron* 80, pp. 1347–1358.

Jack, C. R. et al. (2013). "Tracking pathophysiological processes in Alzheimer's disease: an updated hypothetical model of dynamic biomarkers". *The Lancet Neurology* 12, pp. 207–216.

James, G., Witten, D., Hastie, T., and Tibshirani, R. (2013). *An introduction to statistical learning with applications in R.* 1st ed. New York: Springer.

Jbabdi, S., Sotiropoulos, S. N., Haber, S. N., Van Essen, D. C., and Behrens, T. E. (2015). "Measuring macroscopic brain connections in vivo". *Nature Neuroscience* 18, pp. 1546–1555.

Jenkinson, M., Bannister, P., Brady, M., and Smith, S. (2002). "Improved optimization for the robust and accurate linear registration and motion correction of brain images". *NeuroImage* 17, pp. 825–841.

Jenkinson, M., Beckmann, C. F., Behrens, T. E. J., Woolrich, M. W., and Smith, S. M. (2012). "FSL". *NeuroImage* 62, pp. 782–790.

Jenkinson, M. and Smith, S. (2001). "A global optimisation method for robust affine registration of brain images". *Medical Image Analysis* 5, pp. 143–156.

Jie, B., Wee, C.-Y., Shen, D., and Zhang, D. (2016). "Hyper-connectivity of functional networks for brain disease diagnosis". *Medical Image Analysis* 32, pp. 84–100.

John, M., Ikuta, T., and Ferbinteanu, J. (2017). "Graph analysis of structural brain networks in Alzheimer's disease: beyond small world properties". *Brain Structure and Function* 222, pp. 923–942.

Jonckers, E., Shah, D., Hamaide, J., Verhoye, M., and Van der Linden, A. (2015). "The power of using functional fMRI on small rodents to study brain pharmacology and disease". *Frontiers in Pharmacology* 6, p. 231.

Jucker, M. and Walker, L. C. (2011). "Pathogenic protein seeding in Alzheimer disease and other neurodegenerative disorders". *Annals of Neurology* 70, pp. 532–540.

Jucker, M. and Walker, L. C. (2013). "Self-propagation of pathogenic protein aggregates in neurodegenerative diseases". *Nature* 501, pp. 45–51.

Kaiser, M. (2011). "A tutorial in connectome analysis: Topological and spatial features of brain networks". *NeuroImage* 57, pp. 892–907.

Kaiser, M. (2013). "The potential of the human connectome as a biomarker of brain disease". *Frontiers in Human Neuroscience* 7, p. 484.

Kalthoff, D., Po, C., Wiedermann, D., and Hoehn, M. (2013). "Reliability and spatial specificity of rat brain sensorimotor functional connectivity networks are superior under sedation compared with general anesthesia". *NMR in Biomedicine* 26, pp. 638–650.

Kalthoff, D., Seehafer, J. U., Po, C., Wiedermann, D., and Hoehn, M. (2011). "Functional connectivity in the rat at 11.7 T: impact of physiological noise in resting state fMRI". *NeuroImage* 54, pp. 2828–2839.

Klöppel, S. et al. (2008). "Automatic classification of MR scans in Alzheimer's disease". *Brain* 131, pp. 681–689.

Kuhn, M. (2013). *Applied predictive modeling.* New York: Springer.

Lancichinetti, A. and Fortunato, S. (2012). "Consensus clustering in complex networks". *Scientific Reports* 2, p. 336.

Lemm, S., Blankertz, B., Dickhaus, T., and Müller, K.-R. (2011). "Introduction to machine learning for brain imaging". *NeuroImage* 56, pp. 387–399.

Liang, Z., King, J., and Zhang, N. (2012). "Intrinsic organization of the anesthetized brain". *The Journal of Neuroscience* 32, pp. 10183–10191.

Lim, S., Han, C. E., Uhlhaas, P. J., and Kaiser, M. (2015). "Preferential detachment during human brain development: age- and sex-specific structural connectivity in diffusion tensor imaging (DTI) Data". *Cerebral Cortex* 25, pp. 1477–1489.

Lo, C.-Y., Wang, P.-N., Chou, K.-H., Wang, J., He, Y., and Lin, C.-P. (2010). "Diffusion tensor tractography reveals abnormal topological organization in structural cortical networks in Alzheimer's disease". *The Journal of Neuroscience* 30, pp. 16876–16885.

Logothetis, N. K. (2008). "What we can do and what we cannot do with fMRI". *Nature* 453, pp. 869–878.

MacMahon, M. and Garlaschelli, D. (2015). "Community detection for correlation matrices". *Physical Review X* 5, p. 21006.

Magnin, B., Mesrob, L., Kinkingnéhun, S., Pélégrini-Issac, M., Colliot, O., Sarazin, M., Dubois, B., Lehéricy, S., and Benali, H. (2009). "Support vector machine-based classification of Alzheimer's disease from whole-brain anatomical MRI". *Neuroradiology* 51, pp. 73–83.

Mak, E. et al. (2017). "Structural neuroimaging in preclinical dementia: from microstructural deficits and grey matter atrophy to macroscale connectomic changes". *Ageing Research Reviews* 35, pp. 250–264.

Mathotaarachchi, S., Pascoal, T. A., Shin, M., Benedet, A. L., Kang, M. S., Beaudry, T., Fonov, V. S., Gauthier, S., and Rosa-Neto, P. (2017). "Identifying incipient dementia individuals using machine learning and amyloid imaging". *Neurobiology of Aging* 59, pp. 80–90.

Meinhardt, M. W. and Sommer, W. H. (2015). "Postdependent state in rats as a model for medication development in alcoholism". *Addiction Biology* 20, pp. 1–21.

Meinhardt, M. W. et al. (2013). "Rescue of infralimbic mGluR$_2$ deficit restores control over drug-seeking behavior in alcohol dependence". *The Journal of Neuroscience* 33, 2794 LP –2806.

Miller, K. L. et al. (2016). "Multimodal population brain imaging in the UK Biobank prospective epidemiological study". *Nature Neuroscience* 19, pp. 1523–1536.

Milo, R., Shen-Orr, S., Itzkovitz, S., Kashtan, N., Chklovskii, D., and Alon, U. (2002). "Network motifs: simple building blocks of complex networks". *Science* 298, pp. 824–827.

Mišić, B., Betzel, R. F., Nematzadeh, A., Goñi, J., Griffa, A., Hagmann, P., Flammini, A., Ahn, Y.-Y., and Sporns, O. (2015). "Cooperative and

competitive spreading dynamics on the human connectome". *Neuron* 86, pp. 1518–1529.

Mišić, B., Betzel, R. F., Reus, M. A. de, van den Heuvel, M. P., Berman, M. G., McIntosh, A. R., and Sporns, O. (2016). "Network-level structure-function relationships in human neocortex". *Cerebral Cortex*, pp. 1–12.

Mohajerani, M. H. et al. (2013). "Spontaneous cortical activity alternates between motifs defined by regional axonal projections". *Nature Neuroscience* 16, pp. 1426–1435.

Moradi, E., Pepe, A., Gaser, C., Huttunen, H., and Tohka, J. (2015). "Machine learning framework for early MRI-based Alzheimer's conversion prediction in MCI subjects". *NeuroImage* 104, pp. 398–412.

Moreno, A., Jego, P., Cruz, F. de la, and Canals, S. (2013). "Neurophysiological, metabolic and cellular compartments that drive neurovascular coupling and neuroimaging signals". *Frontiers in Neuroenergetics* 5, p. 3.

Mori, S., Crain, B. J., Chacko, V. P., and Van Zijl, P. C. M. (1999). "Three-dimensional tracking of axonal projections in the brain by magnetic resonance imaging". *Annals of Neurology* 45, pp. 265–269.

Müller, A. C. and Guido, S. (2016). *Introduction to machine learning with Python. A guide for data scientists.* California: O'Reilly Media.

Müller-Oehring, E. M., Jung, Y.-C., Pfefferbaum, A., Sullivan, E. V., and Schulte, T. (2014). "The resting brain of alcoholics". *Cerebral Cortex* 25, pp. 4155–4168.

Murphy, K., Birn, R. M., and Bandettini, P. A. (2013). "Resting-state fMRI confounds and cleanup". *NeuroImage* 80, pp. 349–359.

Murphy, K., Birn, R. M., Handwerker, D. A., Jones, T. B., and Bandettini, P. A. (2009). "The impact of global signal regression on resting state correlations: are anti-correlated networks introduced?" *NeuroImage* 44, pp. 893–905.

Nakagawa, T. T., Jirsa, V. K., Spiegler, A., McIntosh, A. R., and Deco, G. (2013). "Bottom up modeling of the connectome: linking structure and function in the resting brain and their changes in aging". *NeuroImage* 80, pp. 318–329.

Newman, M. E. J. (2003). "The structure and function of complex networks". *SIAM Review* 45, pp. 167–256.

Newman, M. E. J. (2010). *Networks an introduction*. 1st ed. New York: Oxford University Press.

Newman, M. E. J. and Girvan, M. (2004). "Finding and evaluating community structure in networks". *Physical Review E* 69, p. 26113.

Nooner, K. et al. (2012). "The NKI-Rockland sample: a model for accelerating the pace of discovery science in psychiatry". *Frontiers in Neuroscience* 6, p. 152.

O'Donnell, L. J. and Westin, C.-F. (2011). "An introduction to diffusion tensor image analysis". *Neurosurgery Clinics of North America* 22, pp. 185–196.

Oh, S. W. et al. (2014). "A mesoscale connectome of the mouse brain". *Nature* 508, pp. 207–214.

Paasonen, J., Salo, R. A., Shatillo, A., Forsberg, M. M., Närväinen, J., Huttunen, J. K., and Gröhn, O. (2016). "Comparison of seven different anesthesia protocols for nicotine pharmacologic magnetic resonance imaging in rat". *European Neuropsychopharmacology* 26, pp. 518–531.

Palop, J. J., Chin, J., and Mucke, L. (2006). "A network dysfunction perspective on neurodegenerative diseases". *Nature* 443, pp. 768–773.

Pan, W.-J., Billings, J. C. W., Grooms, J. K., Shakil, S., and Keilholz, S. D. (2015). "Considerations for resting state functional MRI and functional connectivity studies in rodents". *Frontiers in Neuroscience* 9, p. 269.

Park, H.-J. and Friston, K. (2013). "Structural and functional brain networks: from connections to cognition". *Science* 342, p. 1238411.

Pastor-Satorras, R., Castellano, C., Van Mieghem, P., and Vespignani, A. (2015). "Epidemic processes in complex networks". *Reviews of Modern Physics* 87, pp. 925–979.

Paxinos, G. and Watson, C. (1998). *The rat brain in stereotaxic coordinates*. 4th. San Diego: Academic Press.

Pedregosa, F. et al. (2011). "Scikit-learn: machine Learning in Python". *Journal of Machine Learning Research* 12, pp. 2825–2830.

Pei, S. and Makse, H. A. (2013). "Spreading dynamics in complex networks". *Journal of Statistical Mechanics: Theory and Experiment* 2013, P12002.

Pereira, F., Mitchell, T., and Botvinick, M. (2009). "Machine learning classifiers and fMRI: a tutorial overview". *NeuroImage* 45, S199–S209.

Perl, D. P. (2010). "Neuropathology of Alzheimer's disease". *Mount Sinai Journal of Medicine: A Journal of Translational and Personalized Medicine* 77, pp. 32–42.

Petersen, R. C. et al. (2010). "Alzheimer's Disease Neuroimaging Initiative (ADNI) clinical characterization". *Neurology* 74, pp. 201–209.

Pini, L., Pievani, M., Bocchetta, M., Altomare, D., Bosco, P., Cavedo, E., Galluzzi, S., Marizzoni, M., and Frisoni, G. B. (2016). "Brain atrophy in Alzheimer's disease and aging". *Ageing Research Reviews* 30, pp. 25–48.

Power, J. D., Barnes, K. A., Snyder, A. Z., Schlaggar, B. L., and Petersen, S. E. (2012). "Spurious but systematic correlations in functional connectivity MRI networks arise from subject motion". *NeuroImage* 59, pp. 2142–2154.

Power, J. D., Mitra, A., Laumann, T. O., Snyder, A. Z., Schlaggar, B. L., and Petersen, S. E. (2014). "Methods to detect, characterize, and remove motion artifact in resting state fMRI". *NeuroImage* 84, pp. 320–341.

Power, J. D., Plitt, M., Laumann, T. O., and Martin, A. (2017). "Sources and implications of whole-brain fMRI signals in humans". *NeuroImage* 146, pp. 609–625.

Power, J. D., Schlaggar, B. L., and Petersen, S. E. (2015). "Recent progress and outstanding issues in motion correction in resting state fMRI". *NeuroImage* 105, pp. 536–551.

Power, J. D. et al. (2011). "Functional network organization of the human brain". *Neuron* 72, pp. 665–678.

Prescott, J. W., Guidon, A., Doraiswamy, P. M., Choudhury, K. R., Liu, C., Petrella, J. R., and Alzheimer's Disease Neuroimaging Initiative (2014). "The Alzheimer structural connectome: changes in cortical network topology with increased amyloid plaque burden". *Radiology* 273, pp. 175–184.

Pruim, R. H. R., Mennes, M., Buitelaar, J. K., and Beckmann, C. F. (2015). "Evaluation of ICA-AROMA and alternative strategies for motion artifact removal in resting state fMRI". *NeuroImage* 112, pp. 278–287.

Raj, A., Kuceyeski, A., and Weiner, M. (2012). "A network diffusion model of disease progression in dementia". *Neuron* 73, pp. 1204–1215.

Raj, A., LoCastro, E., Kuceyeski, A., Tosun, D., Relkin, N., Weiner, M., and Alzheimer's Disease Neuroimaging Initiative (2015). "Network diffusion model of progression predicts longitudinal patterns of atrophy and metabolism in Alzheimer's disease". *Cell Reports* 10, pp. 359–369.

Razi, A. and Friston, K. J. (2016). "The connected brain: causality, models, and intrinsic dynamics". *IEEE Signal Processing Magazine* 33, pp. 14–35.

Razi, A., Seghier, M. L., Zhou, Y., McColgan, P., Zeidman, P., Park, H.-J., Sporns, O., Rees, G., and Friston, K. J. (2017). "Large-scale DCMs for resting-state fMRI". *Network Neuroscience* 1, pp. 222–241.

Reis, S. D. S., Hu, Y., Babino, A., Andrade Jr, J. S., Canals, S., Sigman, M., and Makse, H. A. (2014). "Avoiding catastrophic failure in correlated networks of networks". *Nature Physics* 10, pp. 762–767.

Rubinov, M. and Sporns, O. (2010). "Complex network measures of brain connectivity: uses and interpretations". *NeuroImage* 52, pp. 1059–1069.

Saeys, Y., Inza, I., and Larrañaga, P. (2007). "A review of feature selection techniques in bioinformatics". *Bioinformatics* 23, pp. 2507–2517.

Santos, C. Y., Snyder, P. J., Wu, W.-C., Zhang, M., Echeverria, A., and Alber, J. (2017). "Pathophysiologic relationship between Alzheimer's disease, cerebrovascular disease, and cardiovascular risk: a review and synthesis". *Alzheimer's & Dementia: Diagnosis, Assessment & Disease Monitoring* 7, pp. 69–87.

Satterthwaite, T. D. et al. (2013). "An improved framework for confound regression and filtering for control of motion artifact in the preprocessing of resting-state functional connectivity data". *NeuroImage* 64, pp. 240–256.

Savioz, A., Leuba, G., Vallet, P. G., and Walzer, C. (2009). "Contribution of neural networks to Alzheimer disease's progression". *Brain Research Bulletin* 80, pp. 309–314.

Saxena, S. and Caroni, P. (2011). "Selective neuronal vulnerability in neurodegenerative diseases: from stressor thresholds to degeneration". *Neuron* 71, pp. 35–48.

Schirner, M., Rothmeier, S., Jirsa, V. K., McIntosh, A. R., and Ritter, P. (2015). "An automated pipeline for constructing personalized virtual brains from multimodal neuroimaging data". *NeuroImage* 117, pp. 343–357.

Schwarz, A. J., Danckaert, A., Reese, T., Gozzi, A., Paxinos, G., Watson, C., Merlo-Pich, E. V., and Bifone, A. (2006). "A stereotaxic MRI template set for the rat brain with tissue class distribution maps and co-registered anatomical atlas: application to pharmacological MRI". *NeuroImage* 32, pp. 538–550.

Seeley, W. W., Crawford, R. K., Zhou, J., Miller, B. L., and Greicius, M. D. (2009). "Neurodegenerative diseases target large-scale human brain networks". *Neuron* 62, pp. 42–52.

Sethi, S. S., Zerbi, V., Wenderoth, N., Fornito, A., and Fulcher, B. D. (2017). "Structural connectome topology relates to regional BOLD signal dynamics in the mouse brain". *Chaos: An Interdisciplinary Journal of Nonlinear Science* 27, p. 47405.

Shao, J. et al. (2012). "Prediction of Alzheimer's disease using individual structural connectivity networks". *Neurobiology of Aging* 33, pp. 2756–2765.

Sinha, N., Dauwels, J., Kaiser, M., Cash, S. S., Brandon Westover, M., Wang, Y., and Taylor, P. N. (2017). "Predicting neurosurgical outcomes in focal epilepsy patients using computational modelling". *Brain* 140, pp. 319–332.

Skudlarski, P., Jagannathan, K., Anderson, K., Stevens, M. C., Calhoun, V. D., Skudlarska, B. A., and Pearlson, G. (2016). "Brain connectivity is not only lower but different in schizophrenia: a combined anatomical and functional approach". *Biological Psychiatry* 68, pp. 61–69.

Skudlarski, P., Jagannathan, K., Calhoun, V. D., Hampson, M., Skudlarska, B. A., and Pearlson, G. (2008). "Measuring brain connectivity: diffusion tensor imaging validates resting state temporal correlations". *NeuroImage* 43, pp. 554–561.

Smith, S. M. (2002). "Fast robust automated brain extraction". *Human Brain Mapping* 17, pp. 143–155.

Smith, S. M., Miller, K. L., Salimi-Khorshidi, G., Webster, M., Beckmann, C. F., Nichols, T. E., Ramsey, J. D., and Woolrich, M. W. (2011). "Network modelling methods for FMRI". *NeuroImage* 54, pp. 875–891.

Smith, S. M. et al. (2009). "Correspondence of the brain's functional architecture during activation and rest". *Proceedings of the National Academy of Sciences* 106, pp. 13040–13045.

Smith, S. M. et al. (2013). "Functional connectomics from resting-state fMRI". *Trends in Cognitive Sciences* 17, pp. 666–682.

Sommer, W. H., Rimondini, R., Hansson, A. C., Hipskind, P. A., Gehlert, D. R., Barr, C. S., and Heilig, M. A. (2008). "Upregulation of voluntary alcohol intake, behavioral sensitivity to stress, and amygdala Crhr1 expression following a history of dependence". *Biological Psychiatry* 63, pp. 139–145.

Sotiropoulos, S. N. and Zalesky, A. (2017). "Building connectomes using diffusion MRI: why, how and but". *NMR in Biomedicine*.

Sperling, R. A. et al. (2011). "Toward defining the preclinical stages of Alzheimer's disease: recommendations from the National Institute on Aging-Alzheimer's Association workgroups on diagnostic guidelines for Alzheimer's disease". *Alzheimer's & Dementia* 7, pp. 280–292.

Sporns, O. (2013). "The human connectome: origins and challenges". *NeuroImage* 80, pp. 53–61.

Sporns, O. and Betzel, R. F. (2016). "Modular Brain Networks". *Annual Review of Psychology* 67, pp. 613–640.

Sporns, O. and Kötter, R. (2004). "Motifs in brain networks". *PLoS Biology* 2.

Sporns, O., Tononi, G., and Kötter, R. (2005). "The human connectome: a structural description of the human brain". *PLoS Computational Biology* 1, e42.

Squartini, T., Picciolo, F., Ruzzenenti, F., and Garlaschelli, D. (2013). "Reciprocity of weighted networks". *Scientific Reports* 3, p. 2729.

Stafford, J. M. et al. (2014). "Large-scale topology and the default mode network in the mouse connectome". *Proceedings of the National Academy of Sciences* 111, pp. 18745–18750.

Stam, C. J. (2014). "Modern network science of neurological disorders". *Nature Reviews Neuroscience* 15, pp. 683–695.

Strogatz, S. H. (2001). "Exploring complex networks". *Nature* 410, pp. 268–276.

Swanson, L. W. (2004). *Brain maps: structure of the rat brain. A laboratory guide with printed and electronic templates for data, models and schematics.* 3rd. Amsterdam: Elsevier.

Swanson, L. W., Sporns, O., and Hahn, J. D. (2016). "Network architecture of the cerebral nuclei (basal ganglia) association and commissural connectome". *Proceedings of the National Academy of Sciences* 113, E5972–E5981.

Taylor, P. N., Han, C. E., Schoene-Bake, J.-C., Weber, B., and Kaiser, M. (2015). "Structural connectivity changes in temporal lobe epilepsy: spatial features contribute more than topological measures". *NeuroImage: Clinical* 8, pp. 322–328.

Taylor, P. N., Sinha, N., Wang, Y., Vos, S. B., Tisi, J. de, Miserocchi, A., McEvoy, A. W., Winston, G. P., and Duncan, J. S. (2018). "The impact of epilepsy surgery on the structural connectome and its relation to outcome". *NeuroImage: Clinical*.

Teipel, S. et al. (2015). "Multimodal imaging in Alzheimer's disease: validity and usefulness for early detection". *The Lancet Neurology* 14, pp. 1037–1053.

Telesford, Q. K., Simpson, S. L., Burdette, J. H., Hayasaka, S., and Laurienti, P. J. (2011). "The brain as a complex system: using network science as a tool for understanding the brain". *Brain Connectivity* 1, pp. 295–308.

Thomas Yeo, B. T. et al. (2011). "The organization of the human cerebral cortex estimated by intrinsic functional connectivity". *Journal of Neurophysiology* 106, pp. 1125–1165.

Tijms, B. M., Wink, A. M., de Haan, W., van der Flier, W. M., Stam, C. J., Scheltens, P., and Barkhof, F. (2013). "Alzheimer's disease: connecting findings from graph theoretical studies of brain networks". *Neurobiology of Aging* 34, pp. 2023–2036.

Traag, V. A., Van Dooren, P., and Nesterov, Y. (2011). "Narrow scope for resolution-limit-free community detection". *Physical Review E* 84, p. 16114.

Traud, A. L., Kelsic, E. D., Mucha, P. J., and Porter, M. A. (2011). "Comparing community structure to characteristics in online collegiate social networks". *SIAM Review* 53, pp. 526–543.

Turkheimer, F. E., Leech, R., Expert, P., Lord, L.-D., and Vernon, A. C. (2015). "The brain's code and its canonical computational motifs. From sensory cortex to the default mode network: a multi-scale model of brain function in health and disease". *Neuroscience & Biobehavioral Reviews* 55, pp. 211–222.

Uhrig, S. et al. (2016). "Differential roles for L-type calcium channel subtypes in alcohol dependence". *Neuropsychopharmacology.*

Valdes-Sosa, P. A., Roebroeck, A., Daunizeau, J., and Friston, K. (2011). "Effective connectivity: influence, causality and biophysical modeling". *NeuroImage* 58, pp. 339–361.

van den Heuvel, M. P., Bullmore, E. T., and Sporns, O. (2016a). "Comparative connectomics". *Trends in Cognitive Sciences* 20, pp. 345–361.

van den Heuvel, M. P., Kahn, R. S., Goñi, J., and Sporns, O. (2012). "High-cost, high-capacity backbone for global brain communication". *Proceedings of the National Academy of Sciences* 109, pp. 11372–11377.

van den Heuvel, M. P., Scholtens, L. H., and Reus, M. A. de (2016b). "Topological organization of connectivity strength in the rat connectome". *Brain Structure and Function* 221, pp. 1719–1736.

van den Heuvel, M. P. and Sporns, O. (2011). "Rich-club organization of the human connectome". *The Journal of Neuroscience* 31, pp. 15775–15786.

van den Heuvel, M. P. and Sporns, O. (2013). "Network hubs in the human brain". *Trends in Cognitive Sciences* 17, pp. 683–696.

Van Dijk, K. R. A., Sabuncu, M. R., and Buckner, R. L. (2012). "The influence of head motion on intrinsic functional connectivity MRI". *NeuroImage* 59, pp. 431–438.

Varoquaux, G. and Craddock, R. C. (2013). "Learning and comparing functional connectomes across subjects". *NeuroImage* 80, pp. 405–415.

Varshney, L. R., Chen, B. L., Paniagua, E., Hall, D. H., and Chklovskii, D. B. (2011). "Structural properties of the caenorhabditis elegans neuronal network". *PLoS Comput Biol* 7, e1001066.

Vértes, P. E., Alexander-Bloch, A. F., Gogtay, N., Giedd, J. N., Rapoport, J. L., and Bullmore, E. T. (2012). "Simple models of human brain functional networks". *Proceedings of the National Academy of Sciences* 109, pp. 5868–5873.

Villemagne, V. L. et al. (2013). "Amyloid β deposition, neurodegeneration, and cognitive decline in sporadic Alzheimer's disease: a prospective cohort study". *The Lancet Neurology* 12, pp. 357–367.

Vos, S. B., Tax, C. M. W., Luijten, P. R., Ourselin, S., Leemans, A., and Froeling, M. (2017). "The importance of correcting for signal drift in diffusion MRI". *Magnetic Resonance in Medicine* 77, pp. 285–299.

Wang, Y., Necus, J., Kaiser, M., and Mota, B. (2016). "Universality in human cortical folding in health and disease". *Proceedings of the National Academy of Sciences* 113, pp. 12820–12825.

Wang, Z., Dai, Z., Gong, G., Zhou, C., and He, Y. (2015). "Understanding structural-functional relationships in the human brain: a large-scale network perspective". *The Neuroscientist* 21, pp. 290–305.

Warren, J. D., Rohrer, J. D., Schott, J. M., Fox, N. C., Hardy, J., and Rossor, M. N. (2013). "Molecular nexopathies: a new paradigm of neurodegenerative disease". *Trends in Neurosciences* 36, pp. 561–569.

Watts, D. J. and Strogatz, S. H. (1998). "Collective dynamics of 'small-world' networks". *Nature* 393, p. 440.

Whitwell, J. L. et al. (2008). "MRI correlates of neurofibrillary tangle pathology at autopsy". *Neurology* 71, pp. 743–749.

Williams, K. A., Magnuson, M., Majeed, W., LaConte, S. M., Peltier, S. J., Hu, X., and Keilholz, S. D. (2010). "Comparison of α-chloralose, medetomidine and isoflurane anesthesia for functional connectivity mapping in the rat". *Magnetic Resonance Imaging* 28, pp. 995–1003.

Wirsich, J. et al. (2016). "Whole-brain analytic measures of network communication reveal increased structure-function correlation in right temporal lobe epilepsy". *NeuroImage: Clinical* 11, pp. 707–718.

Wirths, O. and Bayer, T. A. (2003). "α-Synuclein, Aβ and Alzheimer's disease". *Progress in Neuro-Psychopharmacology and Biological Psychiatry* 27, pp. 103–108.

Woo, C.-W., Chang, L. J., Lindquist, M. A., and Wager, T. D. (2017). "Building better biomarkers: brain models in translational neuroimaging". *Nature Neuroscience* 20, pp. 365–377.

World Health Organization (2014). *Global status report on alcohol and health.* Tech. rep. World Health, World Health.

Wu, C. W., Chen, C.-L., Liu, P.-Y., Chao, Y.-P., Biswal, B. B., and Lin, C.-P. (2011). "Empirical evaluations of slice-timing, smoothing, and normalization effects in seed-based, resting-state functional magnetic resonance imaging analyses". *Brain Connectivity* 1, pp. 401–410.

Wu, T.-F., Lin, C.-J., and Weng, R. C. (2004). "Probability estimates for multi-class classification by pairwise coupling". *The Journal of Machine Learning Research* 5, pp. 975–1005.

Xie, T. and He, Y. (2012). "Mapping the Alzheimer's brain with connectomics". *Frontiers in Psychiatry* 2, p. 77.

Yahata, N. et al. (2016). "A small number of abnormal brain connections predicts adult autism spectrum disorder". *Nature Communications* 7, p. 11254.

Yan, C.-G. et al. (2013). "A comprehensive assessment of regional variation in the impact of head micromovements on functional connectomics". *NeuroImage* 76, pp. 183–201.

Yekutieli, D. and Benjamini, Y. (1999). "Resampling-based false discovery rate controlling multiple test procedures for correlated test statistics". *Journal of Statistical Planning and Inference* 82, pp. 171–196.

Young, J., Modat, M., Cardoso, M. J., Mendelson, A., Cash, D., and Ourselin, S. (2013). "Accurate multimodal probabilistic prediction of conversion to Alzheimer's disease in patients with mild cognitive impairment". *NeuroImage: Clinical* 2, pp. 735–745.

Zalesky, A., Fornito, A., and Bullmore, E. (2012). "On the use of correlation as a measure of network connectivity". *NeuroImage* 60, pp. 2096–2106.

Zalesky, A., Fornito, A., and Bullmore, E. T. (2010). "Network-based statistic: identifying differences in brain networks". *NeuroImage* 53, pp. 1197–1207.

Zhan, L. et al. (2015). "Comparison of nine tractography algorithms for detecting abnormal structural brain networks in Alzheimer's disease". *Frontiers in Aging Neuroscience* 7, p. 48.

Zhao, T., Cao, M., Niu, H., Zuo, X.-N., Evans, A., He, Y., Dong, Q., and Shu, N. (2015). "Age-related changes in the topological organization of the white matter structural connectome across the human lifespan". *Human Brain Mapping* 36, pp. 3777–3792.

Zhou, J., Gennatas, E. D., Kramer, J. H., Miller, B. L., and Seeley, W. W. (2012). "Predicting regional neurodegeneration from the healthy brain functional connectome". *Neuron* 73, pp. 1216–1227.